EPFL

Thèse n° 9642

Broadband spectroscopy and inelastic light scattering on the canted antiferromagnet hematite for antiferromagnetic magnonics

Présentée le 13 juin 2023

Faculté des sciences et techniques de l'ingénieur
Laboratoire des matériaux magnétiques nanostructurés et magnoniques
Programme doctoral en science et génie des matériaux

pour l'obtention du grade de Docteur ès Sciences

par

Mohammad HAMDI

Acceptée sur proposition du jury

Prof. A. Mortensen, président du jury
Prof. D. Grundler, directeur de thèse
Prof. J. W. Klos, rapporteur
Dr O. V. Dobrovolskiy, rapporteur
Prof. I.-C. Benea-Chelmus, rapporteuse

École polytechnique fédérale de Lausanne

2023

If we knew what it was we were doing,
it would not be called research, would it?
— Albert Einstein

To the brave women of Iran. Your courage and persistence in the struggle for freedom is an inspiration to all of us. Especially to my wife Fatemeh and my mother Goli, two of those brave women who inspire me by their strength. I am truly lucky to have you in my life.

Acknowledgements

I would like to express my deepest gratitude to everyone who supported me scientifically as well as on a personal level. During my time at EPFL I had many positive encounters.

First and foremost I am extremely grateful to my supervisor **Prof. Dirk Grundler**. Thank you for the invaluable advice, continuous support, and patience during my PhD study. Your feedback was always encouraging, constructive and of tremendous help. Thank you for the rigorous proofreading of all my scientific works, which not only improved the works itself, but was also invaluable for improving my scientific writing. I learned from you not only how to do "excellent science" but also how to best present scientific achievements.

I would like to extend my sincere thanks to **Prof. Jarosław W. Kłos** and **Dr. Oleksandr Dobrovolskiy** as external referees, and **Prof. Ileana-Cristina Benea-Chelmus** as internal referee for taking the time to evaluate my thesis, and **Prof. Andreas Mortensen** for accepting to preside the examination committee. I would like to also thank **Prof. Philip J. W. Moll** for his constructive comments as the expert of my candidacy exam at EPFL.

I would like to thank and acknowledge all **collaborators**, in particular the **ERA.Net RUS Plus Call 2017** consortium members: **Prof. Sergey Nikitov** from the Russian Academy of Sciences, **Dr. Michal Mruczkiewicz** from the Slovak Academy of Sciences, **Dr. Alexandr Sadovnikov** from the Saratov State University for all the samples and discussions. A particular thank you to **Dr. Jilei Chen** from Southern University of Science and Technology and **Prof. Haiming Yu** from Beihang University for the $BiFeO_3/La_{0.67}Sr_{0.33}MnO_3$ sample and the successful collaboration. A big thank you to **Prof. Jean-Philippe Ansermet** and **Dr. Marcin Bialek** for generously providing a bulk crystal of α-Fe_2O_3. The results presented in chapter 4 of this thesis is from my measurements on this crystal.

Special thanks to the **CMI team** for maintaining a first-class cleanroom facility. A particular thank you goes to **Zdenek Benes** and **Joffrey Pernollet** for the crucial support concerning electron-beam lithography, to **Rémy Juttin** for the support concerning the sputtering machine and deposition recipes and to **Patrick Alain Madliger**, who ensured a safe and a cheerful working environment in the cleanroom. To **Adrien Toros** for dicing my substrates and electrically bonding even the most challenging samples. Especial thanks goes to **Didier Bouvet** and **Nicolas Leiser** for the thermal annealing processes.

To **all members and former members of LMGN**: Thank you for the many happy moments we shared. To **Andrea Mucchietto** with whom I enjoyed more than four amazing years confined in

the same office. Thank you for plenty of scientific and non-scientific discussions. I also need to thank you for all your help with e-beam lithography as well as all the AFM measurement you performed on my thin film samples. One day, you will crack the DNA of the spin waves, or maybe they will switch you! To **Dr. Korbinian Baumgaertl**, thank you for helping me walk the first steps in LMGN laboratories and for all the patient and detailed trainings on BLS setups. I still enjoy the interesting scientific and non-scientific discussions with you. To **Dr. Maria Carmen Giordano**, thank you for being such a kind colleague. I remember very well the CMi tour you had for me when I was here for my interview where your non-stop support started. I am thankful for the fruitful scientific collaboration on the nanotubes as well. To **Dr. Sho Watanabe**, thank you for your never ending support in the lab and the trainings on VNA and TDR setups. It was also a pleasure working with you on your magnonic quasi-crystals. To **Dr. Ping Che**, many thanks for all the trainings on the cryostats and fabricating CPWs for the entire group. Discussing science with you was always a pleasure for me. To **Dr. Anna Kúkol'ová**, thank you for always being supportive and bringing energy and laughter to the group. It was a pleasure collaborating with you on your Skyrmion hosting thin films. To **Ferdinand Posva**, thank you for all the VNA measurements you did on the hematite crystal which greatly helped us to reach to the optimized final experiments. To **Dr. Mingran Xu**, **Axel Deenen**, **Shreyas Joglekar**, **Huixin Guo** and **Anna Duvakina**, the new members of LMGN, thank you for all the scientific discussions and taking over the responsibility of the setups. Merci **Yuko Kagata** for the warm and friendly organizational support.

I would like to thank the **Swiss National Science Foundation** for funding this PhD project via grant **No. 177550**. More generally I would like to thank all Swiss tax payers for their indirect financial support to scientific research, which makes projects like this possible.

I wish to express my sincere gratitude to all of **my former teachers and professors** who thought me all the background I needed for my PhD and amplified my interest in Science and Physics. To **Mr. Heidari** who was a great Physics teacher in my high school. Your courses were always a joy and I would learn everything in the class, so much so that I even did not need to study for the final exam and yet get the full grade! I would not be exaggerating to say your fun course was one of the main factors for my interest in Physics and since then I dreamt to be a Physicist! From my bachelor studies: To **Prof. Arash Sabatyan** for showing me the great importance of mathematics in Physics with your excellent "Mathematical Physics" courses. To **Prof. Mahdi Amniat-Talab** whom I had many great courses with, including "Analytical Mechanics", "Quantum Mechanics I" and "Wave Physics". Thank you for teaching me the fundamentals of physics so rigorously. I will never forget how motivating it was to have a whole session presenting (or teaching like a super-star!) the black body radiation instead of you! With that presentation, I had the greatest opportunity to experience the joy of teaching. To **Prof. Korosh Aghayar**, for joyful courses on "Statistical Mechanics" and "Quantum Mechanics II". You introduced me to some of the most fascinating aspects of nature, and you taught me how to enjoy studying Physics even without formulas! You were the best teacher that I could have wished for. From my master studies: To **Prof. Nastaran Mansour** for her solid course on "Electrodynamics". Thank you for making Jackson so accessible and trusting me for being the

teaching assistant of your course for three years. I developed further my interest in teaching during those years. To **Prof. Ali Sadeghi** for great course on "Computational Physics", for co-supervising my master thesis and for later collaborations. And surely, **Prof. Majid Mohseni** for being such a great mentor and inspiration during my master thesis. My great interest in Spintronics was developed while working with you. I always enjoyed your phenomenological viewpoint in physics. Thank you for your continued support especially for the funding of my stay as Junior Researcher after my graduation. Without that period and the development of my research skills, I am not sure if I could land on such a great institute as EPFL. You may not know it, but as a child of middle class family, that few years of support has changed my life for ever. I should also thank you for your trust in me for letting me co-supervise some PhD students while I was myself a PhD student! I am very happy that those collaboration were successful.

Finally I would like to thank **my family and friends** for their unconditional support. To my parents **Maman Goli** and **Baba Shamsaldin** and my brother **Ahmad**. You have made so many sacrifices for me to continue. My mother has always been a symbol of resilience in the face of difficulties. Without you, I would not be the person I am today. To my brother in law **Abolfazl** and his wife **Parastoo** for all the support and care you had for me especially at the start of my PhD when everything was new and difficult. To **Amin** & **Ati** for all the good times we share since our master studies. It was always a pleasure hosting you at Lausanne and thank you for all the fun trips we went on together and also for providing us a second home in Antwerp.

Above all I would like to thank my wife **Fatemeh** for her love and constant support, for all the late nights and early mornings and for making home such a pleasant place for writing my thesis. Thank you for making my life and especially my PhD life so rich. But most of all, thank you for being my best friend and the source of daily inspiration. I owe you everything.

Lausanne, March 28, 2023
Mohammad

Abstract

Collective spin excitations propagating in magnetically ordered materials are called spin waves (SWs) or magnons. They are promising for low-power and beyond-CMOS information processing, which do not suffer from the ohmic losses. SWs in ferromagnets (antiferromagnets) cover the few GHz (hundreds of GHz to few THz) frequency regime and possess wavelengths in the range of few tens of nanometers which is about five (four) orders of magnitude shorter than electromagnetic waves of the same frequency. This property makes SWs an ideal candidate for applications in microwave and THz technology, essential for on-chip processing of wireless telecommunication signals. Of particular interest are the SWs in antiferromagnets (AFMs) because of the two following properties. First, they offer high group velocities due to negligible net magnetization and dipolar effects. Second, their high frequencies due to strong exchange interaction can be utilized to close the THz gap (overcoming the lack of small-sized solid-state THz sources). In this thesis, we investigate SWs in AFMs regarding their potential for i) microwave and ii) THz magnonic devices.

i) Yttrium iron garnet (YIG) has been considered the "fruit fly" of magnonics since 1961 due to its low magnetic damping. However, being a ferrimagnet, dipolar interactions cause its magnon band to be inherently anisotropic leading to a reduction of the SW group velocity by an order of magnitude to below 1 km/s in thin film form. Here we report the dispersion relation of the low-frequency SW branch of the natural mineral hematite in its canted AFM phase. We determine the damping coefficient of 1.1×10^{-5} from broadband GHz spectroscopy measurements at room temperature. The SW group velocities amount to a few 10 km/s measured by means of wave vector resolved inelastic Brillouin light scattering (BLS). We estimate the SW decay length at small magnetic field of 30 mT to be 1.1 cm. With such a fast SW speed and low damping, our results promote hematite as an alternative and sustainable basis for AFM magnonic devices based on a stable natural mineral.

ii) The advancement of compact and adaptable sources of THz-frequency electromagnetic signals would pave the way for a myriad of novel applications. AFM spintronics has introduced the AFM spin-Hall nano-oscillator (AFM-SHNO), which generates THz signal via the combination of spin-orbit torque (SOT) induced self-sustained THz spin dynamics, spin pumping and the inverse spin Hall effect. In contrast to previous studies on AFM-SHNOs that only examined uniform excitations in the macrospin approximation, we conducted theoretical and micromagnetic simulations on nano-constriction (NC) based SHNOs with uniaxial anisotropy AFM. Our results demonstrate the excitation of propagating SWs by SOT and predict a minimum threshold current with respect to NC size achievable by current nanotechnology. Additionally,

we found that the output power of the THz signal generated by uniaxial AFM-based NC-SHNOs is three orders of magnitude higher than that of biaxial AFM-based uniformly excited SHNOs. Our findings highlight the potential of uniaxial AFMs for THz SHNOs, which were previously considered unsuitable. This research advances the understanding of current-driven SWs in AFM-SHNOs, leading to the optimization of practical devices in terms of material, geometry, and frequency. The propagating SWs offer remote terahertz signal generation and efficient synchronization of SHNOs for high-power applications.

Key words: *Antiferromagnetic Magnonics, Antiferromagnetic Spintronics, Hematite, THz spin-Hall nano-oscillator*

Zusammenfassung

Kollektive Spinanregungen, die sich in magnetisch geordneten Materialien als Spinwellen (SWs) oder Magnonen ausbreiten, sind vielversprechend für die Informationsverarbeitung mit niedriger Leistung und jenseits von CMOS, die nicht unter dem ohmschen Verlust leidet. SWs in Ferromagneten (Antiferromagneten) existieren in einem Frequenzbereich von wenigen GHz (Hunderte GHz bis wenige THz) besitzen Wellenlängen im Bereich von wenigen zehn Nanometern, was etwa fünf (vier) Größenordnungen kürzer ist als elektromagnetische Wellen derselben Frequenz. Diese Eigenschaft macht SWs zu einem idealen Kandidaten für die Anwendung in der Mikrowellen- und THz-Technologie, die für die On-Chip-Verarbeitung von drahtlosen Telekommunikationssignalen unerlässlich ist. Von besonderem Interesse sind die SWs in Antiferromagneten (AFM) wegen der beiden folgenden Eigenschaften. Erstens bieten sie aufgrund vernachlässigbarer Nettomagnetisierung und der Vermeidung von dipolaren Effekten hohe Gruppengeschwindigkeiten. Zweitens können ihre THz-Frequenzen aufgrund der starken Austauschwechselwirkung genutzt werden, um die THz-Lücke zu schließen (und den Mangel an miniaturisierten Festkörper-THz-Quellen bekäupfen). In dieser Dissertation untersuchen wir SWs in AFM-Materialien hinsichtlich ihres Potenzials für i) Mikrowellen- und ii) THz-magnonische Geräte.

i) Yttrium-Eisen-Granat (YIG) gilt aufgrund seiner geringen magnetischen Dämpfung seit 1961 als „Fruchtfliege“ der Magnonik. Da es sich jedoch um einen Ferrimagneten handelt, führen dipolare Wechselwirkungen dazu, dass seine Magnonband struktur inhärent anisotrop ist und zu einer Verringerung der SW-Gruppengeschwindigkeit um eine Größenordnung auf unter 1 km/s in dünnen Filmen führt. Hier berichten wir über die Dispersionsbeziehung des niederfrequenten SW-Zweigs des natürlichen Minerals Hämatit in seiner kanten AFM-Phase. Aus Breitband-GHz-Spektroskopiemessungen und SW-Gruppengeschwindigkeiten von einigen 10 km/s, gemessen mittels wellenvektoraufgelöster inelastischer Brillouin-Lichtstreuung (BLS) bei Raumtemperatur, ermitteln wir den Dämpfungskoeffizienten von 1.1×10^{-5}. Wir schätzen die SW-Zerfallslänge bei einem kleinen Magnetfeld von 30 mT auf 1.1 cm ab. Mit einer so schnellen SW-Geschwindigkeit und geringen Dämpfung fördern unsere Ergebnisse Hämatit als alternative und nachhaltige Basis für AFM-Magnonikgeräte auf der Basis eines stabilen natürlichen Minerals.

ii) Die Weiterentwicklung kompakter und anpassungsfähiger Quellen von THz-Frequenzsignalen würde den Weg für eine Vielzahl neuartiger Anwendungen ebnen. AFM-Spintronics hat den AFM-Spin-Hall-Nanooszillator (AFM-SHNO) herorgebradt, der ein THz-Signal über die Kombination von Spin-Orbit-Torque (SOT)-induzierter selbsterhaltender THz-Spindynamik, Spin-

Pumpen und dem inversen Spin-Hall-Effekt erzeugt. Im Gegensatz zu früheren Studien zu AFM-SHNOs, die nur gleichförmige Anregungen in der Makrospin-Näherung untersuchten, führten wir theoretische und mikromagnetische Simulationen auf Nanoeinschnürungs(NC)-basierten SHNOs mit uniaxialer Anisotropie-AFM durch. Unsere Ergebnisse zeigen die Anregung sich ausbreitender SWs durch SOT und sagen einen minimalen Schwellenstrom in Bezug auf die NC-Größe voraus, die durch die aktuelle Nanotechnologie erreichbar ist. Darüber hinaus fanden wir heraus, dass die Ausgangsleistung des THz-Signals, das von uniaxialen AFM-basierten NC-SHNOs erzeugt wird, drei Größenordnungen höher ist als die von zweiachsigen AFM-basierten gleichmäßig angeregten SHNOs. Unsere Ergebnisse unterstreichen das Potenzial von uniaxialen AFMs für THz-SHNOs, die zuvor als ungeeignet galten. Diese Forschung fördert das Verständnis von stromgetriebenen SWs in AFM-SHNOs und führt zur Optimierung praktischer Geräte in Bezug auf Material, Geometrie und Frequenz. Die sich ausbreitenden SWs bieten eine ausgedehnte Terahertz-Signalerzeugung und eine effiziente Synchronisation von SHNOs für Hochleistungsanwendungen.
Stichwörter: *Antiferromagnetische Magnonik, Antiferromagnetische Spintronik, Hämatit, THz-Spin-Hall-Nanooszillator*

Résumé

Les excitations collectives de spin se propageant dans les matériaux ordonnés magnétiquement sont appelées ondes de spin (SW) ou magnons. Ils sont prometteurs pour le traitement de l'information à faible consommation d'énergie et au-delà de la technologie CMOS, qui ne souffrent pas de pertes ohmiques. Les SW dans les ferromagnétiques (antiferromagnétiques) couvrent le régime de fréquence de quelques GHz (de quelques centaines de GHz à quelques THz) et possèdent des longueurs d'onde dans la plage de quelques dizaines de nanomètres, soit environ cinq (quatre) ordres de grandeur plus courts que les ondes électromagnétiques de même fréquence. Cette propriété fait des SW un candidat idéal pour les applications dans la technologie des micro-ondes et des THz, essentielle pour le traitement intégré des signaux de télécommunication sans fil. Les SW dans les antiferromagnétiques (AFM) sont particulièrement intéressants en raison des deux propriétés suivantes. Premièrement, ils offrent des vitesses de groupe élevées en raison de l'aimantation nette négligeable et des effets dipolaires. Deuxièmement, leurs hautes fréquences dues à l'interaction d'échange forte peuvent être utilisées pour combler le vide THz (en surmontant le manque de sources THz à l'état solide de petite taille). Dans cette thèse, nous étudions les SW dans les AFM en ce qui concerne leur potentiel pour i) les dispositifs magnoniques de micro-ondes et ii) THz.

i) Depuis 1961, la grenat d'yttrium et de fer (YIG) est considérée comme la "mouche du vinaigre" de la magnonique en raison de sa faible amortissement magnétique. Cependant, en tant que ferrimagnétique, les interactions dipolaires entraînent une anisotropie inhérente de la bande de magnons, ce qui réduit la vitesse de groupe des ondes de spin d'un ordre de grandeur, en dessous de 1 km/s sous forme de film mince. Nous présentons ici la relation de dispersion de la branche à basse fréquence des ondes de spin de la phase antiferromagnétique inclinée du minéral naturel hématite. Nous avons déterminé le coefficient d'amortissement de 1.1×10^{-5} à partir de mesures de spectroscopie GHz à large bande à température ambiante. Les vitesses de groupe des ondes de spin atteignent quelques 10 km/s, mesurées au moyen de la diffusion inélastique de Brillouin résolue par le vecteur d'onde (BLS). Nous estimons la longueur de décroissance des ondes de spin à un petit champ magnétique de 30 mT à 1.1 cm. Avec une telle vitesse rapide et un faible amortissement des ondes de spin, nos résultats font de l'hématite une base alternative et durable pour les dispositifs magnoniques AFM basés sur un minéral naturel stable.

ii) L'avancée des sources compactes et adaptables de signaux électromagnétiques à haute fréquence THz ouvrirait la voie à une multitude d'applications novatrices. La spintronique AFM a introduit l'oscillateur nano spin-Hall AFM (AFM-SHNO), qui génère un signal THz

via la combinaison de la dynamique de spin auto-soutenue induite par le couple spin-orbite (SOT), le pompage de spin et l'effet Hall inverse. Contrairement aux études précédentes sur les AFM-SHNO qui ont seulement examiné les excitations uniformes dans l'approximation du macrospin, nous avons mené des simulations théoriques et micromagnétiques sur des SHNOs basés sur des nano-contraintes (NC) avec une AFM à anisotropie uniaxiale. Nos résultats démontrent l'excitation d'ondes de spin propagatives par SOT et prévoient un courant seuil minimum par rapport à la taille des NC atteignable par les nanotechnologies actuelles. De plus, nous avons constaté que la puissance de sortie du signal THz généré par les NC-SHNOs basés sur l'AFM à anisotropie uniaxiale est trois ordres de grandeur supérieure à celle des SHNOs uniformément excités basés sur l'AFM à anisotropie biaxiale. Nos résultats mettent en évidence le potentiel des AFMs uniaxiales pour les SHNOs THz, qui étaient auparavant considérées comme inadaptées. Cette recherche fait progresser la compréhension des ondes de spin entraînées par le courant dans les AFM-SHNOs, conduisant à l'optimisation des dispositifs pratiques en termes de matériau, de géométrie et de fréquence. Les ondes de spin propagatives offrent une génération de signal THz à distance et une synchronisation efficace des SHNOs pour les applications à haute puissance.

Mots clés : *Magnonique antiferromagnétique, Spintronique antiferromagnétique, Hématite, Nano-oscillateur spin-Hall THz*

List of abbreviations

SW: Spin Wave
AFM: Antiferromagnet
YIG: Yttrium iron garnet, Y3Fe5O12
BLS: Brillouin light scattering
SHNO: Spin-Hall nano-oscillator
AFM-SHNO: Antiferromagnet-based spin-Hall nano-oscillator
SOT: Spin-orbit torque
NC: Nano-constriction
NC-SHNO: Nano-constriction-based spin-Hall nano-oscillator
IoT: Internet of things
FM: Ferromagnet, ferrimagnet
CPW: Coplanar waveguide
SHE: Spin-Hall effect
HM: Heavy metal
FM-SHNO: Ferromagnet-based spin-Hall nano-oscillator
VNA: Vector network analyzer
DMI: Dzyaloshinskii-Moriya interaction
MD: Magnetic-dipole
SI: Single-ion
LLG: Landau-Lifshitz-Gilbert
AFS: Antiferromagnetic state
WFS: Weak ferromagnetic state
ISHE: Inverse spin-Hall effect
STT: Spin transfer torque
RF: Radio-frequency
SL: Signal line
GL: Ground line
DUT: Device under test
NA: Numerical aperture
WD: Working distance

OOMMF: Object Oriented MicroMagnetic Framework
XRD: X-Ray diffraction
qFM: Quasi-ferromagnetic
qAFM: Quasi-antiferromagnetic
FIB: Focused ion beam
SEM: Scanning electron microscopy
μBLS: Micro-focused Brillouin light scattering
TD-μBLS: Temperature dependent micro-focused Brillouin light scattering
HR-XRD: High-resolution X-ray diffraction
RSM: Reciprocal space mapping
AFMR: Antiferromagnetic resonance
THz-ASSW: THz antiferromagnetic Slonczewski spin wave
LLGS: Landau-Lifshitz-Gilbert-Slonczewski
FFT: Fast-Fourier-transform
PSD: Power spectral density

List of Figures

List of Tables

Contents

List of publications

First-Authored Publications

1. M. Hamdi, F. Posva and D. Grundler. Spin wave dispersion of ultra-low damping hematite (α-Fe_2O_3) at GHz frequencies. *arXiv* 2212.11887 (2022). DOI: arXiv 2212.11887

2. M. Hamdi, and D. Grundler. Terahertz Slonczewski propagating spin waves and large output voltage in antiferromagnetic spin-Hall nano-oscillators. *arXiv* 2206.07844 (2022). DOI: arXiv 2206.07844

3. M. C. Giordano*, M. Hamdi*, A. Mucchietto, D. Grundler. Magnetochiral properties of spin waves existing in nanotubes with axial and circumferential magnetization. *arXiv* 2204.12995 (2022). DOI: arXiv 2204.12995
   *equal contributions

4. J. Zhang*, M. Chen*, J. Chen*, K. Yamamoto*, H. Wang*, M. Hamdi*, Y. Sun, K. Wagner, W. He, Y. Zhang, J. Ma, P. Gao, X. Han, D. Yu, P. Maletinsky, J-P. Ansermet, S. Maekawa, D. Grundler, C-W. Nan, and H. Yu. Long decay length of magnon-polarons in $BiFeO_3$/$La_{0.67}Sr_{0.33}MnO_3$ heterostructures. *Nature Communications* **12**, 7258 (2021). DOI: 10.1038/s41467-021-27405-2
   *equal contributions

Co-Authored Publications

1. S. Watanabe, V. S. Bhat, K. Baumgaertl, M. Hamdi, and D. Grundler. Direct observation of multiband transport in magnonic Penrose quasicrystals via broadband and phase-resolved spectroscopy. *Science Advances* **7**, abg3771 (2021). DOI: 10.1126/sciadv.abg3771

2. A. Kukolova, S. E. Steinvall, R. Paul, J-B. L., P. Che, M. Hamdi, A. Mucchietto, D. Grundler, A. F. i Morral. van der Waals Epitaxy of Co_{10-x} Zn_{10-y} Mn_{x+y} Thin Films: Chemical Composition Engineering and Magnetic Properties. *The Journal of Physical Chemistry C* **125**, 9391 (2021). DOI: 10.1021/acs.jpcc.1c00452

3. N. Bazazzadeh*, M. Hamdi*, S. Park, A. Khavasi, S. M. Mohseni, and A. Sadeghi. Magnetoelastic coupling enabled tunability of magnon spin current generation in two-

dimensional antiferromagnets. *Physical Review B, Letter* **104**, L180402 (2021). DOI: 10.1103/PhysRevB.104.L180402
*equal contributions

4. N. Bazazzadeh*, M. Hamdi*, F. Haddadi, A. Khavasi, A. Sadeghi, and S. M. Mohseni. Symmetry enhanced spin-Nernst effect in honeycomb antiferromagnetic transition metal trichalcogenide monolayers. *Physical Review B* **103**, 014425 (2021). DOI: 10.1103/PhysRevB.103.014425
*equal contributions

5. M. J. K. Ashtiani, M. Mokhtarzadeh, M. Hamdi, S. M. Mohseni. Morphological magnetostatic coupling in spin valves due to anisotropic self-affine interface roughness. *Journal of Applied Physics* **127**, 095301 (2020). DOI: 10.1063/1.5143407

Part I Introductory chapters

1 Motivation and context

Modern technologies rely on materials with magnetic order (magnetic materials). Applications for these include energy-harvesting windmills, microwave components and non-volatile data storage. Nowadays, wireless communication is essential in modern society, especially as we move towards an internet of things (IoT) [3] where an increasing number of devices is connected and shares information in real time. By the end of 2019, it was estimated that there were about 8 billion active IoT devices, with a projection for this number to triple in the next 10 years [4]. Furthermore, data traffic in wireless communication networks is experiencing an explosive growth. It was estimated to account for more than 60% of the overall Internet traffic by 2021 [5]. Current research is focused on optimizing power consumption and miniaturizing microwave and THz devices to overcome these challenges. In case of microwave electronics, multi-band microwave receivers are required, but the use of fixed filter technology in their construction significantly increases the cost, size, and energy consumption of these devices [6]. To overcome the associated capacity challenges, wireless communication networks will need to exploit frequency windows of THz spectrum. However, currently there are no scalable and efficient THz sources and detectors in the frequency range of 0.1-10 THz, which is known as the THz gap [5, 7, 8].

Here, magnonic devices [9–13] offer the potential for unprecedented downsizing and low energy consumption as they employ spin waves (SWs, magnons). Spin waves are collective spin excitations in magnetically ordered materials. They typically offer frequencies in the GHz range for ferro- and ferrimagnets (FMs) and THz range for antiferromagnets (AFMs). Magnons can facilitate information transport and processing without moving electric charges, hence, avoiding joule heating. Magnons offer significantly shorter wavelengths at GHz frequencies compared to electromagnetic waves in air. This unique property is a key aspect of magnonics-based microwave technology. Furthermore, SW excitations in AFMs offer frequencies which cover perfectly the THz gap. These materials can be utilized to close the THz gap in terms of antiferromagnetic spintronic and magnonic devices [5–30]. Antiferromagnetic materials have interesting properties which could help to advance both of the abovementioned areas. This thesis addresses SWs in antiferromagnetic materials regarding their applicability in mi-

crowave and THz magnonic devices, which are contextualized in the following two sections. We reconsider arguments from our own works [14, 15].

1.1 GHz antiferromagnetic spin waves: high speed and long decay length

The development of energy efficient magnonic circuits requires isotropic spin wave dispersion relations, high group velocities, and low magnetic damping. The artificial garnet $Y_3Fe_5O_{12}$ (YIG) has long been central to the study of magnonics functionalities. In 1961, M. Sparks et al drew a comparison between the importance of YIG in ferromagnetic resonance research and the significance of the fruit fly in genetics research, highlighting the essential role that YIG plays in this field [16]. This was especially true for wafer scale high-quality YIG grown using liquid phase epitaxy. However, in a ferromagnetic material like YIG, magnon bands in the regime of small wave vectors and low GHz frequencies are inherently anisotropic due to the dipolar interaction between spins. Furthermore, moving from bulk and thick films to nanometer thin films, which is a necessary step for miniaturization of devices, the group velocity and decay length of magnons drop from about 30 km/s and 14 mm to less than 1 km/s and few 100 μm, respectively. To compensate performance reduction, researchers have developed microwave-to-magnon transducers that allow for the excitation of exchange-dominated spin waves in thin films with isotropic properties and larger group velocities. Some of these transducers involved additional ferromagnets and showed either narrow excitation bands [11, 12] or required an applied field of up to 0.1 T [13] to enable fast spin waves in thin YIG. There is a need for materials that offer spin waves with high speed over a broad range of frequencies and wave vectors, that can be accessed with standard transmission lines and coplanar waveguides (CPW) and without needing extra ferromagnetic parts.

In AFMs, the dispersion relation of spin waves is primarily determined by the huge exchange interaction, even at small wave vectors. Due to the lack of net magnetization in these materials, dipolar interactions have a negligible impact on the spin wave dispersion. Research has found that spin waves can exhibit high group velocities in antiferromagnetic materials, with reported values being comparable to those in thick YIG and as high as 30 km/s. Strikingly, one magnon branch of the canted antiferromagnet hematite (α-Fe_2O_3) provide SWs in GHz frequencies at room temperature. Because of this promising feature for GHz magnonics, hematite has got a lot of attention in recent years. Its strikingly low magnetic damping (7.8×10^{-6}) enabled already incoherent long distance spin transport and enhanced spin pumping. However, there was no experimental report on its GHz magnon band structure in wave vector ranges relevant for magnonics at the start of this PhD thesis. Exactly these considerations are the starting point for the experimental investigation of the natural mineral hematite.

1.2 Spin-Hall nano-oscillators as THz generators: propagating THz antiferromagnetic spin waves

The generation of terahertz (THz) radiation is a subject of ongoing research and development, with a variety of methods proposed and implemented to date. These include the use of free-electron lasers [17, 18], quantum cascade lasers [19, 20], superconductor Josephson junctions [21], backward-wave oscillators [18, 22], and electro-optic rectification of laser radiation [23], among others. However, it is important to note that each of these methods is associated with certain limitations and challenges, such as complex experimental setups, low temperature requirements, or large device dimensions. These factors can restrict the applicability of these methods in practical scenarios, underscoring the need for further research and development in this field. Therefore, there is an urgent need to develop small-sized solid-state THz sources and detectors.

One of the most novel sources is introduced in the field of AFM spintronics. It is called AFM spin-Hall nano-oscillator (AFM-SHNO). In an AFM-SHNO device, a spin current is generated through the spin-Hall effect (SHE) in the adjacent heavy metal (HM) layer, which subsequently enters the AFM layer and exerts a torque known as the spin-orbit torque (SOT). Theoretical studies show that above a certain threshold current, SOT can compensate the damping and induce self-sustained THz spin dynamics. The combination of the spin pumping [24, 25] and inverse SHE [26, 27] can then generate electric currents oscillating at THz frequencies. These studies suggest a great potential for AFM-SHNOs not only as dc-current driven THz sources and detectors [2, 25, 28–40] but also as ultra-fast artificial neurons that generate picosecond spikes [41, 42] which would facilitate ultra-fast neuromorphic computation [43–46]. A comparison of AFM-SHNOs with other THz sources is presented in table 1.1 [2].

Table 1.1: Frequency range and output power of AFM-SHNOs compared to other THz sources. For more detailed comparison see Ref. [2].

THz Source	Frequency Range	Output Power
AFM-SHNO	0.1-10 THz	0.1-1 μW [2]
Free Electron Laser	1-4 THz	1 W-10 kW [17, 18]
Quantum Cascade Laser	0.5-3 THz	0.1-1 μW [19, 20]
Superconducting Josephson Junction	0.1-1 THz	1 nW-1μW [21]
Backward-wave Oscillator	0.03-1.5 THz	1 mW-1 W [18, 22]
Electro-optical Laser Rectification	0.1-1 THz	1 μW-1mW [23]

It is known from the stablished knowledge of ferromagnetic (FM) SHNOs that generally these devices provide low output power. To solve this issue, a huge effort has been put into developing a synchronization scheme for FM-SHNOs which is considered the primary vehicle to achieve a sufficient signal for applications. One of the best developments with record high synchronization efficiency and number of synchronized oscillators is the use of propagating spin waves traveling from one oscillator to another. The focus of the literature on AFM-SHNOs was so far on the uniform excitations. A study on the excitation of propagating waves is

lacking. Furthermore, the existing studies have not considered a realistic SHNO incorporating a nano-constriction (NC). NCs are essential for FM-SHNOs which excite propagating SWs and enable the efficient synchronization of the oscillators granting sufficient signal quality for applications. From macrospin studies which disregard spin wave ecxitations [2, 25, 28–42] it was concluded that uniaxial AFM based SHNOs cannot generate THz output. Therefore, these studies suggested the use of biaxial AFMs, which suffer from a high threshold current.

1.3 Thesis outline

This thesis is organized as follows: In chapter 2, we will present a general overview of the principles of magnetism, with a focus on the specific concepts relevant to the research outlined in this thesis. We will cover various energy terms for a canted antiferromagnet. Then we introduce antiferromagnetic magnons in uniaxial and canted antiferromagnets.

In chapter 3, we describe the experimental methods and setups used in this thesis, including the broadband microwave spectroscopy using vector network analyzer (VNA), Brillouin light scattering and micromagnetic simulations. We also introduce sample preparation and thin film growth of Hematite.

In chapter 4, we present spin wave spectra measured in different phases of bulk hematite using VNA and BLS. In Sec. 4.1 we investigate the GHz magnon band of hematite. We measured spin wave group velocities as high as 23.3 km/s and estimated decay length up to 11 mm for relevant wave vectors for magnonic applications. In Sec. 4.2 we report on the sub-THz spin waves of bulk hematite (α-Fe_2O_3) measured by BLS below its Morin temperature.

High quality epitaxial thin films of hematite are required to realize GHz and THz applications mentioned in Sec. 1.1 and 1.2. In chapter 5 we present characterization of the grown epitaxial hematite thin films and BLS measurements on GHz magnons at room temperature for these samples. Here, we attempted to develop a recipe for growth of such thin films. We measured the GHz SWs in our grown thin films. The results indicate that despite epitaxial growth of the films, the ideal SW properties were not achieved due to substrate clamping and magnetoelastic effects. This poses significant material science challenges in the path to realize AFM magnonic devices which needs to be addressed by the community.

In chapter 6 we present our theoretical and micromagnetic study of NC based AFM-SHNOs. We investigate NC based SHNOs with uniaxial anisotropy AFM. We evidence excitation of the propagating SWs by SOT in this devices. Furthermore we show that not only the uniaxial AFMs can generate THz outputs when used in NC based SHNOs, but also the generated output is three order of magnitude larger compared to biaxial AFM based uniformly excited SHNO. This is a significant improvement on both the power consumption and the output signal of the AFM-SHNOs and draws the attention to the abandoned uniaxial AFMs which were considered not suitable for THz SHNOs.

2 Theoretical background and literature review

In this chapter we introduce the essential theoretical concepts required in the course of this thesis. In Sec. 2.1 we provide a brief introduction to magnetism and magnetically ordered materials. In order to develop a theory for canted antiferromagnets in general and hematite in particular, we introduce the various energy terms for a two sublattice model in Sec. 2.2. Then an analysis of the Morin transition [47, 48] is introduced in In Sec. 2.3 based on the magnetic free-energy formalism. In Sec. 2.4 we introduce the spin dynamics of hematite for its different magnetic phases. In Sec. 2.5 we briefly introduce spin to charge interconversion and spin-orbit torque effects. In Sec. 2.6 we review current status of research concerning structural and magnetic properties of epitaxial thin films of hematite grown by different techniques.

2.1 Introduction to Magnetism

Following quantum electrodynamics, a microscopic magnetic moment $\boldsymbol{\mu_i}$ is attributed to the spin and orbital angular momenta of electrons. The total magnetic moment $\boldsymbol{m} = \sum_i \boldsymbol{\mu_i}$ is directly proportional to the total angular momentum $\boldsymbol{J}$ via

$$\boldsymbol{m} = \gamma \boldsymbol{J}, \tag{2.1}$$

where $\gamma = -\frac{\mu_0 e g}{2m_e}$ is called the gyromagnetic ratio [49, 50]. Here $\mu_0 = 4\pi \cdot 10^{-7}$ N/A^2 is the vacuum permeability, e and m_e are the magnitude of charge and mass of electron, respectively and g is the Landé factor. Most magnetic materials are typically governed by the spin angular momentum with $\boldsymbol{J} \approx \boldsymbol{S}$ and $g \approx 2$. For an electron the spin angular momentum projected along any given direction amounts to $\frac{1}{2}\hbar$, where $\hbar$ is the reduced Planck constant. Thus the associated magnetic moment of an electron is given by $\mu_B = \frac{\hbar|e|}{2m_e} = 9.274 \cdot 10^{-24}$ J/T and is denoted as Bohr magneton. Despite the quantized nature, a classical continuum approach can be used to describe most of the magnetic properties of solids.
In a solid, spin $\boldsymbol{S}_i$ gives rise to a microscopic magnetic moment $\boldsymbol{m}_i$ which leads to the magnetization $\boldsymbol{M} = \sum_i \boldsymbol{m}_i / V$, that is the magnetic moments per volume V. The response of a magnetic

material to an applied magnetic field $\boldsymbol{H}$ is given by

$$\boldsymbol{M} = \hat{\chi}\boldsymbol{H}, \tag{2.2}$$

where $\hat{\chi}$ is the magnetic susceptibility tensor. Magnetic materials can be classified by their response to an external field. Diamagnetic materials possess no permanent magnetic moment and χ is negative and very small on the order of 10^{-5}. Paramagnetic materials possess magnetic moments which are not ordered. By application of an external field the magnetic moments are aligned into the field direction, resulting in a small macroscopic magnetization. Here, χ is positive and on the order of 10^{-4}. Ferromagnetic, ferrimagnetic and antiferromagnetic materials possess permanent magnetic moments which are ordered also without the application of an external magnetic field. The ordering is due to the quantum-mechanical exchange interaction between neighboring angular momenta. The energy of the exchange interaction is in the range of 10 to 100 meV and exceeds by far the energy of the classical dipolar interaction amounting to about 0.1 meV [50]. In ferromagnetic materials neighboring magnetic moments favored to align parallel to each other by the exchange interaction. The relative susceptibility of a strong ferromagnet is on the order of 10^6. Ferrimagnetic materials possess two different magnetic sublattices. Neighboring magnetic moments are aligned in an anti-parallel fashion, however their magnitude is different. Hence ferrimagnets show a spontaneous magnetization and their macroscopic magnetic behavior is similar to ferromagnets. Due to the partial cancelling of magnetic moments the saturation magnetization of ferrimagnets is typically smaller than for ferromagnets. In antiferromagnetic materials the exchange interaction favors an anti-parallel orientation of identical magnetic moments resulting in a vanishing macroscopic magnetization. The susceptibility of antiferromagnetic materials is positive but very small, as an external field has to act against the exchange interaction. As the antiferromagnets are at the core of the studies in this thesis, we review three main types of antiferromagnetic order in Fig. 2.1. In a C-type antiferromagnet (Fig. 2.1(a)), the coupling between spins in neighboring planes (inter-plane coupling) is ferromagnetic and the coupling within each plane (intra-plane coupling) is antiferromagnetic. In an A-type antiferromagnet (Fig. 2.1(b)), the inter-plane coupling is antiferromagnetic and the intra-plane coupling is ferromagnetic. In an G-type antiferromagnet (Fig. 2.1(c)), both the inter-plane and intra-plane couplings are antiferromagnetic. In the next section we will introduce different terms of the free energy of a prototype A-type antiferromagnet called hematite (α-Fe_2O_3) which is studied in this thesis.

2.2 Magnetic free energy of hematite: two sublattice model

The insulating antiferromagnet, hematite (α-Fe_2O_3) is the stable form of iron oxide. The crystal structure of hematite shown in Fig. 2.2 is trigonal and it belongs to the rhombohedral crystal system. It has corundum structure with the space group of $R\bar{3}c$ which has both three-fold rotational symmetry and inversion symmetry within the rhombohedral unit cell. This structure may be indexed hexagonal as well. The oxygen anions lie in hexagonal close-packed

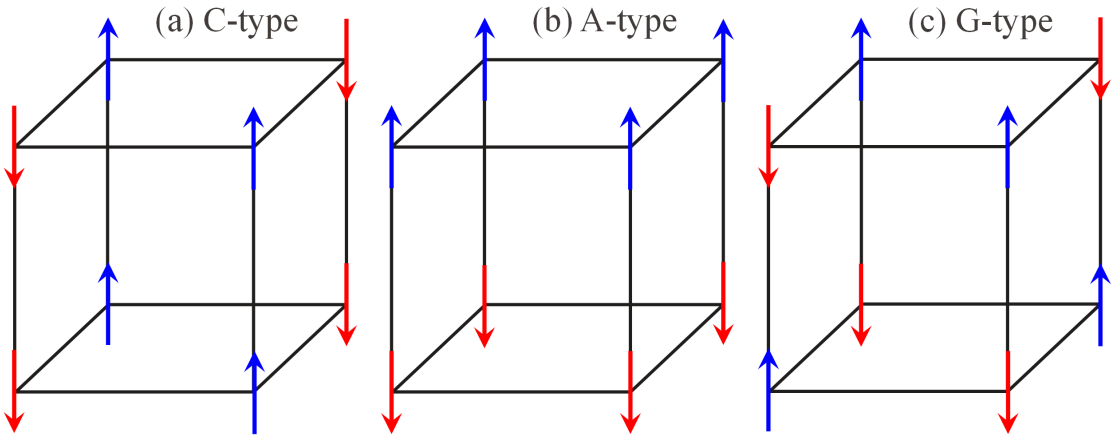

Figure 2.1: Schematics of different types of antiferromagnetic ordering.

layers and the iron cations occupy two thirds of the octahedral interstices in a symmetrical fashion. However, the six nearest neighbor oxygen ions of an iron ion suffer a slight distortion. Also, the four iron ions that surround each oxygen ion do not form a regular tetrahedron [48]. Bulk hematite has a Néel temperature $T_N \simeq 955$ K. The magnetic moments lie in the c-plane above the Morin temperature [47, 48] ($T_M \simeq 263$ K for pure α-Fe_2O_3), and along the c-axis below that temperature, as shown in Fig 2.2. We will discuss the Morin phase transition with more detail in Sec. 2.3.

Exchange interaction

As hematite is an electrical insulator, the electrons are highly localized. Since hematite is an antiferromagnet, the most important magnetic interaction must be the exchange. The Heisenberg Hamiltonian is assumed to express the exchange interaction between a pair of ferric ions, i and j, as

$$\mathcal{H}_{ij} = -J_{ij}\boldsymbol{S}_i.\boldsymbol{S}_j, \tag{2.3}$$

where $J_{ij} < 0$ for antiferromagnetism. By summation over a unit volume, V, the magnetization of each sublattice can be described as

$$\boldsymbol{M}_l = \frac{1}{V}\sum_k \boldsymbol{m}_{lk}, \tag{2.4}$$

where $\boldsymbol{m}_{lk}$ is the magnetic moment of k^{th} ion in the l^{th} sublattice with $l = 1, 2$. Now the exchange free energy density is given by

$$F_e = J_e\boldsymbol{M}_1.\boldsymbol{M}_2, \tag{2.5}$$

where J_e is the mean field coefficient relating the exchange mean field, H_E, to the sublattice magnetization.

Dzyaloshinskii-Moriya interaction

hematite possesses a small spontaneous magnetization at room temperature and above although it is basically an antiferromagnet. This weak ferromagnetism originates from a small canting of the sublattice magnetization, $\boldsymbol{M}_1$ and $\boldsymbol{M}_2$. This canting is caused by the Dzyaloshinskii-Moriya (DM) interaction [51–53] (or antisymmetric exchange interaction) which its energy density is given by

$$F_D = \boldsymbol{D}.(\boldsymbol{M}_1 \times \boldsymbol{M}_2), \tag{2.6}$$

where $\boldsymbol{D}$ is the DM vector that lies along the c-axis. Therefore, if $\boldsymbol{M}_1$ and $\boldsymbol{M}_2$ lie along c-axis, $F_D = 0$ and if $\boldsymbol{M}_1$ and $\boldsymbol{M}_2$ lie in the c-plane F_D is maximum. DM interaction originated from the combination of spin-orbit coupling and lack of inversion symmetry in the magnetic material.

Anisotropy energy

The anisotropy free energy density for a rhombohedral (hexagonal) structure such as hematite has different contributions. Along the c-axis there is a first- and second-order anisotropy given by

$$F_{K_1} = -\frac{K_1}{2}\left(\cos^2\theta_1 + \cos^2\theta_2\right), \tag{2.7}$$

$$F_{K_2} = -\frac{K_2}{2}\left(\cos^4\theta_1 + \cos^4\theta_2\right), \tag{2.8}$$

where K_1 and K_2 is the first- and second-order anisotropy constant, respectively. θ_1 and θ_2 are the polar angles that the sublattice magnetizations $\boldsymbol{M}_1$ and $\boldsymbol{M}_2$ make with the c-axis of hematite. A change in the sign of K_1 will then account for the Morin transition at zero field as we will discuss in Sec. 2.3. There is also another 6-fold crystalline anisotropy in the basal plane (c-plane) of hematite given by

$$F_B = \frac{K_B}{2}\left(\sin^6\theta_1 \cos 6\left(\phi_1 + \beta\right) + \sin^6\theta_2 \cos 6\left(\phi_2 + \beta\right)\right), \tag{2.9}$$

where K_B is the small basal plane anisotropy constant, ϕ_1 and ϕ_2 are the azimuthal angles of $\boldsymbol{M}_1$ and $\boldsymbol{M}_2$ and β is an angle from some crystallographic axis in the basal plane. It is expected that $K_B \ll K_2 \ll K_1$.

Magnetoelastic energy

The magnetostriction effects lead to an additional basal anisotropy term with strength of K_{ME} and the minimum lying along a line perpendicular to the azimuthal axis

$$F_{ME} = -\frac{K_{ME}}{2}\left(\sin^2\theta_1 \sin^2\phi_1 + \sin^2\theta_2 \sin^2\phi_2\right). \tag{2.10}$$

Zeemann energy

The interaction of the applied external magnetic field $\boldsymbol{H}$ with the sublattice magnetization provides the Zeeman term as

$$F_H = -\boldsymbol{H}.(\boldsymbol{M}_1 + \boldsymbol{M}_2)\,. \tag{2.11}$$

Total free energy and effective fields

The total magnetic energy density of hematite can be written as

$$\begin{aligned} F_T &= J_e \boldsymbol{M}_1.\boldsymbol{M}_2 + \boldsymbol{D}.(\boldsymbol{M}_1 \times \boldsymbol{M}_2) - \frac{K_1}{2}\left(\cos^2\theta_1 + \cos^2\theta_2\right) - \frac{K_2}{2}\left(\cos^4\theta_1 + \cos^4\theta_2\right) \\ &\quad + \frac{K_B}{2}\left(\sin^6\theta_1 \cos 6\left(\phi_1 + \beta\right) + \sin^6\theta_2 \cos 6\left(\phi_2 + \beta\right)\right) \\ &\quad - \frac{K_M}{2}\left(\sin^2\theta_1 \sin^2\phi_1 + \sin^2\theta_2 \sin^2\phi_2\right) - \boldsymbol{H}.(\boldsymbol{M}_1 + \boldsymbol{M}_2)\,. \end{aligned} \tag{2.12}$$

It is convenient to introduce equivalent effective fields defined as $H_E = J_e M$, $H_D = DM$, $H_{K_1} = K_1/M$, $J_{K_2} = K_2/M$, $H_B = K_B/M$ and $H_{ME} = K_{ME}/M$, where $M = |\boldsymbol{M}_1| = |\boldsymbol{M}_2|$ and $D = |\boldsymbol{D}|$. We assume an applied magnetic field in the xz-plane as $\boldsymbol{H} = H(\sin\xi\hat{\boldsymbol{x}} + \cos\xi\hat{\boldsymbol{z}})$ where ξ is the angle between $\boldsymbol{H}$ and c-axis. The reduced total energy density $f_T = F_T/M$ is given by

$$\begin{aligned} f_T \equiv \frac{F_T}{M} &= -H\left[\sin\xi\left(\sin\theta_1\cos\phi_1 + \sin\theta_2\cos\phi_2\right) + \cos\xi\left(\cos\theta_1 + \cos\theta_2\right)\right] \\ &\quad + H_E\left[\sin\theta_1\sin\theta_2\cos\left(\phi_2 - \phi_1\right) + \cos\theta_1\cos\theta_2\right] \\ &\quad - H_D\sin\theta_1\sin\theta_2\sin\left(\phi_2 - \phi_1\right) \\ &\quad - \frac{H_{K_1}}{2}\left(\cos^2\theta_1 + \cos^2\theta_2\right) - \frac{H_{K_2}}{2}\left(\cos^4\theta_1 + \cos^4\theta_2\right) \\ &\quad + \frac{H_B}{2}\left[\sin^6\theta_1\cos 6\left(\phi_1 + \beta\right) + \sin^6\theta_2\cos 6\left(\phi_2 + \beta\right)\right] \\ &\quad - \frac{H_{ME}}{2}\left(\sin^2\theta_1\sin^2\phi_1 + \sin^2\theta_2\sin^2\phi_2\right). \end{aligned} \tag{2.13}$$

2.3 Morin phase transition

The Morin transition is the temperature-driven transition from the antiferromagnetic (Fig. 2.3a) to the weak ferromagnetic state (Fig. 2.3b) or visa versa at zero field [47, 48]. It is known that K_B does not play a role in this transition. This phase transition was first explained by a change in the sign of the uniaxial anisotropy K_1 by temperature so that $K_1 > 0$ for $T < T_M$ and $K_1 < 0$ for $T > T_M$. In this explanation H_D and H_{K_2} in Eq. 2.13 were neglected and the transition happens when $K_1 = 0$. This behaviour would occur if there was two main microscopic contributions to K_1 that have opposite signs and different temperature dependencies. These two microscopic interactions were modeled as the magnetic-dipole (MD) and single-ion (SI)

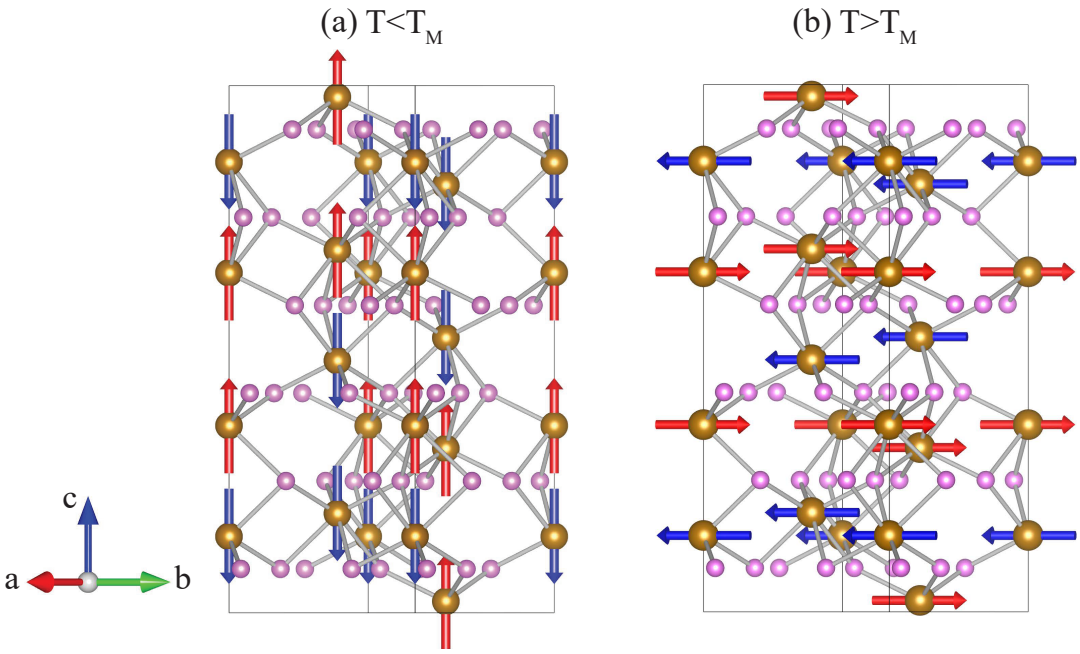

Figure 2.2: Crystal structure of hematite produced using VESTA [1]. Pink and gold spheres indicate O and Fe atoms, respectively. Magnetic ordering of hematite below (a) and above (b) The Morin temperature, $T_M \simeq 263$ K. Blue and red arrows represent two sublattices $\boldsymbol{M}_1$ and $\boldsymbol{M}_2$, respectively.

anisotropies. The mean-field approximation for the temperature dependence are given by

$$H_{MD} = H_{MD}(0) B_s^2(x), \tag{2.14}$$

$$H_{SI} = H_{SI}(0) \left[2(S+1) - 3B_s(x) \coth\left(\frac{x}{2S}\right) \right]. \tag{2.15}$$

$B_s(x)$ is the Brillouin function. The magnetic-dipole anisotropy at absolute zero, $H_{MD}(0)$ can be calculated by a summation over the hematite magnetic structure. Artman et al [47] obtain the value $\mu_0 H_{MD}(0) = -1.0045$ T. The single-ion anisotropy is then calculated by $\mu_0 H_{SI}(0) = \mu_0 (H_{K_1} - H_{MD}(0)) = 1.0268$ T. Equations 2.14 and 2.15 are ploted in Fig. 2.3a. $H_{K_1} = 0$ is indicated as intersection point with $T/T_N = 0.281$. This model predicts a Morin temperature within a few degrees of that observed. However, this good agreement clearly must be somewhat fortuitous since H_D and H_{K_2} are not negligible. The origin of K_2 is solely a single-ion contribution and is temperature dependent. The temperature dependence of the anisotropy constants is shown in Fig. 2.3b. To consider DM and the second order anisotropy, one needs to obtain the spin-flop transition for $T < T_M$ when an external field is applied along c-axis from the total free energy density 2.13. These calculations are tedious and we do not present them here, but a detailed derivation is presented in Ref. [48]. The spin flop transition of hematite is given by

$$H_{C||} = 2H_E \left(H_{K_1} + H_{K_2} \right) - H_D^2. \tag{2.16}$$

This is the external field needed to apply along c-axis to switch the magnetic moments from being along c-axis to lie in the c-plane. The Morin transition happens at zero field i.e. $H_{C||} = 0$ which results in

$$H_{K_1}^M = \frac{H_D^2 - 2H_E H_{K2}}{2H_E}. \tag{2.17}$$

T_M is obtained as the temperature where $H_{K_1}(T_M) = H_{K_1}^M$. From Ref. [48], for $\mu_0 H_E = 920$ T, $\mu_0 H_D = 2.1$ T and $\mu_0 H_{K_2} = 3.6$ T one obtain: $\mu_0 H_{K_1} = -1.1$ mT. This value is indicated in Fig. 2.3a which corresponds to $T/T_N = 0.282$. For $T_N = 965$ K it results in $T_M = 269$ K which is very close to the experimental value of $T_M = 263$ K. In Sec. 4.2 we obtain the Morin transition by measuring the sub-THz spin waves for $T < T_M$.

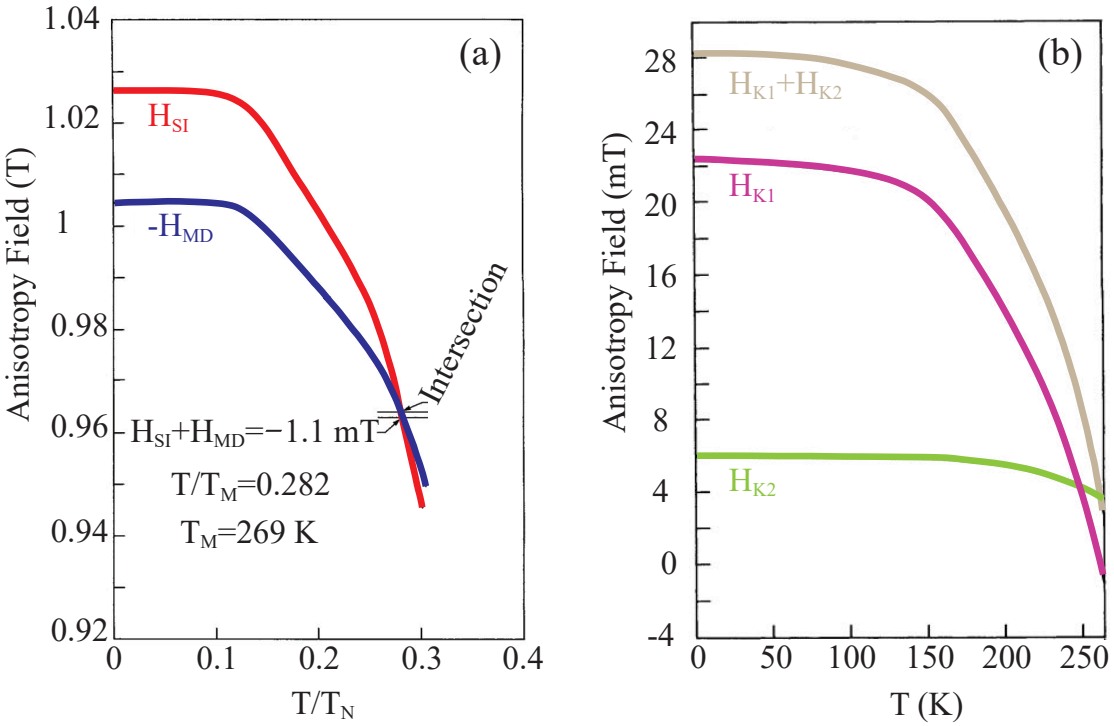

Figure 2.3: Temperature dependence of (a) single-ion (red) and magneto-dipolar (blue) contribution to the anisotropy field H_{K_1}, (b) first-order (pink) H_{K1} and second-order (green) H_{K2} fields. Gray indicates $H_{K_1} + H_{K_2}$. Figures reproduced from Ref. [48].

2.4 Spin waves in hematite

Magnetic ground state from free energy

The magnetic free energy in Eq. 2.12 is a function of the angular coordinates (θ_1, ϕ_1) and (θ_2, ϕ_2) of the two sublattice magnetizations $\boldsymbol{M}_1$ and $\boldsymbol{M}_2$, respectively. The possible equilibrium

configuration of $\boldsymbol{M}_1$ and $\boldsymbol{M}_2$ can be found from the relations

$$\frac{\partial F_T}{\partial \theta_1} = \frac{\partial F_T}{\partial \theta_2} = \frac{\partial F_T}{\partial \phi_1} = \frac{\partial F_T}{\partial \phi_2} = 0. \tag{2.18}$$

The dynamics of the sublattice magnetization $\boldsymbol{M}_i$ ($i = 1,2$) is governed by the Landau-Lifshitz-Gilbert (LLG) equation

$$\frac{d\boldsymbol{M}_i}{dt} = -\gamma \boldsymbol{M}_i \times \boldsymbol{H}_{i,eff} + \frac{\alpha}{M}\left(\boldsymbol{M}_i \times \frac{d\boldsymbol{M}_i}{dt}\right), \tag{2.19}$$

where $\boldsymbol{H}_{i,eff} = -\frac{\delta F_T}{\delta \boldsymbol{M}_i}$ is the effective field of sublattice i and α is the Gilbert damping. Neglecting the damping term the equation of motion in the polar coordinates is given by

$$\frac{d\theta_i}{dt} = \gamma H_{\phi ie}, \tag{2.20}$$

$$\sin\theta_i \frac{d\phi_i}{dt} = \gamma H_{\theta ie}, \tag{2.21}$$

where $H_{\phi ie} = -\frac{\partial F_T}{\partial \phi_i}$ and $H_{\theta ie} = -\frac{\partial F_T}{\partial \theta_i}$ are the ϕ and θ components, respectively, of the effective field along the sublattice i. In other words, Eq. 2.18 means that at equilibrium the effective sublattice fields vanish. Equation 2.18 is a necessary but not a sufficient condition for the minimum of the free energy. In order to ensure an energy minimum solution, together with Eq. 2.18 the determinant of the second derivatives must satisfy the following condition

$$\begin{vmatrix} F_{T\theta_1\theta_1} & F_{T\theta_1\theta_2} & F_{T\theta_1\phi_1} & F_{T\theta_1\phi_2} \\ F_{T\theta_2\theta_1} & F_{T\theta_2\theta_2} & F_{T\theta_2\phi_1} & F_{T\theta_2\phi_2} \\ F_{T\phi_1\theta_1} & F_{T\phi_1\theta_2} & F_{T\phi_1\phi_1} & F_{T\phi_1\phi_2} \\ F_{T\phi_2\theta_1} & F_{T\phi_2\theta_2} & F_{T\phi_2\phi_1} & F_{T\phi_2\phi_2} \end{vmatrix} > 0, \tag{2.22}$$

with $F_{Txy} = \partial^2 F_T / \partial x \partial y$ being the second derivatives of F_T. A detailed derivation is presented in Ref. [48]. Here, we review the result. For the antiferromagnetic state (AFS) when $T < T_M$ and $H < H_{C||}$ applied along the c-axis ($\xi = 0$), energy minimization leads to $\theta_1 = \pi$, $\theta_2 = 0$ and $\tan\left(\phi_2 - \phi_1\right) = -H_D / H_E$. For the weak ferromagnetic state (WFS) when $T > T_M$ and for an arbitrary ξ, the equilibrium state is given by $\theta_1 = \theta_2 = \theta$ with $\theta \simeq \pi/2$, $\phi_2 = \phi$, $\phi_1 = 2\pi - \phi$ with $\phi \simeq \pi/2$. Considering the orders of magnitude of the different effective fields (in T) as below

$$\begin{aligned} &H_E(\sim 10^3) \gg H(\sim 10^{-1} \text{ to } 10) \simeq H_D(1), \\ &H, H_D \gg H_{K_1}(10^{-2}) \simeq H_{K_2}(\sim 10^{-3} \text{ to } 10^{-2}), \\ &H_{K_1}, H_{K_2} \gg H_{ME}(10^{-4}) \simeq H_B(10^{-5}). \end{aligned} \tag{2.23}$$

The values of θ and ϕ are given by

$$\cos\theta = \frac{H\cos\xi}{2H_E} \qquad \text{and} \tag{2.24}$$

$$\cos\phi = \frac{H\sin\xi + H_D}{2H_E}. \tag{2.25}$$

Spin waves

If the deflections from equilibrium $\delta\theta_i = \theta_i(t) - \theta_{0i}$ and $\delta\phi_i = \phi_i(t) - \phi_{0i}$ are small one can write the equation of motion as

$$\begin{aligned}
-M\sin\theta_1\delta\dot{\phi}_1/\gamma &= F_{T\theta_1\theta_1}\delta\theta_1 + F_{T\theta_1\theta_2}\delta\theta_2 + F_{T\theta_1\phi_1}\delta\phi_1 + F_{T\theta_1\phi_2}\delta\phi_2,\\
-M\sin\theta_2\delta\dot{\phi}_2/\gamma &= F_{T\theta_2\theta_1}\delta\theta_1 + F_{T\theta_2\theta_2}\delta\theta_2 + F_{T\theta_2\phi_1}\delta\phi_1 + F_{T\theta_2\phi_2}\delta\phi_2,\\
M\sin\theta_1\delta\dot{\theta}_1/\gamma &= F_{T\phi_1\theta_1}\delta\theta_1 + F_{T\phi_1\theta_2}\delta\theta_2 + F_{T\phi_1\phi_1}\delta\phi_1 + F_{T\phi_1\phi_2}\delta\phi_2,\\
M\sin\theta_2\delta\dot{\theta}_2/\gamma &= F_{T\phi_2\theta_1}\delta\theta_1 + F_{T\phi_2\theta_2}\delta\theta_2 + F_{T\phi_2\phi_1}\delta\phi_1 + F_{T\phi_2\phi_2}\delta\phi_2,
\end{aligned} \tag{2.26}$$

where $\delta\dot{\theta}_i = d\theta_i/dt$, $\delta\dot{\theta}_i = d\phi_i/dt$. This system of homogeneous equations has periodic solutions of the form $\delta\theta_i(t) = \delta\theta_i(0)e^{i\omega t}$ and $\delta\phi_i(t) = \delta\phi_i(0)e^{i\omega t}$ with the frequency ω. These frequencies can be determined by setting the determinant of equation 2.26 equal to zero. For the AFS, the resonance frequencies of two modes are given by

$$f_1 = \left(\frac{\gamma}{2\pi}\right)\sqrt{2H_E\left(H_{K_1} + H_{K_2}\right) - H_D^2} + H \qquad \text{and} \tag{2.27}$$

$$f_2 = \left(\frac{\gamma}{2\pi}\right)\sqrt{2H_E\left(H_{K_1} + H_{K_2}\right) - H_D^2} - H. \tag{2.28}$$

In the WFS the resonance frequencies of the modes are as follows

$$f_1 = \left(\frac{\gamma}{2\pi}\right)\sqrt{H\sin\xi\left(H\sin\xi + H_D\right) + 2H_E\left(18H_B\cos 6\beta + H_{ME}\right)} \qquad \text{and} \tag{2.29}$$

$$f_2 = \left(\frac{\gamma}{2\pi}\right)\sqrt{H_D\left(H_D + H\sin\xi\right) + H^2\cos^2\xi + 2H_E\left(3H_B\cos 6\beta - H_{K_1} + H_{ME}\right)}. \tag{2.30}$$

In this thesis we study the mode in Eq. 2.29 at room temperature in Sec.4.1 for a bulk sample and Sec. 5.2 for thin films of Hematite. The high frequency mode in WFS Eq. 2.30 was not observed in our Brillouin light scattering (see methods Sec. 3.2) measurements. We also study the modes Eq. 2.27 and 2.28 at zero field at cryogenic temperatures for the bulk sample.

2.5 Spin to charge interconversion and spin-orbit torque

Spin Hall effect

The spin Hall effect (SHE) is a phenomenon where a transverse spin current, $\boldsymbol{j}_s$, is generated in response to a longitudinal electric current, $\boldsymbol{j}_c$, flowing through a non-magnetic material

with strong spin-orbit interaction e.g heavy metals (HM). The effect was first predicted by D'yakonov and Perel in semiconductors [54] and later rediscovered by Hirsch and Zhang in metals [55, 56]. Such spin current results in the accumulation of spins, $\boldsymbol{\mu}_s$, on the edges of the material as indicated in Fig. 2.4(a). This effect arises as the spin-orbit interaction causes the electrons to deflect perpendicular to the direction of the electric current flow in the opposite direction depending on their spin orientation. There exists a reverse phenomenon in the same material called inverse SHE (ISHE) in which a spin current injected into HM generates a transverse charge current as depicted in Fig. 2.4(b).
SHE is a central phenomenon in modern spintronics as it allows the spin to charge current interconversion which facilitates electrical creation and detection of pure spin currents. The conversion efficiency between the charge current, $\boldsymbol{j}_c = \boldsymbol{j}_\uparrow + \boldsymbol{j}_\downarrow$, and the spin current, $\boldsymbol{j}_s = \boldsymbol{j}_\uparrow - \boldsymbol{j}_\downarrow$, where $\boldsymbol{j}_{\uparrow(\downarrow)}$ represents the current of spin up (down) electrons is called the spin Hall angle, θ_{SH}. The spin to charge interconversion is given by

$$\boldsymbol{j}_s \propto \theta_{SH}\left(\boldsymbol{j}_c \times \boldsymbol{p}\right), \tag{2.31}$$

$$\boldsymbol{j}_c \propto \theta_{SH}\left(\boldsymbol{j}_s \times \boldsymbol{p}\right), \tag{2.32}$$

where $\boldsymbol{p}$ is the spin polarization direction of the spin current.

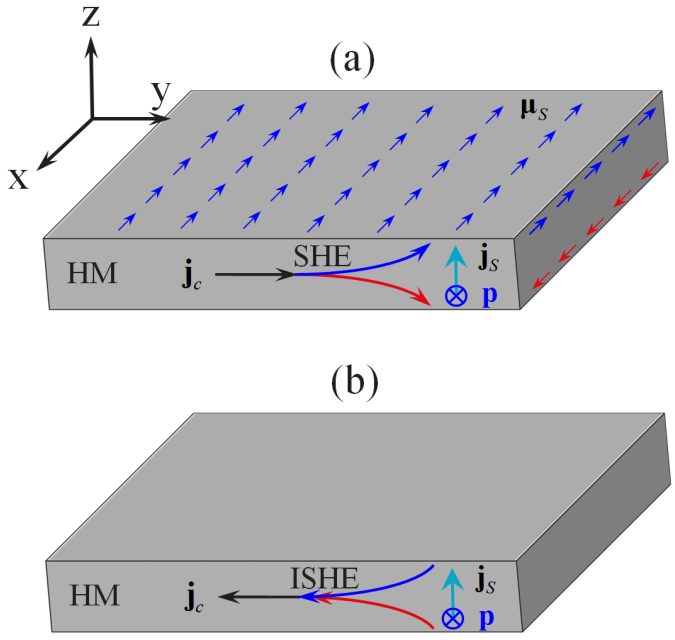

Figure 2.4: (a) Schematics of SHE in a HM. A charge current, $\boldsymbol{j}_c$, (black arrow) generates a transverse spin current, $\boldsymbol{j}_s$, (cyan arrow) flowing in perpendicular direction with spin polarization, $\boldsymbol{p}$. Red and blue curved arrows indicate the deflected trajectories of spin up and spin down electrons. Small straight red and blue arrows indicate spin accumulations generated on the surfaces of the HM layer. (b) Schematics of ISHE in a HM. An injected spin current, $\boldsymbol{j}_s$, (cyan arrow) with spin polarization, $\boldsymbol{p}$, generates a transverse charge current, $\boldsymbol{j}_c$, (black arrow) flowing in perpendicular direction.

Spin-orbit torque and spin pumping

In seminal papers in 1996, Slonczewski [57, 58] and Berger [59, 60] independently predicted that current flowing perpendicular to the plane in a metallic multilayer comprised of alternating magnetic and non-magnetic metals can generate a torque on the magnetization of the magnetic layers by transferring spin angular momentum to the localized moments via s-d exchange coupling. This torque called spin transfer torque (STT) [61, 62] is strong enough to reorient the magnetization in the magnetic layer. Such torque can also result from the spin current generated via SHE and injected to an adjacent magnetic material. In this case the torque is called spin-orbit torque (SOT) [63–66]. In both cases of STT and SOT the torque acting on sublattice i of the magnetic material is given by

$$\boldsymbol{\tau}_{s,i} = \beta(j_c)\, \boldsymbol{M}_i \times \left(\boldsymbol{M}_i \times \boldsymbol{p}\right). \tag{2.33}$$

Here, $\beta(j_c)$ is the applied electric perpendicular to the plane of multilayer or in the HM layer in case of STT or SOT, respectively. $\beta(j_c)$ is directly proportional to the applied current density j_c and has different prefactors for STT and SOT. In this thesis we focus on SOT where the prefactors will be given in chapter 6. $\boldsymbol{M}_i$ is the magnetization of sublattice i in the magnetic material and $\boldsymbol{p}$ is the spin polarization of the current or the spin accumulation for STT and SOT, respectively.
When a normal conductor is adjacent to a magnetically ordered material, the spin dynamics in the magnet generates a flow of spin angular momentum from the magnet into the normal conductor through the interface, resulting in the creation of spin current. This phenomenon that is called spin pumping first predicted and observed by Silsbee [67] and later reformulated in Refs. [68, 69] can enhance the magnetic damping. The spin current generated by sublattice i of the magnetic material via spin pumping is given by

$$\boldsymbol{j}_{sp,i} = G_r \left(\boldsymbol{m}_i \times \frac{d\boldsymbol{m}_i}{dt}\right) - G_i \frac{d\boldsymbol{m}_i}{dt}, \tag{2.34}$$

where $\boldsymbol{m}_i$ is the direction of the sublattice magnetization and G_r (G_i) is the real (imaginary) part of the spin mixing conductance that describes the spin conductivity of the interface between the magnet and the normal conductor [68, 69]. Often G_i is negligible compared to G_r.

2.6 Hematite thin films in the literature

There are many reports on epitaxial growth of hematite thin films in the literature. Here we review some of these literature in terms of the structural and magnetic properties of the grown films. All the methods used c-plane Sapphire (Al_2O_3) as substrate. Fujii et al [70] reported epitaxial growth of hematite thin films using reactive vapor deposition at 450 °C. They annealed the grown films ex-situ in air for one day. The films showed a high level of epitaxy both in plane and out of plane and did not show any Morin transition. Reactive dc

magnetron sputtering was used by others [13, 71, 72] with substrate temperature in the range 300-800 °C with the best results at 600 °C. Here highly strained films obtained for thicknesses below 16 nm and no Morin transition observed. Park et al [73] demonstrated strain control of Morin transition by growing a 15 nm Cr_2O_3 buffer layer between hematite thin film and the substrate. The α-Fe_2O_3 (Cr_2O_3) films were grown by consecutive cycles of Fe (Cr) evaporation under O_2 and following 60 min post-oxidation in O_2 at 630 °C. In each cycle, a 3 nm thick layer was grown. Morin temperature in these films was in the range of 360 K to 250 K for the film thicknesses of 3 nm to 24 nm, respectively. No Morin transition was observed for non-buffered films. Shimomura et al used reactive radio-frequency (RF) magnetron sputtering [74, 75] with a substrate temperature of 500 °C where they observed a Morin transition of 180 K for 100 nm thin films. Others have reported epitaxial films grown by off-axis sputtering from a stoichiometric target at 500-640 °C [76–79]. No Morin transition was reported on these films. In case of Ref. [79] the substrate clamping effect on the magnetic texture was reported. Here the authors showed that despite having a relaxed growth of the 10 nm across the thickness of the film, at the substrate-film interface it was experiencing a strain due to clamping on the substrate. They showed that the formation of domains did not follow the hexagonal crystal symmetry of the *c*-plane and was predominantly driven by destressing fields. They also reported a non-homogeneous distribution of strain in the film. For the thin films grown by pulse laser deposition the Morin transition is reported [80–83]. In Ref. [80] where the deposition is done at 800 °C, the transition takes place over a relatively broad temperature rang which is correlated with a variation in the out-of-plane axis of the film. In Ref. [82] the transition was reported to be very sharp in films with thicknesses of (20-45 nm) and was shown that it can be controlled by Hydrogen doping. In Ref. [81] Jani et al report observation of antiferromagnetic half-skyrmions and bimerons in the same films. They also showed that despite having a relaxed growth of the film, the full saturation of the hematite film was not possible for the fields up to 500 mT and there was some remaining noncolinear texture in the magnetic structure even at such fields. In Ref. [83] Kan et al report a triaxial magnetic anisotropy in 70nm thin films. The reported Morin temperature depended on the substrate temperature during the growth. Zhang et al [84] reported hematite thin film growth by RF magnetron sputtering from a stoichiometric target at room temperature and annealing in a furnace for 60 min in 50% N_2 and 50% O_2 at 900 °C. These films did not show Morin transition.

3 Experimental and Numerical Methods

In this chapter we present experimental techniques and numerical methods used in this thesis: Sec. 3.1 introduces the broadband microwave spectroscopy using vector network analyzer (VNA). In Sec. 3.2 we present Brillouin light scattering (BLS) at room and cryogenic temperatures. In Sec. 3.3 we introduce the micromagnetic simulations used in this thesis. In the Sec. 3.4, the fabrication process for epitaxial thin films of hematite is presented.

3.1 Broadband microwave spectroscopy

In this thesis we apply broadband microwave spectroscopy in the flip-chip configuration with a coplanar waveguide (CPW) [Fig. 3.1]. By means of the CPW a high frequency magnetic field, $\mathbf{h}_{\mathrm{rf}}$, is applied while the absorption is being measured by a vector network analyzer (VNA). The CPW (see Fig. 3.1(b)) is a type of transmission line made up of a central conductor or signal line (SL) that is sandwiched between two parallel shielding conductors, often referred to as ground line (GL). The geometry of the CPW is optimized to match the impedance of the measurement system, which in this case is 50 Ω for the VNA. The calculation of the impedance of a CPW can be found in reference [85]. I used a CPW with SL and GL widths of 165 μm and 295 μm, respectively with a gap width of 30 μm. We received different pieces of the same hematite bulk crystal from Prof. J.-P. Ansermet and Dr. M. Bialek at EPFL. The sample was an a-plane natural crystal of hematite which is available commercially at SurfaceNet GmbH [86]. Figure 3.1(a) illustrates a sketch of the VNA measurement setup used. The VNA equipment model is Agilent PNA-X N-5242A. The VNA allows the application of microwave signals within a wide range of frequencies, from 10 MHz up to 26.5 GHz, at its two RF ports. Additionally, it has the capability of detecting incoming voltages with high precision in both signal level and phase.

The VNA measures scattering (S) parameters between port 1 and port 2. The S-parameters for

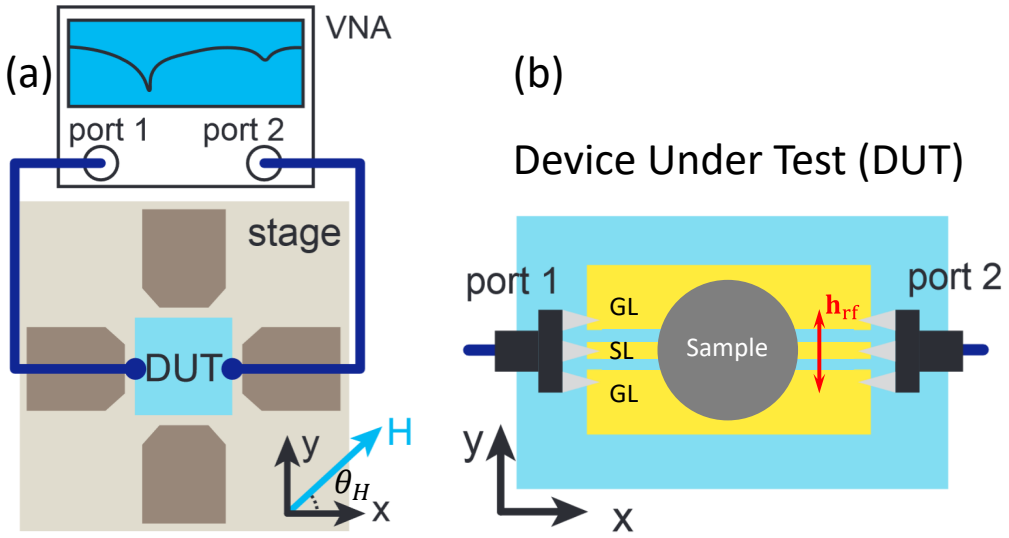

Figure 3.1: (a) Sketch of the VNA setup in a typical measurement configuration. Port 1 and 2 of a VNA are connected with RF cables and tips to a CPW placed under the sample. Microwave absorption is characterized by measuring scattering parameters S_{11} and S_{21} with the VNA. A magnetic field $\mu_0\mathbf{H}$ is applied in any in-plane angle θ_H by using a two-axis electromagnet system. The field is calibrated by a Hall-sensor placed directly under the device under test (DUT). (b) Schematics of DUT where the sample is placed on the CPW in flip-chip configuration. Ends of the CPW are connected to VNA via RF tips.

a two-port network are defined by a scattering matrix as [87]:

$$\begin{pmatrix} V_1^- \\ V_2^- \end{pmatrix} = \begin{pmatrix} S_{11} & S_{12} \\ S_{21} & S_{22} \end{pmatrix} \begin{pmatrix} V_1^+ \\ V_2^+ \end{pmatrix}. \tag{3.1}$$

V_1^+ (V_2^+) is the voltage applied by the VNA at port 1 (port 2), while V_1^- (V_2^-) represent the voltage detected at port 1 (port 2). If the output at port 2 is switched off ($V_2^+ = 0$), Eq. 3.1 leads to $S_{11} = V_1^-/V_1^+$ and $S_{21} = V_2^-/V_1^+$. Such parameters detected as a function of frequency f give rise to the spin-were spectra presented in this work. Note that S-parameters are unitless complex numbers and are either described by magnitude $|S_{ij}|$ and phase Φ_{ij}, or by its real part $\mathrm{Re}(S_{ij})$ and an imaginary part $\mathrm{Im}(S_{ij})$.

In a the flip-chip configuration, both ports are connected via microwave cables and RF tips to the CPW. When the microwave signal is applied to CPW, a microwave current passes through it and creates a dynamic magnetic field, $\boldsymbol{h}_{\mathrm{rf}}$, in its vicinity. $\boldsymbol{h}_{\mathrm{rf}}$ exerts a torque on the magnetic moment in the sample. When the resonance condition is met, absorption increases and measured both in reflection, S_{11}, and transmission, S_{21}. $\boldsymbol{h}_{\mathrm{rf}}$ generated by a CPW is displayed in Fig. 3.2(a). In plane and out of plain components of $\boldsymbol{h}_{\mathrm{rf}}$ underneath the CPW are sketched in Fig. 3.2(b).

The magnet system consisted of two perpendicularly mounted electromagnets, allowing for a field $\mathbf{H}$ application in all in-plane angles θ_H (Fig. 3.1(a)). Each of the two field axes is driven by a Kepco bipolar power supply, respectively. The power supplies enabled a seamless transition

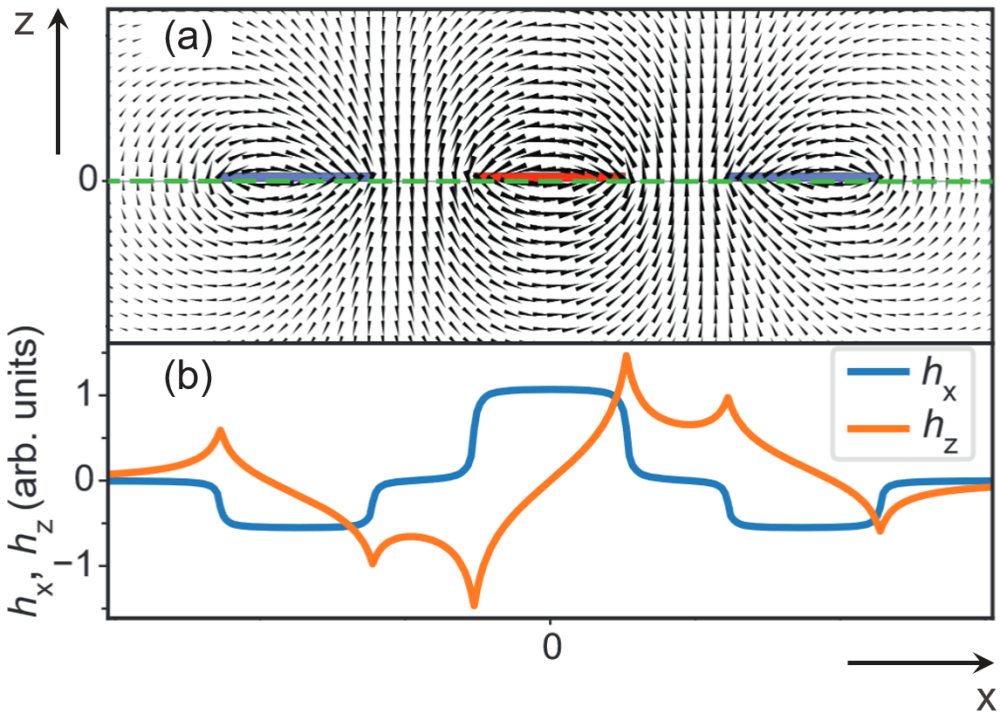

Figure 3.2: (a) Sketch of the cross-section of a CPW in the xz-plane. Black arrows represent $\boldsymbol{h}_{\mathrm{rf}}(x,z)$ where the length of the arrows represents logartithmically scaled $|\boldsymbol{h}_{\mathrm{rf}}|$. The current in the signal line (red) is flowing in the opposite direction of the current in the ground lines (blue). (b) The blue and orange curves are the line plot of x and z component of $\boldsymbol{h}_{\mathrm{rf}}$, respectively, at $z = 0$ underneath the CPW (green dashed line in (a)). The picture is adopted from the PhD thesis of K. Baumgärtl [88].

of the output currents applied to the field coils, resulting in a smooth transition of the magnetic field from positive to negative values across zero field without interruption. The magnetic field is continuously monitored by a two-axis Hall-sensor, which is mounted directly beneath the sample location. The Hall voltages are amplified and utilized as a feedback mechanism for the power supplies. The control computer inputs a set voltage which corresponds to the desired magnetic field $\mu_o \boldsymbol{H}$. The power output is adjusted to bring the set and reference values in alignment. This feedback loop utilizing the Hall sensor allows for precise control of the applied magnetic field and minimizes nonlinear effects in the pole shoes such as hysteresis. The control computer allows to program automatic field sweeps and angle sweeps and reads the measured S-parameters from the VNA. The magnet system supports a maximum field of $|\mu_0 \boldsymbol{H}_{\mathrm{max}}| = 90$ mT.

3.2 Brillouin light spectroscopy

Brillouin light scattering spectroscopy (BLS), also known as Brillouin-Mandelstam scattering, is an optical spectroscopy technique. It is named after Brillouin [89] and Mandelstam [90],

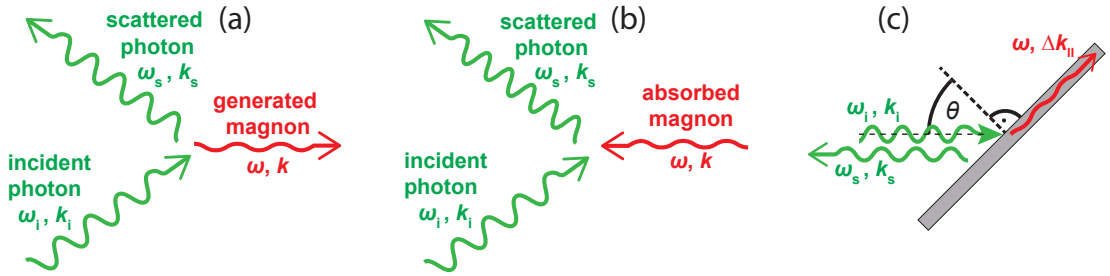

Figure 3.3: Illustration of **a** the Stokes scattering process, in which a magnon is generated **b** and the anti-Stokes scattering process, in which a magnon is absorbed. **c** Sketch of the employed measurement configuration for wave vector resolved BLS in reflection geometry. Laser light impinges on the sample surface with an incident angle θ. Back-reflected light with $\boldsymbol{k}_\mathrm{s} \parallel \boldsymbol{k}_\mathrm{i}$ is guided to the interferometer and analyzed. In the scattering process, the photon wave vector parallel to the sample surface was changed by $-\Delta k_\parallel$, which is transferred to the generated magnon. $\Delta k_\parallel$ can be adjusted by changing θ and reaches maximally two times the photon momentum for $\theta = 90°$. The picture is adopted from the PhD thesis of K. Baumgärtl [88].

who independently predicted light scattering from acoustic phonons in the 1920s. BLS is usually differentiated from Raman scattering by the relevant frequency range [91]. While Raman grating spectrometers measure shifts of the photon energy in the tens of THz regime, BLS refers to the detection of energy shifts of the scattered light in the GHz regime [91]. High frequency resolution and high contrast spectrometers are required to distinguish between GHz-shifted light from elastically scattered Rayleigh light. An optimized multipass Fabry-Pérot interferometer developed by J. Sandercock [92] makes BLS detection feasible down to frequency shift of 0.5 GHz. Nowadays it is widely used in BLS setups for the investigation of spin waves (SWs). Details on the working principle of the interferometer can be found in Refs. [93, 94]. The aim of this section is to decribe the basic working principles of BLS and the BLS setup used in this thesis, located in the LMGN laboratories. We discuss the wave vector resolved BLS and the cryogenic BLS microscopy setup used in this thesis.

Magnon-photon scattering

In a quantum mechanical framework, the scattering of photons with magnons can be seen as the interaction of quasiparticles, as illustrated in Fig. 3.2. The incident photon, possessing energy $\hbar\omega_i$ and wave vector k_i, can either create or annihilate a magnon with energy $\hbar\omega$ and wave vector k. The creation process is referred to as Stokes scattering, while the annihilation process is referred to as anti-Stokes scattering. In the former, the scattered photon loses energy, while in the latter, it gains energy. As energy and momentum are conserved in both scenarios, the scattered light carries information about the probed magnon. The energy $\hbar\omega_s$ and wave

vector k_s of the scattered light is given by

$$\hbar\omega_\mathrm{s} = \hbar\omega_\mathrm{i} \pm \hbar\omega, \tag{3.2}$$

$$\boldsymbol{k}_\mathrm{s} = \boldsymbol{k}_\mathrm{i} \pm \boldsymbol{k}. \tag{3.3}$$

The wave vector conservation stated in Eq. 3.3 applies in the presence of translational invariance. In the course of the thesis we study bulk or thin film hematite with a penetration depth of 75 nm [95] for the green laser used. Here only the wave vector component parallel to the sample surface is conserved. Figure 3.3c shows a typical measurement configuration for wave-vector resolved BLS on a reflective sample. Monochromatic laser light is focused on the sample with an incident angle θ defined in respect to the surface normal of the sample. According to the law of reflection, elastically scattered light is reflected on the opposing side of the surface normal. The angle between incident and elastically reflected beam amounts to 2θ. Instead, in the used measurement configuration, light scatters with $\boldsymbol{k}_\mathrm{s} \parallel \boldsymbol{k}_\mathrm{i}$ is collected and analyzed. Here the photon wave vector parallel to the sample surface $k_\parallel$ was changed during the scattering process. The transferred momentum $\Delta k_\parallel$ is given by [96]

$$\Delta k_\parallel = 2k_\mathrm{i} \sin\theta. \tag{3.4}$$

$\Delta k_\parallel$ is either absorbed or transferred by a magnon depending on whether the Stokes or anti-Stokes process is considered. The magnitude of the wave vector of the incident light is given by $k_\mathrm{i} = 2\pi/\lambda_\mathrm{L}$, where λ_L is the laser wave length. Measurements in this thesis were conducted with solid-state lasers with $\lambda_\mathrm{L} = 532$ nm. Photons can maximally transfer two times their wave vector which amounts to $k_\mathrm{max} = 23.6\ \mathrm{rad}/\mu\mathrm{m}$ for the used laser wave length. Usually the signal strength in wave-vector resolved BLS measurements drops significantly above $\theta = 70$ degrees. Due to the elongation of the laser spot, the transferred wave vector is not well defined. The BLS setup at LMGN is equipped with a piezoelectric rotary positioner (SmarAct SR-2013-S-NM) which enables an angular resolution of 25 μdeg for θ. Equipped with an objective lens with numerical aperture of 0.18, the spot size for wave vector resolved BLS with green light is 1.5 μm. In order to discriminate between magnons and other collective excitations like phonons, the scattered beam is sent through a polarization analyzer and only the cross-polarized light (with respect to the incident beam) enters the interferrometer. This is because magnons transfer their angular momentum to the scattered photon which results in a 90 degree rotation of the polarization of the scattered photons. Magnetic field and temperature dependent measurements can also discriminate between magnons and phonons. The magnon frequency changes with magnetic field and in most cases with temperature, whereas phonon frequencies often are insensitive to these external parameters.

Cryogenic micro-focus Brillouin light scattering microscopy

We use a Mitutoyo M Plan Apo SL 100x objective lens with NA = 0.55 (numerical aperture) and WD = 13 mm (working distance) that focuses the laser light on a sample residing in a cryostat (Fig. 3.4). At the same time, the optical images are taken by a CCD camera so we can locate the laser position during the measurements. Combined with the piezoelectric stages underneath the sample, a scanning function is achieved to explore micro- and nanostructures. A cryostat with a closed-loop helium circle was integrated with the BLS setup for exploring spin dynamics at cryogenic temperatures (Fig. 2.7). The basement is cooled by the compressed helium gas down to about 4.5 K. It further cools down the whole stage as a cold finger. Both the basement and the holder stage are made of Cu to guarantee good thermal conductivity. The sample is placed on top of the holder stage consisting of a three-axis piezo-positioner and the temperature controlling chip carrier. I integrated the computer control of the piezoelectric stages of the cryostat into the LabView VI of the BLS setup. The chip carrier contains a thermal sensor and a heater. They are directly buried underneath the sample so the control of the sample temperature is achieved by varying a proportional–integral–derivative controller. In this thesis we use the set nominal temperatures for all the discussions. The green laser is incident normal to the top surface of the sample and focused through a window.

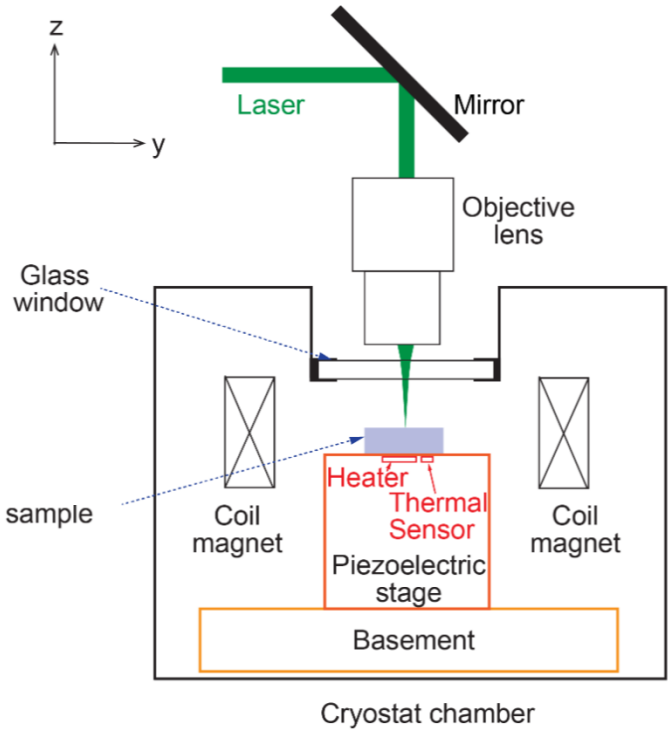

Figure 3.4: Illustration of the cryostat installed on the BLS setup in incorporating a piezoelectric scanning stage. Picture is adopted from PhD thesis of P. Che [97]

3.3 Micromagnetic simulations

At the time that we started the study presented in chapter 6 there was no micromagntic simulation packages developed for AFM materials. There were few studies that used the Object Oriented MicroMagnetic Framework (OOMMF) [98], a micromagnetic code that solves the Landau-Lifshitz-Gilbert (LLG) equation based on the finite difference method and is widely used to study FM materials. For micromagnetic simulations on AFMs a negative exchange constant was introduced [99, 100]. In chapter 6 we use the same approach and employ OOMMF to study the AFM-based spin-Hall nano-oscillators. The relation between this negative exchange constant and the effective homogeneous and non-homogeneous exchange interaction of an AFM was not clear in the beginning. In Appendix A.2 we show the mathematical equivalence between the energy terms that OOMMF is dealing with and a two sublattice model for an antiferromagnet and obtain the relation of this negative exchange in OOMMF with the exchange terms of a two-sublattice model AFM. Latter a micromagnetic simulation package called Boris Computational Spintronics that incorporates a two sublattice AFM model was developed by S. Lepadatu [101]. Boris is a multi-physics magnetisation dynamics and spin transport simulation software. Below we report an excellent agreement of the analytical results and OOMMF simulations with the two sublattice micromagnetic simulations done by Boris for a standard micromagnetic problem (namely the calculation of the spin wave dispersion). These simulations together with our derivations in Appendix A.2 proves that the negative exchange model of OOMMF is mathematically, numerically and physically equivalent to a two sublattice G-type (Fig. 3.5) antiferromagnet.

Micromagnetic simulations performed via OOMMF and Boris and their comparison

Below we show a snapshot of the magnetic configuration of a stripe with dimensions 4 μm$\times$ 20 nm$\times$1 nm [along x, y and z direction] after energy minimization by OOMMF in Fig. 3.5. The simulation material parameters are given in Sec. 6. Uniaxial anisotropy direction (x) is in the xy-plane and along the long edge of the picture. Orange and green squares represent the cells with dimensions of 1 nm$\times$1 nm$\times$1 nm corresponding to two different sublattices of the two sublattice antiferromagnet. Blue and red arrows represent the magnetization vectors in each cell which as expected, arrange antiferromagnetically and are parallel to the easy axis. This magnetic configuration is a G-type antiferromagnet.

In order to further verify our micromagnetic simulations, we solve a standard micromagnetic problem using OOMMF and a reference micromagnetic simulation package. Boris [101] solves the full two sublattice model. Following Eq. 2.19, the micromagnetic equations for the two sublattice model are given by [34, 101]

$$\frac{d\mathbf{m}_i}{dt} = -\gamma \mathbf{m}_i \times \mathbf{H}_{i,eff} + \frac{\alpha}{M_s}\left(\mathbf{m}_i \times \frac{d\mathbf{m}_i}{dt}\right), \tag{3.5}$$

where we use $\mathbf{m}_i$ as the unit vector along the sublattice magnetization. The exchange effective

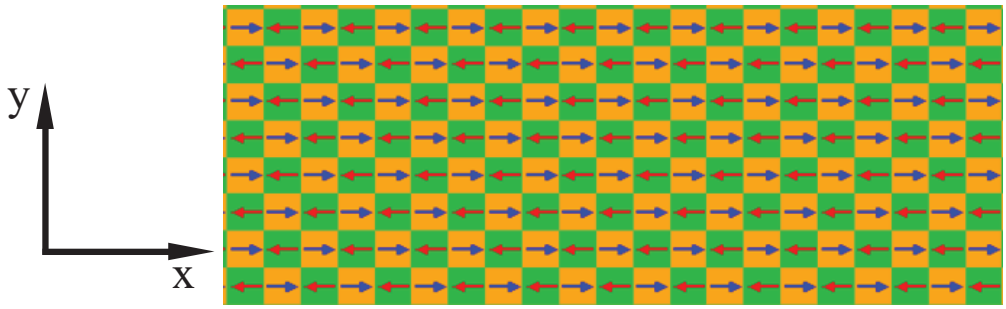

Figure 3.5: Snapshot of the magnetic ground state of the antiferromagnet after energy minimization with OOMMF. Each square represents a simulation cell of 1 nm×1 nm×1 nm and the uniaxial anisotropy is along the x-axis. Green and orange colors indicate cells of the two sublattices.

field is given by [34, 101]

$$\mathbf{H}_{ex,i} = \frac{2A_i^b}{M_s}\nabla^2\mathbf{m}_i - \frac{4A_{h,i}^b}{M_s}\mathbf{m}_i \times (\mathbf{m}_i \times \mathbf{m}_j) + \frac{2A_{nh,i}^b}{M_s}\nabla^2\mathbf{m}_j. \tag{3.6}$$

Here $i \neq j$, A_i^b, $A_{h,i}^b$ and $A_{nh,i}^b$ are intra-lattice, homogeneous and non-homogeneous exchange constants (b stands for Boris), respectively, for the two sublattice model implemented in Boris [101].

We calculate the spin wave dispersion of an AFM stripe with the dimensions mentioned above. We compare the results of the negative exchange approach in OOMMF with the results obtained with Boris for which the full two sublattice model with the equations 3.5 and 3.6 are implemented. In both cases, we use the cell size as mentioned earlier. We apply a sinc pulse in time and space with the cutoff frequency and wave vector of $f_c = 0.9$ THz and $k_{xc} = 0.2$ rad/nm, respectively, and amplitude of 100 mT. We perform the simulations for two cases of easy axis along the long side (x-axis) and along the short side (y-axis) of the stripe in xy-plane (Fig. 3.5). The spin wave dispersion of the continuum two sublattice model [with free energy Eq. A.80] obtained by fully solving the dynamic Eqs. A.2 and A.3 without damping is presented in [102] as

$$f(k) = \frac{\gamma}{2\pi}\sqrt{\left(2H_E + H_A - \frac{2A_{nh}}{M_s}k^2\right)\left(H_A + \frac{2A_{nh}}{M_s}k^2\right)}. \tag{3.7}$$

k is the SW wave vector. In the exchange limit, we obtain the following equation for the dispersion of spin waves

$$f(k) = \frac{\gamma}{2\pi}\sqrt{(2H_E + H_A)\left(H_A + \frac{2A_{nh}}{M_s}k^2\right)}. \tag{3.8}$$

In the above mentioned Eqs. 3.7 and 3.8, the exchange field is given by $H_E = 2A_h/M_s$. From the two sublattice model equations implemented in Boris [Eqs. 3.5 and 3.6], they obtain the following equation for the spin wave dispersion [101]

$$f(k) = \frac{\gamma}{2\pi}\sqrt{\left(2H_E + H_A - \frac{\left(2A^b + \left|A^b_{nh}\right|\right)}{M_s}k^2\right)\left(H_A + \frac{\left(2A^b + \left|A^b_{nh}\right|\right)}{M_s}k^2\right)}, \tag{3.9}$$

with $H_E = 4A^b_h/M_s$. Comparing the definition of the exchange field, H_E, between the continuum two sublattice model and the implementation in Boris, we obtain the relation between the homogeneous exchange coefficient in our continuum model and the one used in Boris as $A_h = -2A^b_h$. By comparing the magnon dispersion [Eqs. 3.7 and 3.9] we find that the non-homogeneous exchange constant in our continuum model is related to the one in Boris as $2A_{nh} = -A^b_{nh}$. An intra-sublattice exchange coefficient in our continuum model and Ref. [102] is not considered so $A^b = 0$. Therefore, our negative exchange model in OOMMF with $A_{ex} = -10$ pJ/m is equivalent to our two sublattice continuum model with $A_h = 40$ MJ/m^3 and $A_{nh} = 10$ pJ/m and a two sublattice model in Boris with $A^b_h = -20$ MJ/m^3, $A^b_{nh} = -20$ pJ/m and $A^b = 0$. The result of micromagnetic simulations for an anisotropy along the x-axis, which represents a wave vector k parallel to the anisotropy axis or Néel vector ($\mathbf{k}||\mathbf{n}$), is shown in Fig. 3.6. The result for an anisotropy along the y-axis ($\mathbf{k} \perp \mathbf{n}$) is shown in Fig. 3.7. The parameters mentioned above are used for simulations with OOMMF [Figs. 3.6(a) and 3.7(a)] and Boris [Figs. 3.6(b) and 3.7(b)]. The sublattice magnetization and anisotropy values are the same as those used later in chapter 6. The red dashed lines represents the Eq. 3.8, which is the spin wave dispersion obtained from our continuum model with the exchange limit approximation. From these simulations we prove that: i) a negative exchange model in OOMMF physically represents a two sublattice micromagnetic model as it was proven by the derivations in Appendix A.2 and the direct two sublattice model simulations, ii) our exchange limit approximation in chapter 6 is in very good agreement with both micromagnetic simulation results. The second conclusion is because in the exchange limit where the exchange interaction is very large, the contribution of k dependent term in the first bracket of Eqs. 3.7 and 3.9 is negligible compared to k dependent term in the second bracket.

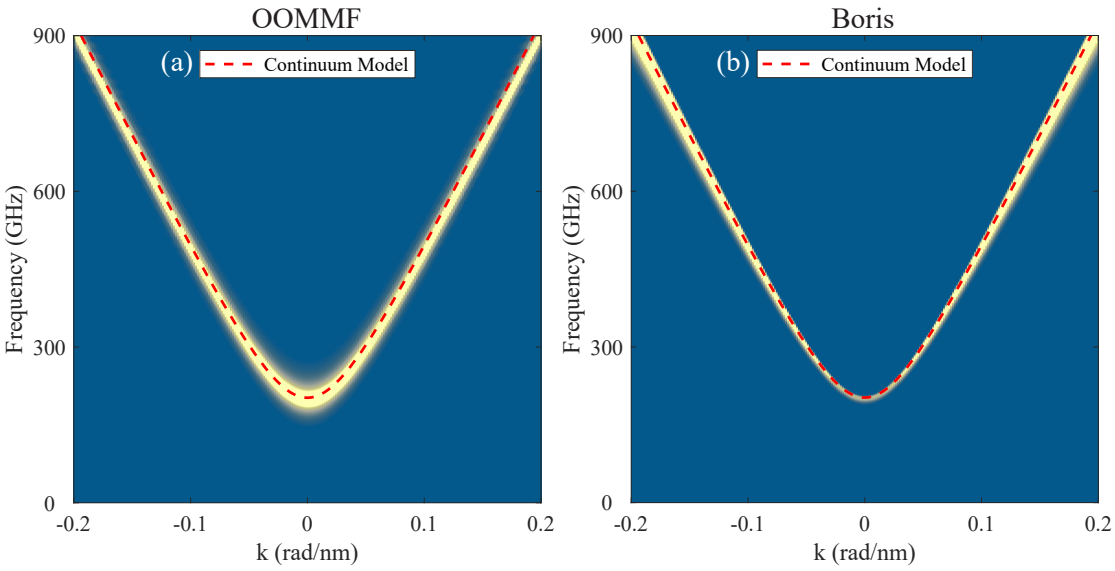

Figure 3.6: Spin wave dispersion for $\mathbf{k}||\mathbf{n}$ using OOMMF (a) and Boris (b). The red dashed line represents the spin wave dispersion obtained from the continuum model in the exchange limit.

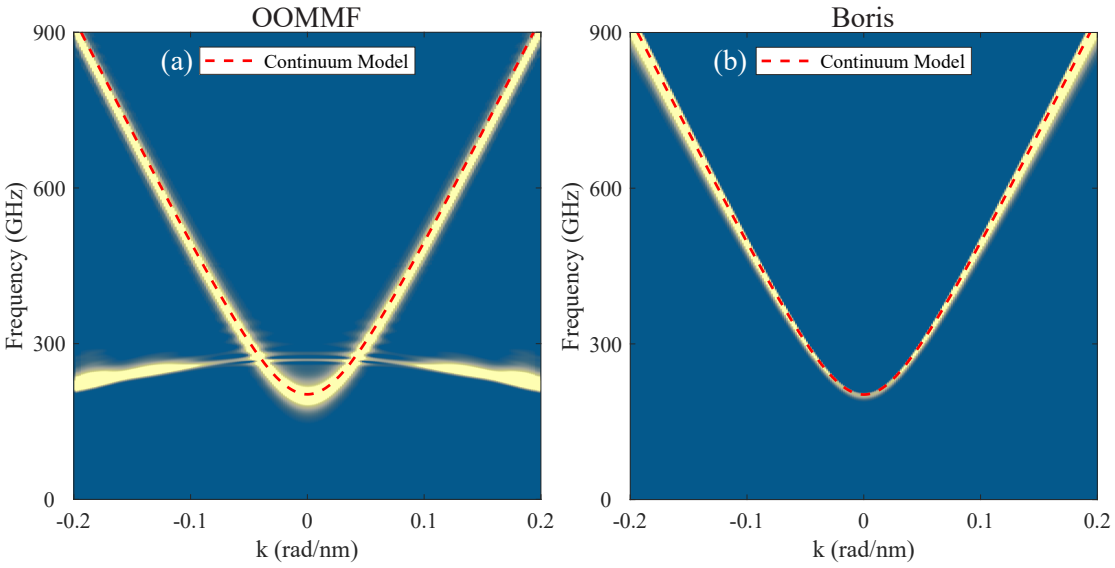

Figure 3.7: Spin wave dispersion for $\mathbf{k} \perp \mathbf{n}$ using OOMMF (a) and Boris (b). The red dashed line represents the spin wave dispersion obtained from the continuum model in the exchange limit.

3.4 Thin film growth

Of all the growth methods reviewed in Sec. 2.6 the available techniques at CMi were reactive rf sputtering from a Fe target as well as rf magnetron sputtering from a stoichiometric target. Most of the reviewed deposition methods involved substrate heating to temperatures ranging from 300 °C to 800 °C. The sputtering machine in CMi did not support any substrate heating and I was limited to room temperature deposition. Therefore, a post deposition annealing step was applied. I tried both reactive and stoichiometric depositions at room temperature and combined them with post annealing steps. In the begining I tried furnace annealing at 800-900 °C for 24 hours. The recipes resulted in epitaxial thin films evidenced by XRD measurements with thicknesses between 15nm and 200 nm with both deposition methods. However, the grown films did not show any magnon spectra in BLS measurements. Inspired by Ref. [73] suggesting successive ultra-thin film depositions combined with intermediate annealing and by Refs. [103, 104] I decided to use rapid thermal annealing instead of furnace annealing. Fixing the annealing temperature to 900°C, I tested different durations (2-5 min) and repetitions (1-4 times) of annealing step. Here, I report the most successful recipe in the following. I should note that all the annealing recipes resulted in epitaxial films evidenced by XRD. But only the films grown by the following recipe showed magnon spectra.
Smooth thin films of α-Fe_2O_3 with rms roughness of 0.2-0.4 nm have been sputtered on sapphire substrates (0.11 nm rms roughness). Samples are grown with different Ar/O2 partial pressure and sputtering rf power (in order to control the deposition rate) on a *c*-plane sapphire substrate at room temperature from a stoichiometric Fe_2O_3 target. The growth conditions are indicated in Table 3.1. Samples are grown in a layer-by-layer fashion in which we deposit 5 nm of Fe_2O_3 and for every layer it is annealed twice via a rapid thermal annealing (RTA) recipe. RTA recipe consists of two successive annealing steps of 5 minute long at 900 °C under the constant O_2 and N_2 flow of 1400 sccm and 600 sccm as shown in Fig. 3.8. The temperature ramp rate was 200 °C/s. We repeated this successive deposition and annealing steps for three times and obtained an epitaxial thin film of α-Fe_2O_3 with thickness of 15 nm. The XRD characterization and BLS measurements on these thin films will be presented in chapter 5.

Table 3.1: Sputtering condition for α-Fe_2O_3 thin film growth.

Sample Name	Atmosphere: Ar/O_2 (sccm)	Power (W)	Depisition Rate (Å/s)
SB1	30/15	200	0.112
SB2	30/15	150	0.075
SB3	10/20	200	0.1

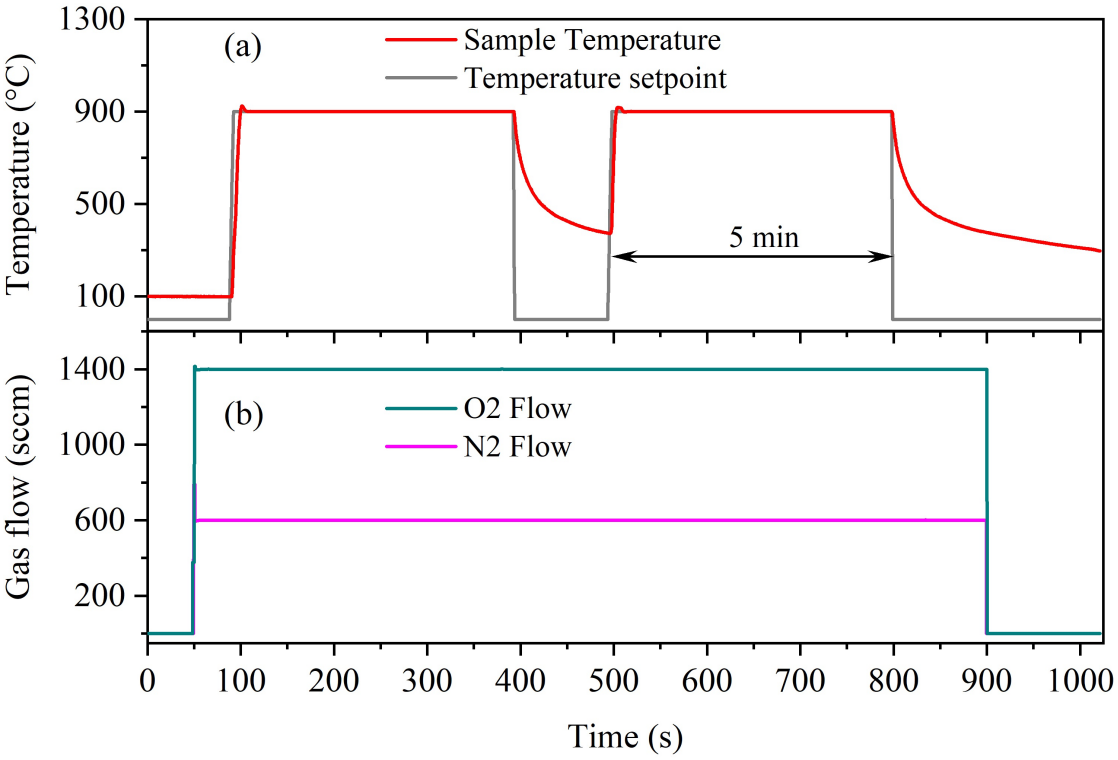

Figure 3.8: The rapid thermal annealing recipe used for epitaxial growth of α-Fe_2O_3 thin films originally deposited at room temperature. (a) The setpoint (gray) and actual sample temperature (red) profile during annealing. (b) Annealing atmosphere in the chamber consisting of O_2 (green) and N_2 (magenta) gas flow. Samples are annealed twice with this recipe after every 5 nm deposition of α-Fe_2O_3 at room temperature.

Results and Discussion Part II

4 Antiferromagnetic spin waves in bulk canted antiferromagnet Hematite α-Fe_2O_3

This chapter constitutes a substantial part of my thesis, namely the investigation of antiferromagnetic spin waves in bulk hematite crystal. In Sec. 4.1 we report on broad band microwave spectroscopy of quasi-ferromagnetic (qFM) mode at $k = 0$. From this we obtain material parameters including exchange, anisotropy and magnetoelastic fields as well as the damping. Then we report wave vector resolved BLS measurements from which we obtain the dispersion relation of the qFM mode. The VNA and BLS results combined indicate that qFM mode in hematite has extremely large group velocities and long decay length in the range of 23.3 km/s and 11 mm, respectively. All these measurements are performed at room temperature. Moving on we present cryogenic BLS measurements for the bulk crystal and a lamella prepared from the bulk sample in the temperatures below Morin temperature where hematite is in the uniaxial AFM state. Sub-THz spin waves with frequencies in the range of 60 to 200 GHz observed in the temperature range of 265 to 10 K.

4.1 Spin wave dispersion of ultra-low damping hematite (α-Fe_2O_3) at GHz frequencies

M. Hamdi, F. Posva and D. Grundler
arXiv 2212.11887 (2022)
doi: arXiv 2212.11887

My contribution to this paper included the broad band microwave spectroscopy and Macro-BLS measurements and data analysis. Preliminary broad band microwave spectroscopy measurements were conducted with the help of F. Posva. I wrote the draft of the manuscript.

Chapter 4. Antiferromagnetic spin waves in bulk canted antiferromagnet Hematite α-Fe_2O_3

Abstract

Low magnetic damping and high group velocity of spin waves (SWs) or magnons are two crucial parameters for functional magnonic devices. Magnonics research on signal processing and wave-based computation at GHz frequencies focussed on the artificial ferrimagnetic garnet $Y_3Fe_5O_{12}$ (YIG) so far. We report on spin-wave spectroscopy studies performed on the natural mineral hematite (α-Fe_2O_3) which is a canted antiferromagnet. By means of broadband GHz spectroscopy and inelastic light scattering, we determine a damping coefficient of 1.1×10^{-5} and magnon group velocities of a few 10 km/s, respectively, at room temperature. Covering a large regime of wave vectors up to $k \approx 24$ rad/μm, we find the exchange stiffness length to be relatively short and only about 1 Å. In a small magnetic field of 30 mT, the decay length of SWs is estimated to be 1.1 cm similar to the best YIG. Still, inelastic light scattering provides surprisingly broad and partly asymmetric resonance peaks. Their characteristic shape is induced by the large group velocities, low damping and distribution of incident angles inside the laser beam. Our results promote hematite as an alternative and sustainable basis for magnonic devices with fast speeds and low losses based on a stable natural mineral.

Main part

Introduction

Spin waves (magnons) are collective spin excitations in magnetically ordered materials. They exhibit promising functionalities for information transmission and processing at GHz frequencies [9, 12, 105]. To realize energy efficient magnonic circuits [9–12, 106] isotropic spin wave (SW) dispersion relations, high group velocities, and low magnetic damping are essential. Until today, the artificial garnet $Y_3Fe_5O_{12}$ (YIG) [107] played a key role for the exploration of magnonics functionalities [108]. Already in 1961, M. Sparks et al. coined the term that YIG was to ferromagnetic resonance research what the fruit fly was to genetics research [16]. This was particularly true for high-quality YIG grown by liquid phase epitaxy on the wafer scale [108, 109]. However, in a ferrimagnetic material like YIG, magnon bands in the regime of small wave vectors, k, and low GHz frequencies are inherently anisotropic due to the dipolar interaction between spins. To overcome this, a lot of effort has been put into the development of microwave-to-magnon transducers which allow for the excitation of exchange dominated SWs with isotropic properties at high frequencies [110–112]. The transducers suffer however from typically a narrow bandwidth or require an applied magnetic field in contrast to conventional transmission lines and coplanar waveguides (CPWs).

In antiferromagnetic (AFM) materials, exchange interaction dominates the dispersion relation already at small wave vectors k. The dipolar interactions are virtually absent due to net zero magnetization. Still, SWs can propagate with high group velocities. Values similar to thick YIG [108, 113] and as high as 30 km/s have been reported [114–117]. However, the challenge with most AFMs is their net zero magnetization and sub-THz frequencies which make on-chip integration hard due to lack of efficient CPWs and THz sources (THz gap) [7, 8]. Recently, the natural mineral and canted antiferromagnet hematite (α-Fe_2O_3) [48] gained particular atten-

tion for magnonics [118, 119] after the observation of long distance spin transport [120, 121] and enhanced spin pumping [122]. It is known that, due to extremely low anisotropy in the basal plane [47, 48, 123], in the canted phase [Fig. 4.1(a) and (b)] one branch of the magnon modes resides at around 10 GHz at small k. Depending on the purity of hematite crystals, a damping coefficient as low as 7.8×10^{-6} was reported for the magnetic resonance [124]. The hematite's finite net magnetization and strikingly small damping of below 10^{-5} make it hence suitable for magnonic applications. They allow for inductive coupling to CPWs and long-distance SW transport, respectively. However, there is no experiment reporting a measured SW dispersion for k values accessible by CPWs with integrated microwave-to-magnon transducers [110–112]. The dispersion measured over a large wave vector regime is of fundamental importance as it allows one to quantify the exchange stiffness length l_e with large precision. l_e is the key parameter to estimate the maximum possible spin-wave velocity of hematite in the GHz frequency regime.

Here, we study the magnon band structure of bulk hematite at different wave vectors k by means of broadband microwave spectroscopy and k-resolved inelastic Brillouin light scattering (BLS) (Fig. 4.1). All the measurements are performed on an a-pane natural crystal of hematite commercially bought from the company Surface Net. Using a CPW in flip-chip configuration we extract a magnetic damping parameter of 1.12×10^{-5} which is similar to the best YIG reported in Ref. [125]. Still, the measured spectra with BLS show broad linewidths. Our modelling substantiates that the linewidth is explained by the SW dispersion relation, the large SW velocity and the Gaussian profile of the laser used for inelastic light scattering. The data substantiate a high group velocity of 10 km/s for $k = 2.5$ rad/μm which are excited easily by a micron-sized CPW [119, 126]. In an applied field of 90 mT, the velocity increases to 16 km/s near $k = 5$ rad/μm and levels off to 23.3 km/s for $k \geq 25$ rad/μm. The latter value has routinely been realized by transducers. Our findings substantiate hematite as a very promising candidate for a sustainable future of magnonics as its growth avoids the lead-based synthesis route used for high-quality YIG [107, 125].

Properties of hematite

We first briefly review the relevant magnetic properties of α-Fe_2O_3. Hematite is the stable end product of oxidation of magnetite [127] and known for its great abundance as well as stability in an aqueous environment [128]. It is an insulating antiferromagnet (AFM) with a corundum crystal structure. The arrangement of the magnetic atoms of Fe in the crystal is shown in Fig. 4.1(a) [129]. At room temperature and above the Morin transition temperature of $T_M = 262$ K the Fe^{+3} magnetic moments lie in the c-plane due to an easy plane anisotropy, H_A, and stack antiferromagnetically along the c-axis [Fig. 4.1(a)] [47, 48]. Within the c-plane, there is a weak 6-fold anisotropy around the c-axis, H_a, which favors the magnetic moments to align with the a-axes [Fig. 4.1(b)]. The magnetic moments of the two AFM sublattices are slightly canted away from the a-axis by the Dzyaloshinskii-Moriya (DM) interaction (Fig. 4.1(b)), resulting in a weak magnetic moment, **m**, perpendicular to both a- and c- axes at equilibrium [47, 48]. The magnetization amounts to about 2 kA/m [127]. The domain nucleation and propagation

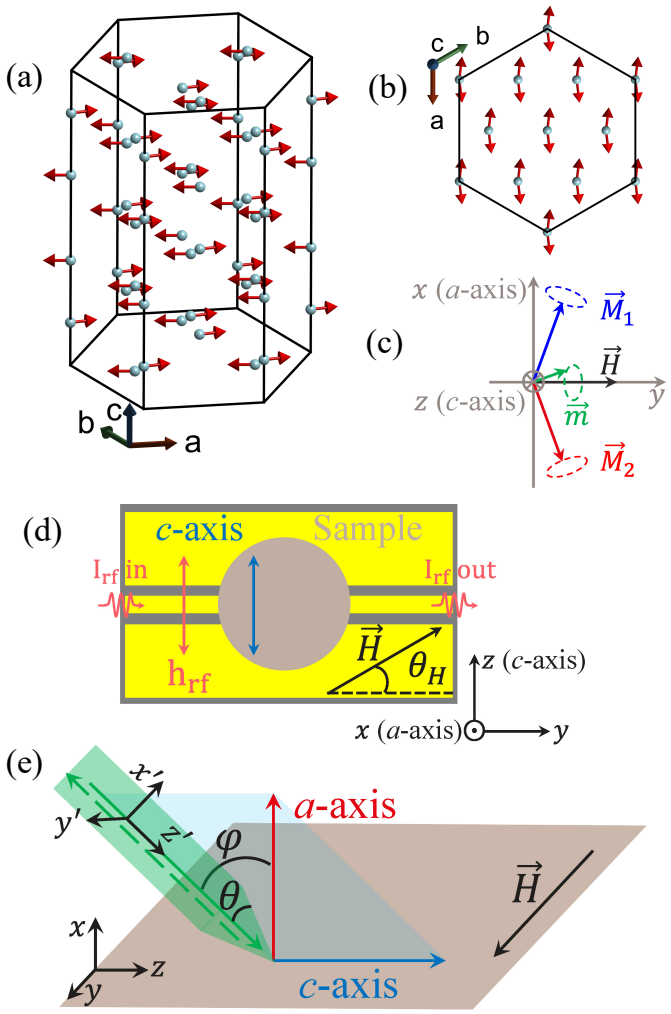

Figure 4.1: Hexagonal unit cell of the crystal structure of hematite from (a) the side and (b) top view. The cyan spheres and red arrows indicate the Fe atoms and the spins associated with them, respectively (oxygen atoms are not shown). We depict the canted antiferromagnetic state above the Morin temperature for which the sublattice spins lie in the c-plane along the a-axis with a small canting. They give rise to sublattice magnetization vectors $\mathbf{M}_1$ and $\mathbf{M}_2$. (c) Sketch of the low frequency quasi-ferromagnetic mode where a small magnetization (green arrow), $\mathbf{m}$, precesses elliptically around the applied field (black arrow), $\mathbf{H}$. (d) Schematics of the flip-chip VNA measurement. The sample (gray disk) is placed on a CPW. The static magnetic field, $\mathbf{H}$, is applied in the a-plane and with an angle, θ_H, to the normal of the c-axis of the crystal. The rf magnetic field (orange double-headed arrow), $\mathbf{h}_{\text{rf}}$, of the CPW is parallel to the c-axis. (e) Sketch of the BLS configuration. The magnetic field, $\mathbf{H}$, is applied perpendicular to c-axis in the a-plane. The laser light (green) forms a Gaussian beam and is focused on the surface of the sample (gray). The cone angle of the objective lens is θ. The incident laser light with an incidence angle, φ is scattered by magnons. We measure in back-scattering geometry (dashed green arrow).

in bulk hematite crystals are sluggish. Vigorous wall displacements only begin in earnest in negative fields, once a threshold field is exceeded. It is shown that for an applied field of ≈2.5 mT the domain structure was removed except in localized regions that are probably the sites of crystal defects [130–134]. The magnetization dynamics of hematite in this weak ferromagnetic state offers two modes namely the quasi-ferromagnetic mode (qFM or low frequency mode) and quasi-antiferromagnetic mode (qAFM or high frequency mode) [47, 48, 123].
The study of qAFM mode on our sample is reported in Ref. [135]. Here, we explore the qFM mode schematically depicted in Fig. 4.1 (c). The canted AFM sublattice magnetization vectors precess elliptically around their equilibrium direction. This results in an elliptical precession of the weak magnetic moment, **m** (green arrow in Fig. 4.1 (c)), around the applied field, **H** [47, 48, 123]. The frequency of the qFM mode was derived by Pincus [48, 123] according to

$$f_r = \frac{|\gamma|\,\mu_0}{2\pi}\sqrt{H\sin\xi(H\sin\xi + H_\mathrm{D}) + 2H_\mathrm{E}(H_\mathrm{a} + H_\mathrm{ME})}, \tag{4.1}$$

where, γ, μ_0, H_E, H_D and H_ME is the electron gyromagnetic ratio, vacuum permeability, exchange, DM and spontaneous magnetoelastic effective field, respectively. $\xi = \pi/2 - \theta_H$ is the polar angle between **H** and the c-axis (z-direction). We define θ_H in Fig. 4.1(d). Fink [136] derived the dynamic susceptibility $\chi_{zz}(f, f_r)$ for the qFM mode. The real and imaginary parts read

$$\mathrm{Re}\left[\chi_{zz}(f, f_r)\right] = \frac{\left(f_r^2 - f^2\right) f_r^2}{\left(f_r^2 - f^2\right)^2 + \Delta f^2 f^2} \text{ and} \tag{4.2}$$

$$\mathrm{Im}\left[\chi_{zz}(f, f_r)\right] = \frac{f f_r^2 \Delta f}{\left(f_r^2 - f^2\right)^2 + \Delta f^2 f^2}, \tag{4.3}$$

respectively. Here, f is the frequency of the radiofrequency (rf) magnetic field $\mathbf{h}_\mathrm{rf}$ (Fig. 4.1 (d)). The frequency linewidth, Δf, is related to the magnetic damping parameter, α, by

$$\Delta f \approx 2\alpha H_\mathrm{E}(\gamma/2\pi), \tag{4.4}$$

for $H \ll H_\mathrm{E}$. Unlike ferromagnets and uniaxial antiferromagnets, the resonance line width of a canted antiferromagnet does not depend on f_r and is governed by the field-independent exchange frequency. Following Turov [114, 115], the SW dispersion of the qFM mode for hematite near $k = 0$ is given by

$$f_m(k) = \frac{|\gamma|\,\mu_0}{2\pi}\sqrt{H(H + H_\mathrm{D}) + 2H_\mathrm{E}(H_\mathrm{a} + H_\mathrm{ME} + Ak^2)}, \tag{4.5}$$

where $A = H_\mathrm{E} l_\mathrm{e}^2$ is the dispersion coefficient and l_e is the effective magnetic lattice parameter or exchange stiffness length. For Eq. 4.5, we considered the experimental geometry for k-resolved BLS measurements with an angle $\xi = \pi/2$ as described below.

Experimental techniques

The broadband microwave spectroscopy was conducted at room temperature above T_M (Fig. 4.1(d)). The disk-shaped a-plane α-Fe_2O_3 crystal had a diameter of 2.3 mm and thickness of 0.5 mm. Measurements were done in flip-chip configuration for which the sample was placed on a CPW with signal (ground) line width of 165 μm (295 μm). The a-axis of the crystal was perpendicular to the disk plane. The c-axis was in the plane and perpendicular to the CPW axis. Injecting a radio-frequency (rf) current, $I_{\mathrm{rf}}^{\mathrm{in}}$, into the CPW by port 1 of a vector network analyzer (VNA) induced the dynamic magnetic field $\mathbf{h}_{\mathrm{rf}}$ (orange double-head arrow). The rf current was collected on the other end of the CPW by port 2 of the VNA ($I_{\mathrm{rf}}^{\mathrm{out}}$). The static magnetic field, $\mathbf{H}$, was applied in the a-plane of the crystal in all VNA measurements (yz-plane in Fig. 4.1 (d)). For the angle dependent measurements an external field of 90 mT was applied and the angle, θ_{H}, was varied in steps of $\Delta\theta_{\mathrm{H}} = 2°$. In case of field sweep measurements, the applied field angle was perpendicular to the c-axis and in the a-plane of the crystal ($\theta_H = 0$ deg). The field amplitude was varied in steps of $\Delta H = 0.5$ mT.

Wave vector-resolved BLS measurements were done for $\theta_H = 0$ deg on a piece of the same crystal in back-scattering geometry (Fig. 4.1 (e)) using a green laser with wavelength, $\lambda =$ 532 nm and wave vector $k_0 = 2\pi/\lambda = 11.81$ rad/μm. The external field was applied in the a-plane and perpendicular to c-axis. The sample for BLS was irregularly shaped. We ensured that it was tilted with respect to the incident laser beam along the y-axis in such a way that the laser beam remained in the xz-plane formed by the a- and c-axis. Since the penetration depth of the green laser in hematite is on the order of 75 nm [95], linear momentum conservation holds only for the in-plane component of the transferred wave vectors. Therefore, we define the transferred momentum from the light to magnons along the c-axis as $k_z = 2(k_0 \sin\varphi + k_x^{'} \cos\varphi)$, where φ is the angle between the incident beam and the normal to the plane of the sample (a-plane) [137]. We assume a Gaussian beam profile giving rise to a Fourier transform of the beam intensity I as

$$I(k_x^{'}) = e^{k_x^{'2} w_0^2/2}, \tag{4.6}$$

with $w_0 = \frac{2}{k_0 \mathrm{NA}}$. NA is the numerical aperture of the lens [138, 139]. The momentum $k_x^{'}$ has a projection on z-direction due to the focusing of the beam.

Broadband microwave spectroscopy data

Field-dependent VNA spectra are shown in Fig. 4.2 (a). We depict the imaginary part of the quantity $U(f,H) = i \ln\left[S_{21}(f,H)/S_{21}(f,H=0)\right]$ in a color-coded plot, where S_{21} is the complex scattering parameter measured by the VNA at a given field, H. We identify two branches which we label f_1 and f_2 for positive fields. For a detailed analysis, we consider that the parameter U contains the susceptibility χ of the sample [140, 141] and the electromagnetic response of the rf circuit used in the flip-chip method. To account for the different contributions, we

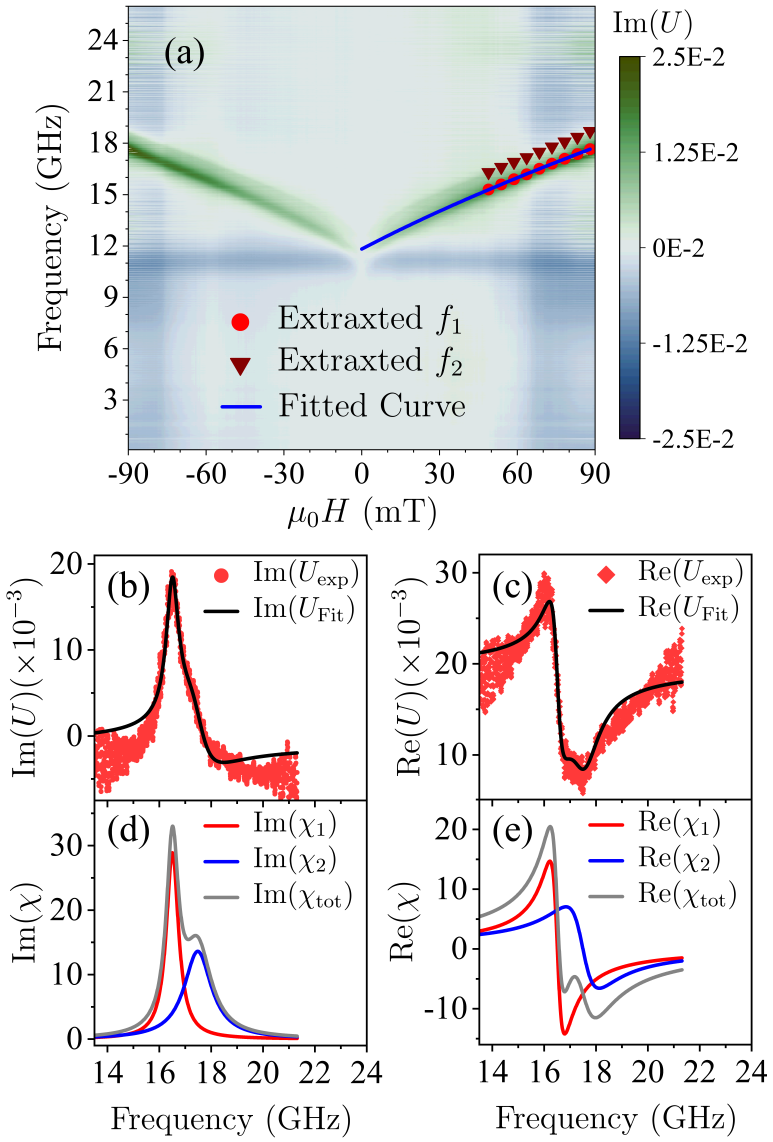

Figure 4.2: (a) Color-coded field dependent Im(U) parameter measured on the sample as indicated in Fig. 4.1(d) with $\theta_H = 0$ deg. Solid red circles and wine triangles are the frequencies extracted by fitting Eq. 4.7 on the data. Blue solid line is obtained by fitting Eq. 4.1 with extracted f_1 values. (b) Imaginary and (c) real part of U_{exp} (red symbols) and U_{fit} (black curves) for 70 mT, respectively. (d) Imaginary and (e) real parts of χ_1 (red curve), χ_2 (blue curve) and their sum (gray curve) for 70 mT, respectively.

follow Refs. [140, 141] and fit the measured U with

$$U_{fit} = C[1 + \chi_0 + \chi(f, f_1, \Delta f_1)e^{i\phi_1} + \chi(f, f_2, \Delta f_2)e^{i\phi_2}], \tag{4.7}$$

as shown in Fig. 4.2(b) and (c) (black lines). C is a real-numbered scaling parameter, χ_0 is a complex-numbered offset parameter, and ϕ_i are phase shift adjustments ($i = 1,2$). Using

Eq. 4.7, we extract the resonance frequencies and linewidths Δf_i for the two modes labelled by f_1 and f_2. In Fig. 4.2 (b) and (c), we display the measured imaginary and real parts of U with red symbols. In Fig. 4.2 (d) and (e), we show the extracted real and imaginary parts together with the total susceptibilities (gray lines) from which the two resonant modes are identified. Their frequencies extracted for different H are depicted in Fig. 4.2 (a) with solid red circles and magenta triangles. We focus on fields larger than 50 mT to ensure a saturated state.
The blue line in Fig. 4.2(a) results from fitting Eq. 4.1 to branch f_1 with $\xi = \pi/2$. From the fit, we obtain $\mu_0 H_E = 1003.61$ T, $\mu_0 H_D = 2.34$ T and $\mu_0(H_a + H_{ME}) = 88.64$ μT. Using Eq. 4.4 and the experimental value of $\Delta f_1 = 0.63$ GHz for branch f_1, we extract a damping parameter of $\alpha = 1.12 \times 10^{-5}$. This value is similar to the best value reported for YIG in Ref. [125]. The branch f_2 will be discussed later.
Angle-dependent VNA spectra are shown in Fig. 4.3. To enhance the signal to noise ratio, we

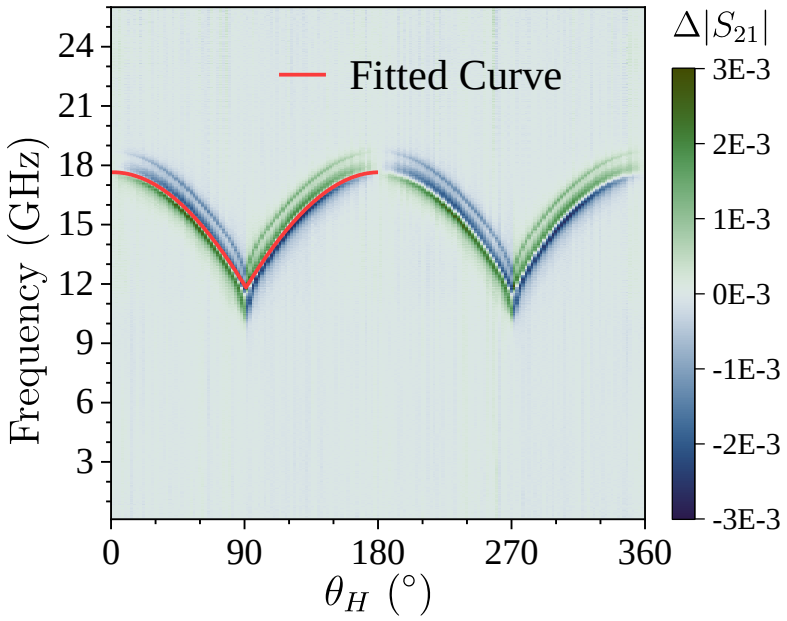

Figure 4.3: Color-coded neighbor subtracted angle dependent VNA-FMR spectra measured on the sample as indicated in Fig. 4.1(d) with $\mu_0 H = 90$ mT. Orange curve depicts Eq. 4.1 by extracted material parameters.

depict $\Delta|S_{12}| = |S_{12}(H + \Delta H) - S_{12}(H)|$. For such data, a zero-crossing (highlighted by the red curve) represents the resonance frequency. The spectra show a 2-fold symmetry as expected for the c-axis being in the plane of the applied magnetic fields. Introducing the extracted parameters discussed above, Eq. 4.1 models well the resonance frequency of branch f_1 as a function of angle θ_H (red line). The angular dependency is hence consistent with the effective anisotropy field extracted from the field-dependent data.

BLS data

The BLS spectra for different values of incident angle, φ, are shown in Fig. 4.4 (a). Black symbols in Fig. 4.4 (b) depict the frequency position of the maximum BLS peak as a function of wave vector calculated from the incidence angles shown in the legend of Fig. 4.4 (a). The red curve in Fig. 4.4 (b) is obtained by considering first the material parameters obtained from VNA measurements and then fitting Eq. 4.5 to the black symbols in the same graph. We obtain a dispersion coefficient of $\mu_0 A = 9.153 \times 10^{-6}$ T.μm^2 which leads to an exchange stiffness length of $l_e = 0.955$ Å. Using Eq. 4.5 and the obtained parameters we calculate the SW group velocity, v_g, for $\mu_0 H = 90$ mT [blue line in Fig. 4.4 (c)]. The velocity v_g increases significantly with k and levels off at 23.3 km/s. Such a high group velocity is the direct result of the strong exchange interaction and at the same time vanishingly small net magnetization. Microstructured CPWs used in magnonics offer spin-wave wave vectors around $k = 2.5$ rad/μm [119, 126]. For such a value k, the qFM spin wave in hematite exhibits a group velocity of $v_g = 10$ km/s similar to SWs in thick YIG and about a factor of 10 larger compared to ultra-thin YIG [142]. The decay length of the SWs is given by $l_d = v_g \tau$, where $\tau = (1/2\pi\alpha f_m(k))$ is the relaxation time of the SW. For 30 mT applied field and $k = 2.5$ rad/μm we calculate $v_g = 13.4$ km/s and $\tau = 840.6$ ns which leads to $l_d = 11.3$ mm, again similar to thick YIG. This is due to low damping and high group velocity of the qFM spin waves in hematite. Despite the small damping of the hematite sample measured by the VNA, the resonance peaks of the qFM mode in the BLS spectra show a large width of 10 to 20 GHz. Furthermore, the BLS peak taken at nearly normal incidence of the laser beam (e.g. at $\varphi = 0$ or 5 deg) shows a strong asymmetric shape. As φ increases, the intensity of the prominent peak reduces and it becomes more and more symmetric. To understand these observations, we calculated the partial density of states (pDOS) by considering the magnon dispersion relation and the Gaussian beam profile according to

$$pDOS(f,\varphi) = -\frac{1}{\pi}\int_{-\infty}^{+\infty} dk_x^{'} \cos\varphi \,\mathrm{Im}\left[\frac{I(k_x^{'})}{f - f_m(k) + i\Delta f}\right]. \tag{4.8}$$

Assuming only fully back reflected light we have $k = 2(k_0 \sin\varphi + k_x^{'}\cos\varphi)$. Δf is the resonance broadening due to the damping given by Eq. 4.4. The numerical aperture of the objective lens was $NA = 0.18$. The calculated pDOS for different incident angles is plotted in Fig. 4.4 (d). Comparing Figs. 4.4(a) and (c), the experimental BLS peaks are broad because they contain a certain frequency regime of the band structure which is determined by the Gaussian wave vector distribution of $k = 2k_0 \sin\varphi + \Delta k$. The central wave vector is $k_c = 2k_0 \sin\varphi$ and the distribution function for $\Delta k = 2k_x^{'}\cos\varphi$ is given by $I(k_x^{'})$ (Eq. 4.6). We attribute the broad BLS peaks hence to the high group velocity of magnons which leads to a peak width proportional to $v_g \times \Delta k$. The asymmetry of BLS peaks for small φ can be understood in terms of the Van Hove singularity of the pDOS near $k = 0$. As φ increases, the part of the band structure which is relevant for the collected light shifts away from $k = 0$. Consequently, the peak gets more symmetric with φ. The peak intensity reduces with φ due to the factor $\cos\varphi$ in Eq. 4.8. We note that Eq. 4.8 does not include all possible scattering processes. Still it provides a good qualitative understanding about the contributions giving rise to the characteristics shape and

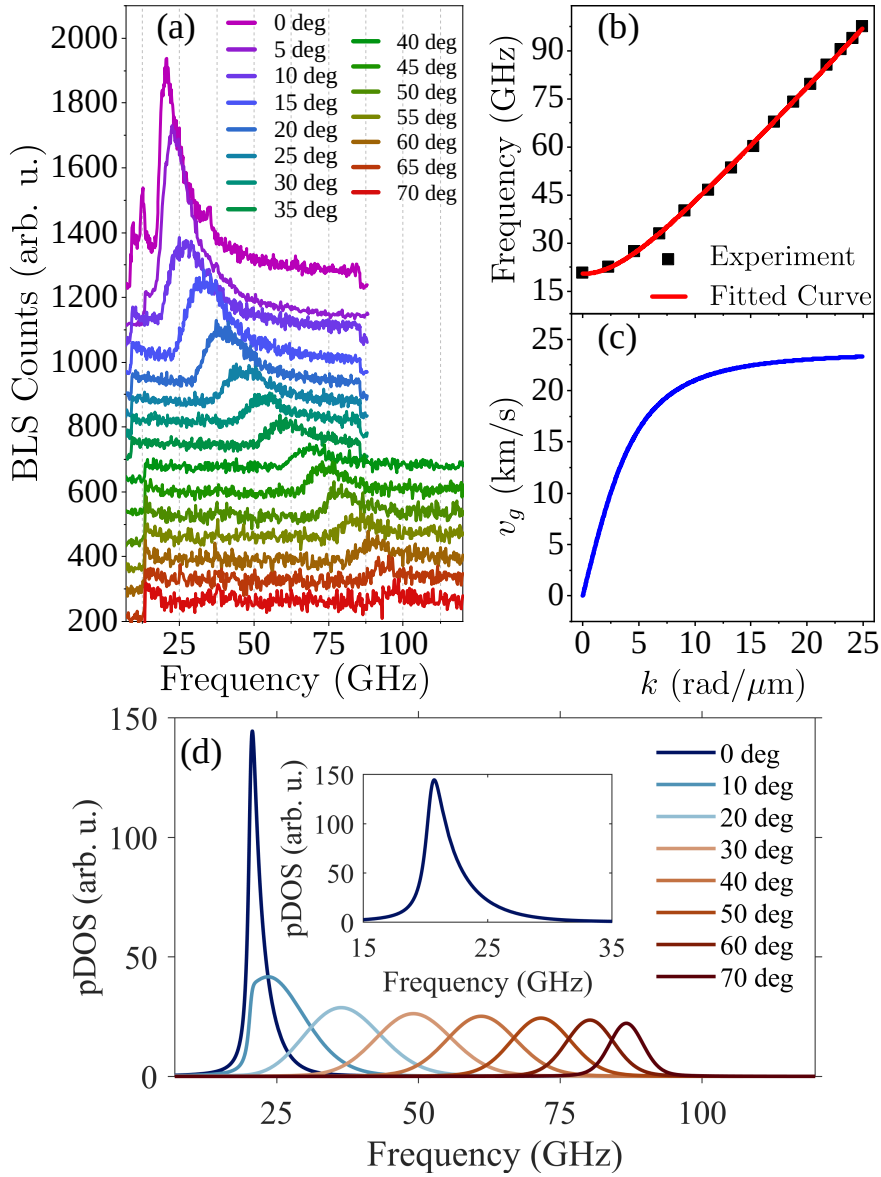

Figure 4.4: (a) BLS spectra for different incident angles, φ, measured as indicated in Fig. 4.1(e) with $\mu_0 H = 90$ mT. (b) Extracted peak maxima frequency (black squares) as a function of corresponding transferred wave vector, k and fitted dispersion relation (red curve) by Eq. 4.5. (c) Group velocity (d) partial density of states and obtained from fitted magnon dispersion at $\mu_0 H = 90$ mT. Inset in (d) depicts pDOS for $\varphi = 0$ degree.

signal strength of BLS peaks as a function of φ.

Discussion

The branch of mode f_2 in Fig. 4.2(a) is higher by about $\delta f = 1$ GHz than f_1 at the same field H. A second branch was reported also in Ref. [135]. Here the authors studied the qAFM mode at zero field and assumed a distribution of magnetic domains. We applied a large enough magnetic field to avoid domains. A domain formation can not explain our second branch. Another possibility for f_2 is a standing wave along the thickness of the sample or a SW excited with a discrete wave vector coming from the CPW. However, for these cases a quantitative estimate based on the magnon dispersion obtained with BLS (Eq. 4.5) led to a frequency separation of much smaller than 1 GHz.
The remaining explanation for f_2 is a nonuniform magnetoelastic field in the sample induced when fixing the sample on the CPW. We attribute the observed frequency splitting to different strains in different parts of the sample that is either in contact with the CPW conductors or floating on the CPW gaps. A difference of $\delta H_{\mathrm{ME}} = 24\ \mu$T would account for $\delta f = f_2 - f_1 = 1$ GHz. The effect of magnetoelastic interaction by unidirectional compression, $\mathbf{p}$, in the basal plane of the crystal, on the qFM mode is given by replacing H_{ME} with $H'_{\mathrm{ME}} = H_{\mathrm{ME}} - Rp\cos 2\psi$ [143, 144]. Here, $R = 287\ \mu$T/bar [144] is a coefficient determined by the elastic and magnetoelastic parameters of the crystal and $\psi = \pi/2$ is the angle between $\mathbf{p}$ and $\mathbf{H}$. Using $\delta H_{\mathrm{ME}} = Rp$ we obtain $p = 0.084$ bar. This value corresponds to a force of 14.6 mN on the parts of the crystal that are in contact with the CPW conductors. The evaluated force is one order of magnitude smaller than the weight of our sample and indicates the known sensitivity of hematite towards magnetoelastic effects.
From our experiments, we do not determine H_{a} and H_{ME} separately as they enter Eq. 4.1 in the same way. To separate the small H_{a} from H_{ME} an angle dependent VNA measurement with the magnetic field applied in the c-plane of the crystal would be required. The existing sample was not suitable for that.
Our BLS data were acquired on a seven times larger wave vector regime compared to the data used in Ref. [119] where, the authors extracted an exchange stiffness length l_{e} of 1.2 Å. From our extended dataset, we evaluate the value $l_{\mathrm{e}} = 0.96$ Å. The precise determination of l_{e} is of key importance as it determines the SW group velocity. Contrary to the ferrimagnetic YIG, dipolar effects are not expected to play an important role in SW dispersion of hematite. Hence, hematite thin films can provide similarly large spin-wave velocities as reported here for the bulk crystal. As a consequence, they potentially outperform YIG thin films concerning speed and decay lengths at wave vectors which are realized by the state-of-the-art transducers. Furthermore, hematite is based on earth abundant elements and as an end product of oxidation of magnetite a stable natural mineral suggesting sustainable synthesis routes.

Conclusion

We have measured the magnon dispersion relation of hematite for wave vectors k which are relevant for timely experiments in magnonics. The damping coefficient of the studied natural crystal was 1.1×10^{-5} at room temperature. This value is only 40 % larger than the best value

reported for pure hematite and is already as good as the best YIG. The estimated spin-wave decay length for k = 2.5 rad/μm is larger than 1 cm in a small magnetic field. In optimized thin films, current microwave-to-magnon transducers are expected to achieve larger group velocities in hematite than in YIG. The reported properties suggest that hematite can become the fruit fly of sustainable modern magnonics.

Note added

While completing the manuscript about our experiments on hematite [118], we became aware of Ref. [119]. The authors measured group velocities and the spin-wave dispersion via integrated CPWs for 1 rad/μm $\leq k \leq$ 3.5 rad/μm. Our BLS measurements cover a seven times larger regime of k values enabling an improved evaluation of the parameter l_e. This parameter is decisive to estimate the saturation velocity of GHz SWs in hematite.

The scientific colour maps developed by Crameri et. al. [145] is used in this study to prevent visual distortion of the data and exclusion of readers with colour-vision deficiencies [146].

Acknowledgement

The authors thank SNSF for financial support via grant 177550. We acknowledge discussions with A. Mucchietto, M. Mruczkiewicz, S. Nikitov and A. Sadovnikov. The different pieces of the hematite crystal were provided by J.-P. Ansermet and M. Bialek. We thank them for the support and discussions.

4.2 Sub-terahertz spin waves in bulk and micron sized lamella of hematite below Morin temperature

Characterization of (sub-)THz SWs in AFMs is an essential primary step in designing AFM-SHNOs. Due to THz gap indicated above, such characterizations is so far mostly done with an optical pump-probe method. Recently an all-electrical method based on solid-state frequency extenders is developed. However, it is difficult to characterize integrated on-chip magnonic devices like SHNOs by such methods. The inelastic Brillouin light scattering (BLS) is widely used to study FM-SHNOs in the GHz range due to its spatial resolution of few 100 nm. There are very few BLS studies in (sub-)THz frequency range. Here, we study the sub-THz spin waves of bulk hematite (α-Fe_2O_3) below its Morin temperature.

We investigated the magnons in bulk hematite ($\alpha-Fe_2O_3$) in AFS below the Morin temperature. The results of temperature dependent BLS measurements on the (11-20) surface of the crystal (a-plane) using the green laser is shown in Fig. 4.5(a). We observe at least three peaks in the spectra (marked by a black diamond, blue triangle and red aster). The temperature dependencies of the peaks are depicted in Fig. 4.5(b). The first peak (black diamond) at ≈60 GHz does not change much with temperature and indicates a phonon mode or a laser side peak. The second (blue triangle) and third (red aster) peaks evolve with temperature and indicate the magnon modes below a Morin temperature of T_M = 260 K which is in agreement with the reports in literature [147, 148]. After these measurements on the bulk sample we fabricated a lamella with lateral dimensions of ≈24×11 μm^2 with a thickness of ≈4 μm using a Ga focused ion beam (FIB). After performing temperature dependent BLS measurements on this lamella we thinned it down to ≈800 nm and measured again. An scanning electron microscopy (SEM) image of the transferred lamella on a substrate is shown in Fig. 6.3(c). The temperature dependent BLS data (Fig. 6.3(d)) shows that the Morin temperature is decreased to ≈245 K in the ≈4 μm lamella. Comparing the observed magnon spectra for bulk crystal, 4 μm and 800 nm thick lamellas indicated that by moving from bulk to 4 μm lamella, magnon frequencies reduce. However similar reduction is not observed for further thinning the lamella to 800 nm. We attribute these reductions in Morin transition and magnon frequency to possible Ga doping in the surface of the lamella while using Ga-FIB to prepare the lamella which is consistent with previous studies [148].

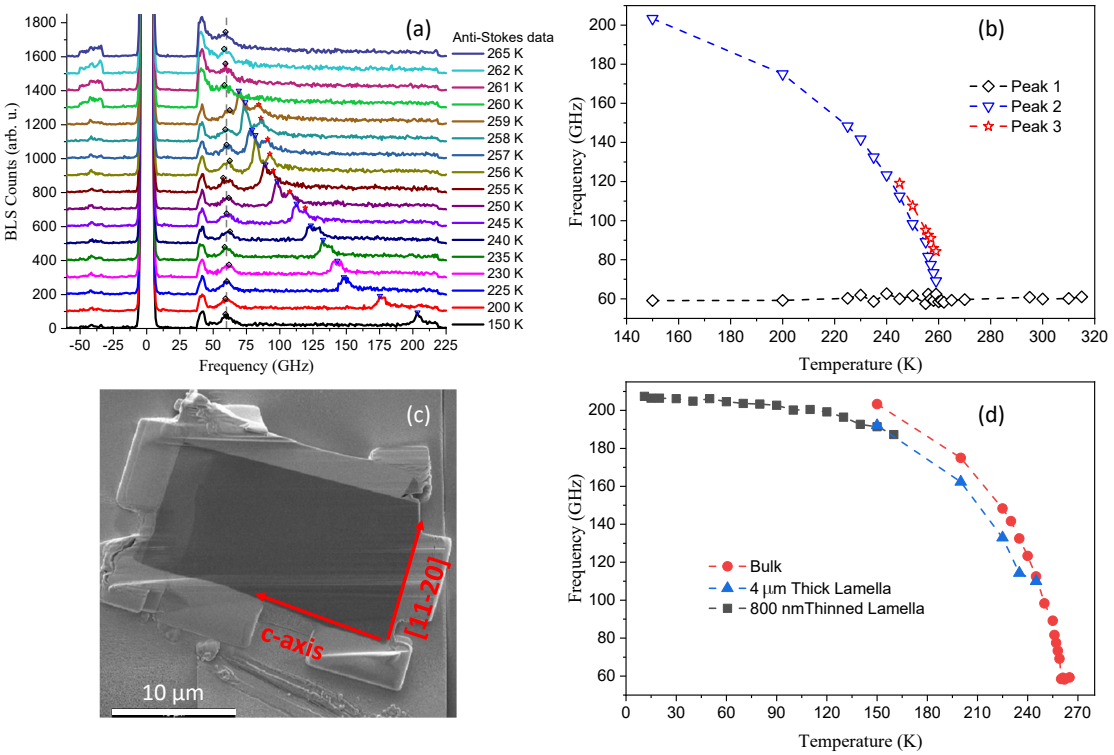

Figure 4.5: (a) μBLS spectra taken at different temperatures (indicated on the right) (b) temperature dependent peak positions extracted from of TD-μBLS performed on bulk hematite $\alpha - Fe_2O_3$(11-20). (c) SEM image of a 800 nm thick hematite $\alpha - Fe_2O_3$(11-20) lamella, and (d) comparison of temperature dependent peak positions of TD-μBLS for bulk, 4 μm and 800 nm thick lamellas. The high frequency mode above Morin transition was not observed in BLS spectra.

5 Antiferromagnetic spin waves in thin film canted antiferromagnet Hematite α-Fe_2O_3

High quality epitaxial thin films of hematite are required to realize GHz and THz applications mentioned in Sec. 1.1 and 1.2. Here, we report the High-resolution X-ray diffraction (HR-XRD) characterization of epitaxial α-Fe_2O_3 thin films grown as described in Sec. 3.4. The XRD results in Sec. 5.1 indicate the full epitaxial growth of thin films. Reciprocal lattice maps indicate that the growth is pseudomorphic and strained. We report the measurements on GHz SWs in our grown thin films in Sec. 5.2. The results indicate that despite epitaxial growth of the films, the ideal SW properties were not achieved since there is finite mosaicity in the films. This indicate the significant material science challenges in the path to realize AFM magnonic devices which needs to be addressed by the community.

5.1 Thin film growth and characterization

Al_2O_3 has the corundum structure, and the lattice parameters are $a = b = 4.76$ Å and $c = 12.99$ Å , and $\gamma = 120°$. The lattice mismatch between a-Fe2O3 and Al2O3 is about 5.8% and applies compressive strain to the film layers. The out of plane ($\theta - 2\theta$) XRD profile is shown in Fig. 5.1 for three samples SB1, SB2 and SB3. (0006) reflections of α-Fe_2O_3 is observed at $2\theta = 39.5°$ for all grown films. This is $\delta 2\theta = 0.25°$ larger that the bulk value $2\theta_0 = 39.25°$ which leads to a compressive strain of 0.65% along c-axis of the hematite thin film. Figure 5.2 shows the ϕ-scan profiles for the (104) reflection for the α-Fe_2O_3 thin film (sample SB3 as an example) and Al_2O_3 substrate in red and blue, respectively. For all films investigated here, (104) reflection peaks are seen every 120° in ϕ and their positions are identical to those for the (104) Al_2O_3 reflection of the substrates. These observations ensure that our α-Fe_2O_3 films are fully epitaxial single domain without crystallographic twin formation.

We also carried out reciprocal space mapping (RSM) measurements around the (104) reflection of Al_2O_3 shown in Fig. 5.3. As the peaks corresponding to substrate and the film lie on the same vertical line, it indicates a pseudomorphic growth i.e. the film takes the in-plane lattice constant of the substrate. This means that the grown thin films are fully strained. Therefore, there is a compressive strain of 5.8% in the in-plain direction. The spreading of the peaks

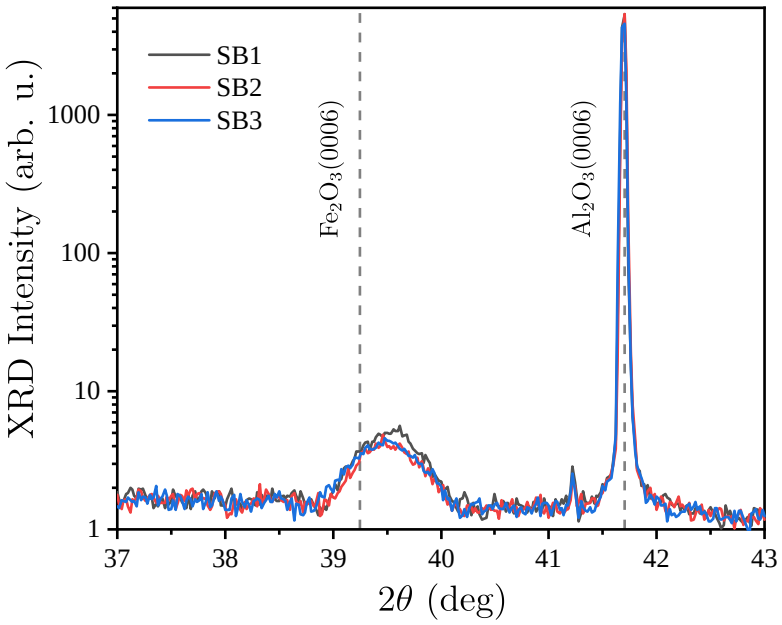

Figure 5.1: $\theta - 2\theta$ XRD profile of the grown thin films.

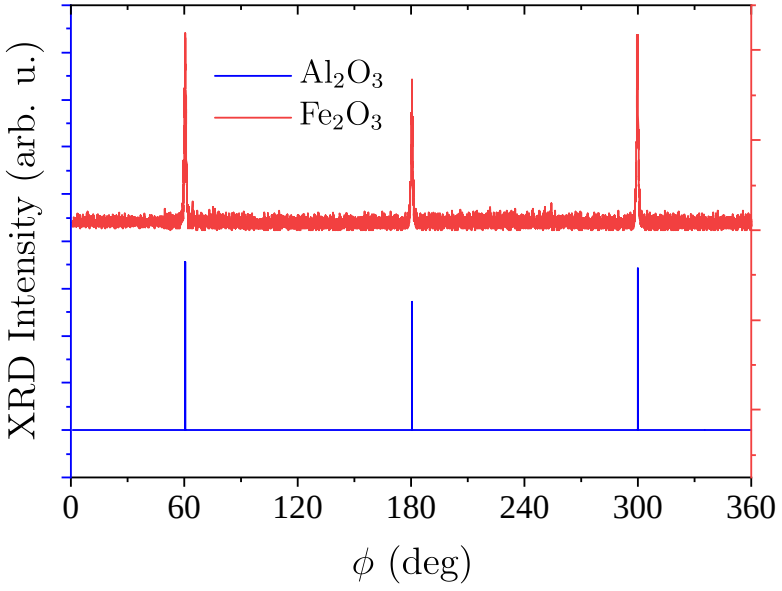

Figure 5.2: ϕ-scan profiles for the (104) reflection of α-Fe_2O_3 thin films (red) and Al_2O_3 substrate (blue) for sample SB3 as an example.

in horizontal direction extracted from RSM data (Fig. 5.4) indicates the mosaicity. The data indicates that the sample SB1 (SB3) has the lowest (highest) SB3 mosaicity among the three samples.

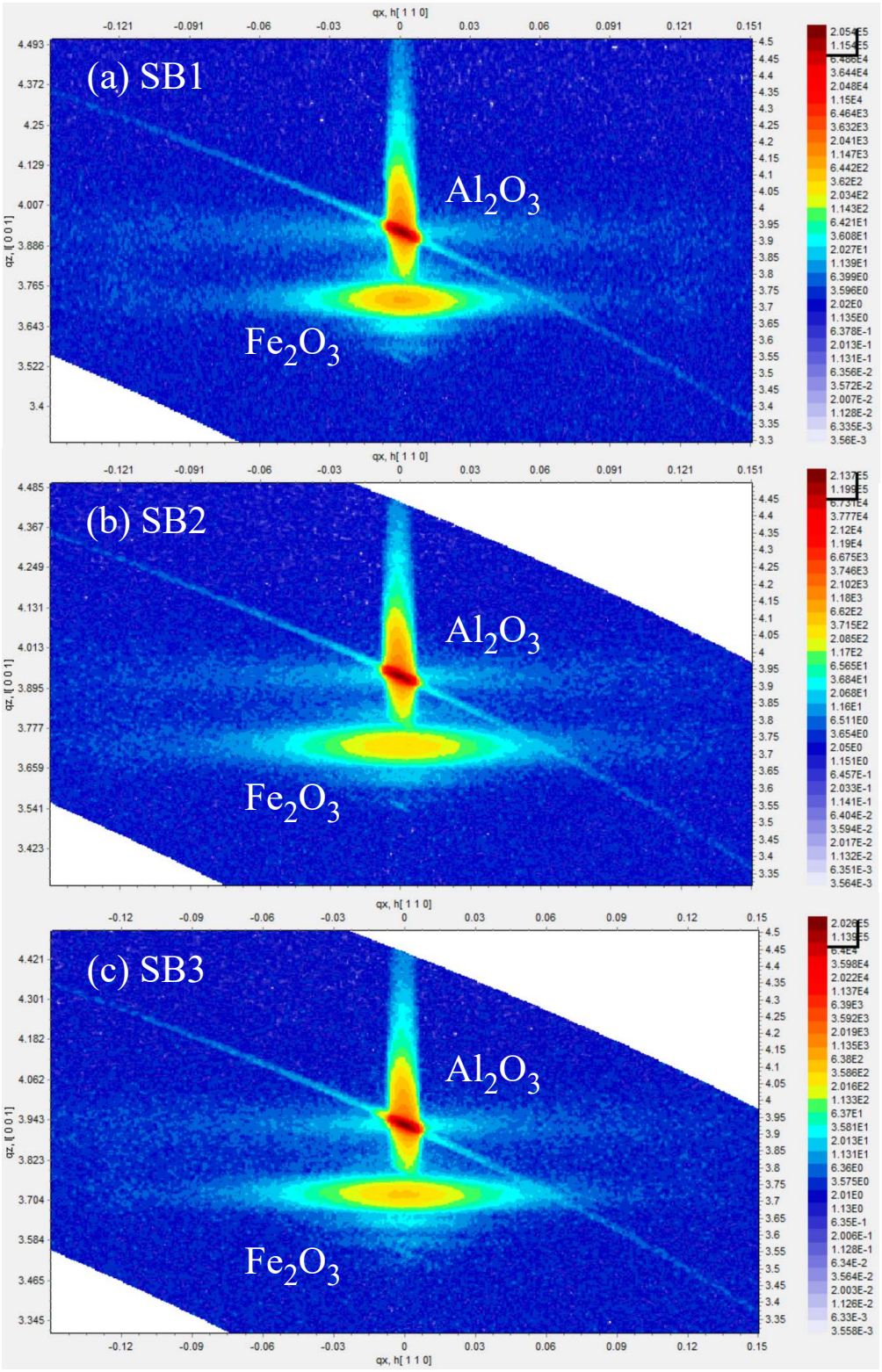

Figure 5.3: Reciprocal space mapping for the (104) reflection of Al_2O_3 for sample (a) SB1, (b) SB2 and (c) SB3. Legends represent XRD intensity.

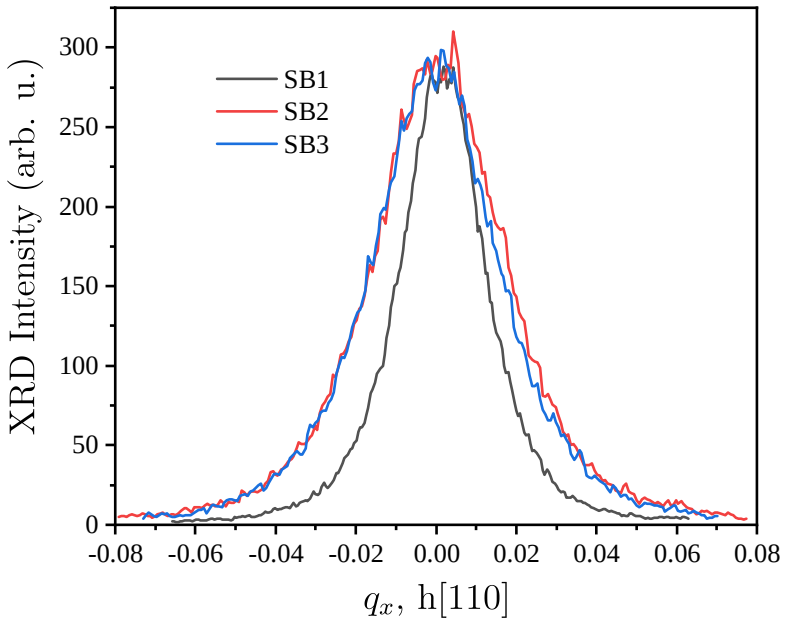

Figure 5.4: Line plot of the RSM spreading for the (104) reflection of α-Fe_2O_3 thin films.

5.2 Brillouin light scattering spectroscopy of thin film hematite α-Fe_2O_3

The BLS spectra measured at room temperature on qFM mode on samples SB1, SB2 and SB3 are shown in Figs. 5.5 , 5.6 and 5.7 respectively. Panels (a) and (b) in these figures show the BLS spectra obtained on two different spots with lateral separation of 5 μm. In all samples the spectra obtained on two separate spots differ greatly indicating magnetic non-uniformity. In each spot, multiple SW modes are observed. The frequencies of these modes do not strictly follow the field dependent behavior measured in the bulk sample reported in Sec. 4.1. The frequencies of the prominent peaks in Figs. 5.5(a), 5.6(b) and 5.7(b) are depicted in Fig. 5.8. The qFMR mode given by Pincus' Eq. 4.1 is plotted for comparison. The effective field values obtained in Sec. 4.1 are used for estimating the bulk mode. The modes observed in our thin films often show sudden jumps in the low field regime (12-40 mT). Figure 5.5(a) contains spectra closest to the bulk sample in terms of the observed frequency range.
In Ref. [79] the authors report what they call "substrate clamping" in which, the film experiences strain due to clamping on the substrate at the substrate-film interface. This cause the magnetic anisotropy not to follow the crystal symmetry of α-Fe_2O_3, but fluctuate. This leads to an overall isotropic distribution of the Néel order vector with locally varying effective anisotropy in α-Fe_2O_3 thin film. Such description can also explain our BLS observation. As it is clear from the XRD results discussed in Sec. 5.1, our films are under a great compressive strain in the *c*-plane due to lattice mismatch. Furthermore, there is a certain mosaicity in the grown films, which is created by slight misorientations of different crystals as they nucleate and grow on the substrate. When the crystals join to form the film, they form low energy boundaries. This would cause a certain spatially non-uniform strain in the film as reported in Ref. [79]. As it was discussed in Sec. 4.1, the magneto-elastic effects are very strong in hematite [143, 144]. Therefore, the internal magnetoelastic anisotropy will be affected by the in-plain compressive strain and mosaicity pattern and have a non-uniform spatial distribution. This spatially non-uniform anisotropy in turn would result in different magnetic resonance frequency as in is observed by BLS measurements.

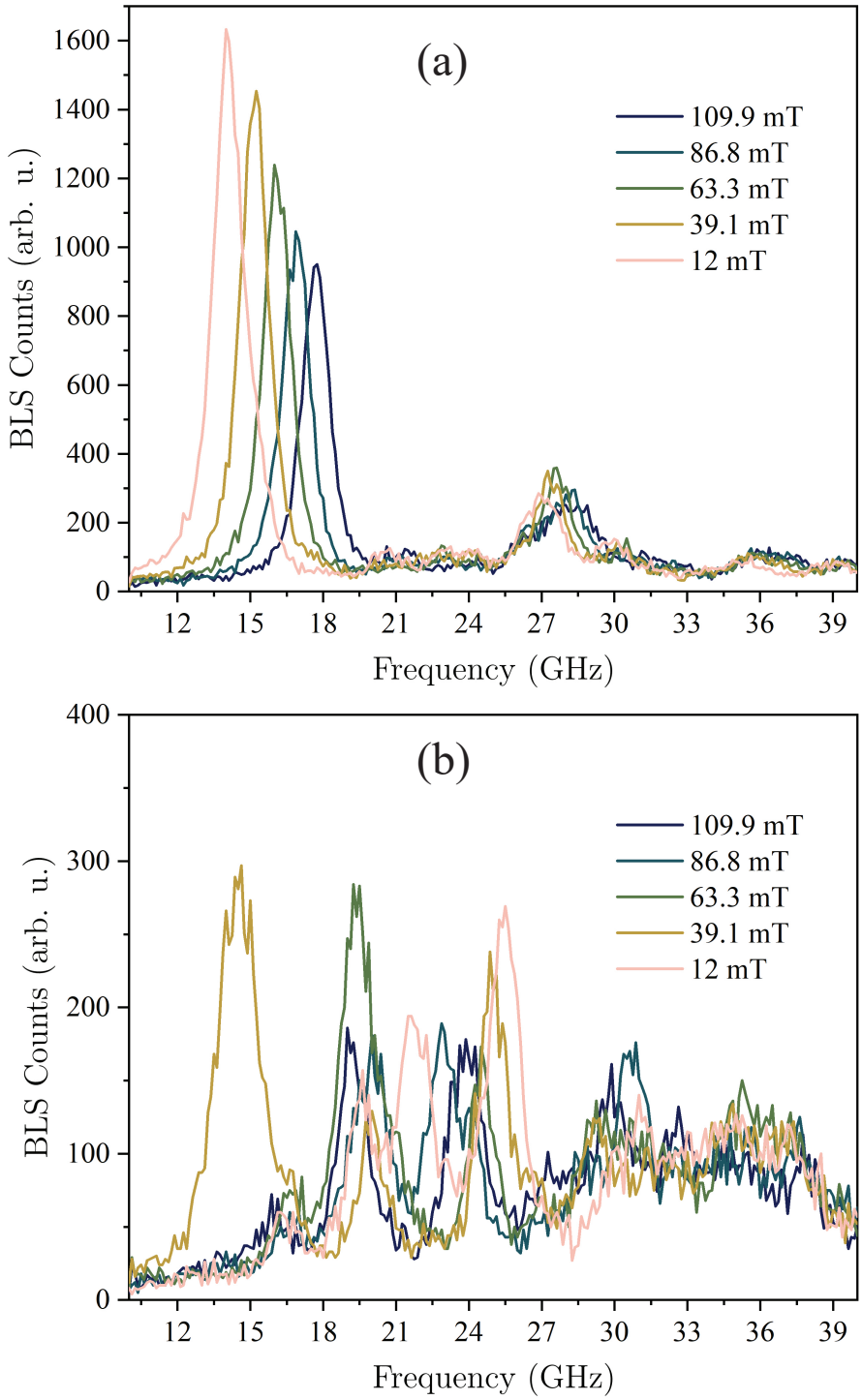

Figure 5.5: BLS spectra measured on 15 nm α-Fe_2O_3 (sample SB1) on two different spot separated by 5 μm.

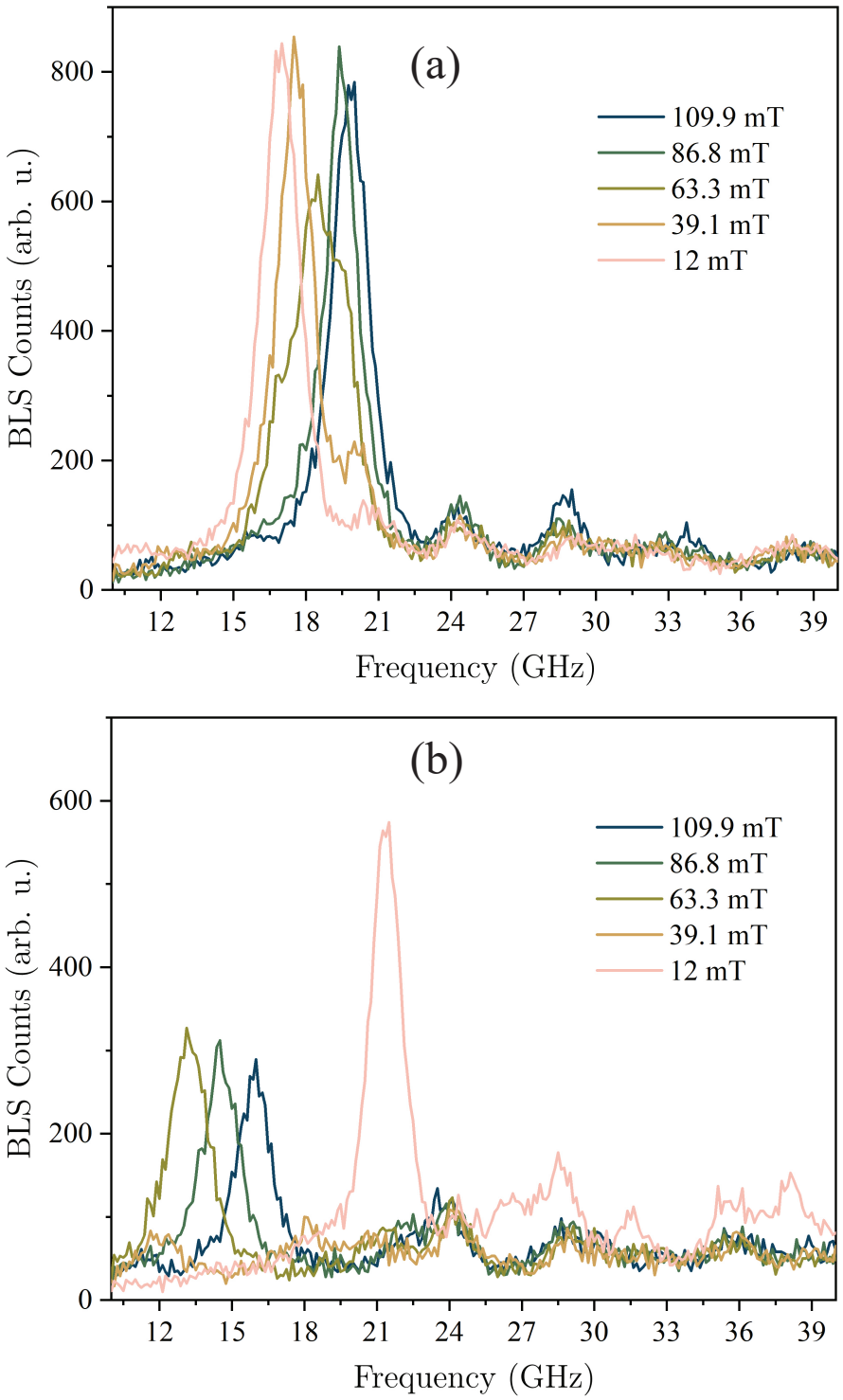

Figure 5.6: BLS spectra measured on 15 nm α-Fe_2O_3 (sample SB2) on two different spot separated by 5 μm.

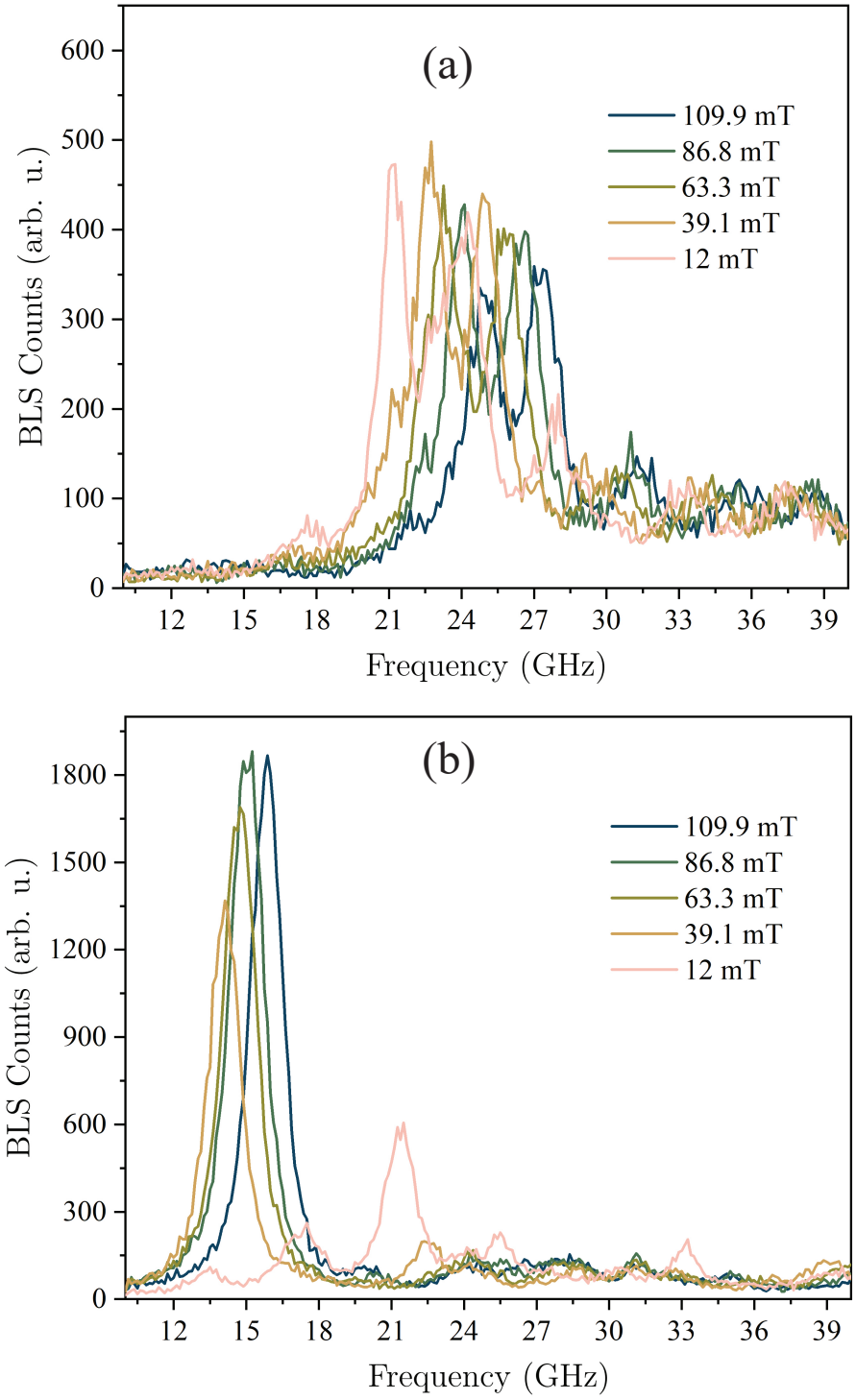

Figure 5.7: BLS spectra measured on 15 nm α-Fe_2O_3 (sample SB3) on two different spot separated by 5 μm.

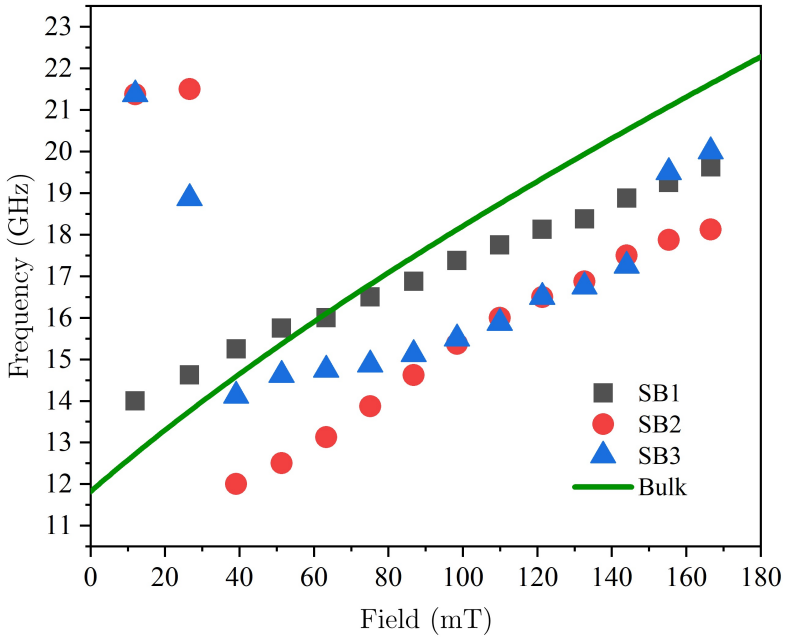

Figure 5.8: BLS peak positions (resonance frequencies) of the prominent peaks extracted from Fig 5.5(a) (black squares), Fig. 5.6(b) (red circles) and Fig. 5.7(b) (blue triangles) for samples SB1, SB2 and SB3, respectively. The green curve is the Pincus' equation 4.1 with effective field values extracted from the bulk sample in Sec. 4.1.

To furthere elaborate, in the following we recall some aspects of magnetoelastic effects in bulk hematite from Refs. [144, 149]. Considering the two sublattice model reviewed in Sec. 2.2 and the fact that our thin films are in the weak ferromagnetic state (WFS), we suppose the sublattice magnetizations $\boldsymbol{M}_1$ and $\boldsymbol{M}_2$ in the xy-plane (c-plane of the crystal) are given by the azimuthal angles ϕ_1 and ϕ_2, respectively (Fig. 5.9), from the applied field direction along x-axis. The direction of total magnetization vector, $\boldsymbol{M} = \boldsymbol{M}_1 + \boldsymbol{M}_2$ can be determined by the angle $\phi = (\phi_1 + \phi_2)/2$ and its length can be defined with angle $\psi = (\phi_1 - \phi_2)/2$ as $|\boldsymbol{M}| = 2M_0 \cos\psi$ with $M_0 = |\boldsymbol{M}_1| = |\boldsymbol{M}_2|$. We assume that a magnetic field $\mathbf{H}$ and an external stress $\sigma_{xx} = -p$ are applied along the x-direction. This direction can be chosen arbitrarily in basal plane as we neglect the 6-fold crystalline anisotropy in the basal plane for the sake of simplicity. The mechanical stress is compressive when $p > 0$ and tensile when $p < 0$. The pressure-associated effective field is given by $H_p = Rp$ as discussed in Sec. 4.1. It is instructive to define another effective field as $H_p^* = \frac{H(H+H_D)}{2H_E}$, which reflects the strength of the external field.
It can be shown that there are two equilibrium cases depending on the strength H_p and H_p^* as follows. (1) For the case of $H_p \leq H_p^*$, the magnetization vector, $\boldsymbol{M}$, is parallel to the external field, $\boldsymbol{H}$, and $\phi = 0$. By increasing the applied field the canting angle increases by $\Delta\psi = \pi/2 - \psi = (H + H_D)/2H_E$. (2) For $H_p > H_p^*$ and $p > 0$, one obtains $\cos\phi = \frac{HH_D}{2H_E(H_p - H_p^*) + HH_D}$ and $\Delta\psi = \frac{H_p}{H}\cos\phi$. Therefore, an orientational phase transition occurs depending on p at $H_p = H_p^*$. Further increasing p results in further rotation of $\boldsymbol{M}$ from the direction $\boldsymbol{M}||x$ to the perpendicular direction $\boldsymbol{M}||y$ when $H_p - H_p^* \gg HH_D/2H_E$. For $p < 0$ only state (1) is relevant. An analogous orientational phase transition can happen at a given pressure $p > 0$ by sweeping

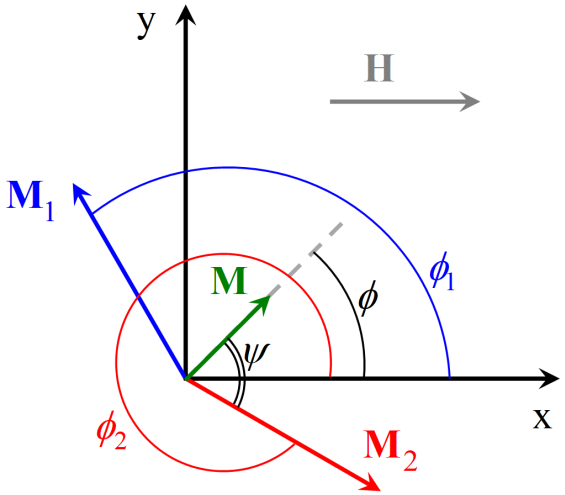

Figure 5.9: Sublattice magnetizations (red and blue arrows) in the canted state of hematite. Net magnetization (green arrow) makes an angle ϕ with the applied field direction (gray arrow). Angle ϕ is defined between the sublattice magnetizations and the net magnetization.

the applied field strength and hence, H_p^*. In this case, at $H = 0$ the magnetization vector aligns perpendicular to the direction of $\boldsymbol{p}$, i.e. $\boldsymbol{M}||y$. By increasing H the magnetization rotates from $\phi = \pi/2$ to $\phi = 0$ for the field range of $0 \leq H \leq H^*$, with $H^* = \sqrt{(H_D/2)^2 + 2H_E H_p} - H_D/2$. For $H \geq H^*$, state (1) is retrieved with $\boldsymbol{M}||\boldsymbol{H}||x$ after overcoming the in-plane anisotropy created by $\boldsymbol{p}$.
The qFMR mode for the state (1) with $H_p \leq H_p^*$ is given by

$$f_r = \frac{|\gamma|\mu_0}{2\pi}\sqrt{2H_E(H_{ME} + H_p^* - H_p)}. \tag{5.1}$$

For the state (2) with $H_p \geq H_p^*$ is given by

$$f_r = \frac{|\gamma|\mu_0}{2\pi}\sqrt{2H_E\left[H_{ME} + \frac{2H_E H_p - H^2 + HH_D}{2H_E H_p - H^2}(H_p - H_p^*) + H_M \sin^2\phi\right]}. \tag{5.2}$$

H_{ME} is the intrinsic magnetoelastic field and $H_M = \mu_0 M_0 \left(\frac{H+H_D}{H_E}\right)^2$ is the dipolar field due to the canting in response to a strong external field. From these equations, the qFMR frequency as a function of H (p) when a given p (H) is applied has a minimum at the phase transition point where $H = H^*$ ($H_p = H_p^*$). This frequency is given by the intrinsic magnetoelastic field as $f_{ME} = \sqrt{2H_E H_{ME}}$. A schematic illustration of Eqs. 5.1 and 5.2 as a function of H is shown in Fig. 5.10. The qFMR branch can have a more complicated form than shown in Fig. 5.10 and in particular, it may contain jumps [144].
Our thin films are, as mentioned earlier, under compressive strain from the substrate. This strain can be in-homogeneous as reported in Ref. [79]. Therefore, a spatial variation of SW spectra measured at different spots can originate from a local variation of H_p in the films.

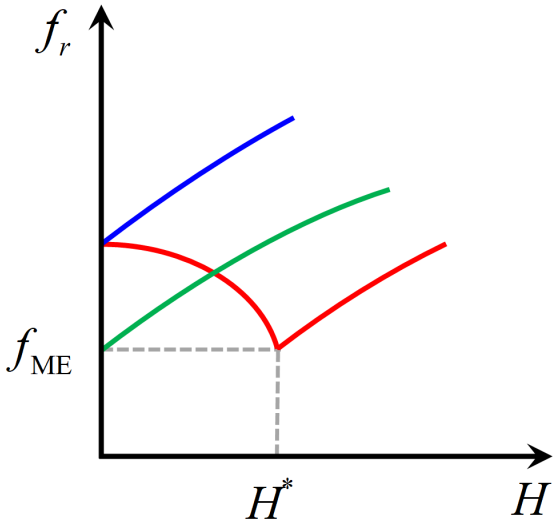

Figure 5.10: Field dependent qFMR frequency under external strain for a compressive strain ($H_p > 0$). Red (blue) curve indicates $\boldsymbol{H}||\boldsymbol{p}$ ($\boldsymbol{H} \perp \boldsymbol{p}$). The green curve represents $H_p = 0$.

Multiple peaks in the BLS spectra also can be explained by considering such a variation ($H_p = H_p(\boldsymbol{r})$) in the measured laser spot. As $H_p = H_p(\boldsymbol{r})$, different parts of the sample might be on different curves, $f_r(H)$, presented in Fig. 5.10. The mosaicity of the samples adds to the complexity of the spectra since it means that crystallographic axis directions exhibit some distribution as well. This is especially relevant as we have neglected the 6-fold anisotropy in the basal plane. Adding this anisotropy and considering a local variation of the strength and orientation of the net compressive strain from the substrate can result in a strain-defined magnetic texture that can persist at fields as high as 500 mT as reported in REf. [81]. The situation in our case would be even more pronounced as the thin films in Ref. [81] are relaxed in contrast to our strained films.
We have applied a magnetic field perpendicular to the a-axis in the plane in our measurements which is an easy axis direction for the 6-fold basal plane anisotropy. However, it is quite likely that for a given position in the sample, the direction of the net local strain is either parallel or perpendicular to the applied field direction. For example, the field dependency of the sample SB1 in Fig. 5.8 suggests that in the measured spot on the sample, $\boldsymbol{H}$ was perpendicular to $H_p(\boldsymbol{r})$ as the extracted f_r behaves similar to the blue curve in Fig. 5.10. However, in case of the spectra for SB2 and SB3 in Fig. 5.8, the behavior is similar to the red curve in Fig. 5.10 which indicates $\boldsymbol{H} \perp \boldsymbol{H}_p(\boldsymbol{r})$ in the laser spot for those specific measurements. For a quantitative analysis of the data we need micromagnetic simulations that support magnetoelastic effects in hematite together with more detailed information about the microstructure of the grown thin films. Unfortunately such a code is currently not available.

6 Theory of antiferromagnet based nano-constriction spin-Hall nano-oscillator

6.1 Terahertz Slonczewski propagating spin waves and large output voltage in antiferromagnetic spin-Hall nano-oscillators

M. Hamdi, and D. Grundler
arXiv 2206.07844 (2022)
doi: arXiv 2206.07844

My contribution to this paper included the derivation of analytical equations, micromagnetic simulations and data analysis. I wrote the draft of the manuscript.

Abstract

We study theoretically antiferromagnet (AFM) based spin-Hall nano-oscillators (SHNOs) consisting of a nano-constriction (NC) in a thin-film uniaxial AFM. By solving the derived SW equation we evidence radially propagating spin waves (SWs) at THz frequencies similar to the Slonczewski SWs known at GHz frequencies for a ferromagnet-based SHNO. We predict a minimum threshold current for a specific NC radius accessible by the state-of-the-art nanotechnology. The exchange interaction enhanced spin pumping for AFMs leads to a strong thickness dependent threshold frequency. We show that the uniaxial AFMs generate ac electrical fields via spin pumping that are three orders of magnitude larger than reported for biaxial AFMs. Our work enhances the fundamental understanding of current-driven SWs in AFM-SHNOs and enables optimization of practical devices in terms of material choice, device geometry, and frequency tunability. The propagating SWs offer remote THz signal generation and an efficient means for synchronization of SHNOs when aiming at high power.

Main body

Introduction

Terahertz (THz) radiation attracts tremendous attention due to its several promising applications including ultrafast communication [150, 151], biosensing and imaging [7, 8]. However, the widespread use of THz instrumentation is constrained, in particular, because of the lack of efficient sources and detectors of THz radiation for frequencies in the range of 0.1-10 THz (THz gap) [7, 8]. Therefore, there is an urgent need to develop small-sized solid-state THz sources and detectors. Spin wave (SW) excitations in antiferromagnetic materials (AFMs) offer frequencies which cover perfectly the THz gap. These materials can be utilized to close the THz gap in terms of antiferromagnetic spintronic and magnonic devices [2, 24, 25, 28–42, 152–159]. One of the most promising devices is the AFM-based spin-Hall nano-oscillator (AFM-SHNO) consisting of an AFM and a heavy metal (HM) layer [2, 25, 28–42]. In an AFM-SHNO, a spin current generated by the spin-Hall effect (SHE) in the HM enters the AFM layer and exerts the so-called spin-orbit torque (SOT) [57, 59, 61, 62]. It has been shown theoretically that when the spin current exceeds a certain threshold, damping can be compensated, and the magnetization starts self-sustained auto-oscillations. They can generate THz radiation via the combination of spin pumping [24–27] and inverse spin-Hall effect [2, 25, 28–42]. The AFM-SHNOs have potential not only as THz sources and detectors [2, 25, 28–40], but also as ultra-fast artificial neurons which generate picosecond-duration spikes [41, 42] and enable ultra-fast neuromorphic applications [43–46]. Howver, there has not yet been any report on the experimental realization of an AFM-SHNOs.

All the theoretical studies mentioned above were carried out by considering an AFM in the macrospin approximation. They described uniform antiferromagnetic resonance (AFMR) excitation by a spin current in planar bilayer HM/AFM structures [2, 25, 28–42]. Still, there have been few micromagnetic studies of SHNOs addressing the planar HM/AFM geometry and AFMR excitation [34, 35]. These studies do not describe however a realistic AFM-SHNO which incorporates a nano-constriction (NC) [160, 161]. NCs are essential for ferromagnet-based SHNOs (FM-SHNOs) which excite propagating SWs [57, 162, 163]. These SWs enable the efficient synchronization of FM-SHNOs [164–169] granting sufficient signal quality for applications.

In this chapter, we study theoretically and by means of micromagnetic simulations an NC-based AFM-SHNO and provide a fundamental understanding of its spin dynamics. We first derive the SW equation for an insulating AFM layer subjected to a spin current in a circular NC. We show that the solution to this equation is the antiferromagnetic counterpart of Slonczewski SWs known for ferromagnetic SHNOs. The Slonczewski spin waves are radially propagating waves generated by spin torque in a circular NC in a FM layer [57, 59]. We obtain the threshold frequency and current for such THz antiferromagnetic Slonczewski SWs (THz-ASSWs) as a function of the material parameters and the NC radius R. Our analytical results show good agreement with the micromagnetic simulations. A unique feature of these THz-ASSWs is that the threshold current exhibits a minimum with respect to the NC radius which allows one to reduce the power consumption to a minimum. Interestingly, the minimum diameter $2R$ is

in the range of few tens to few hundreds of nanometers for realistic material parameters and is realizable by state-of-the-art fabrication technology. Moreover, our results infer that other types of excitation such as the antiferromagnetic counterpart of the dynamic droplet soliton [170–172] originally predicted by Ivanov *et. al.* [173] can be realized in AFM-SHNOs which may lead to high power THz generation.

Theory

We consider an AFM-SHNO as a plane AFM film that is subjected to a spin current injected locally in a circular region of radius R, as depicted in Fig. 6.1 (a). Such spin current is generated by restricting the electric current in the adjacent HM into a nano-constriction [160, 161]. We assume an AFM with a uniaxial anisotropy in the plane along the x-axis and a thickness, d_{AF}, smaller than the exchange length, $\lambda_{ex} = \sqrt{a^2\omega_E/4\omega_A}$. Thereby we avoid standing waves along the thickness. Here, a is the magnetic lattice constant of the material and $\omega_E = \gamma H_E$ ($\omega_A = \gamma H_A$) is the exchange (anisotropy) field in the units of frequency with H_E (H_A) being the exchange (anisotropy) field and γ is the electron gyromagnetic ratio. The Néel order vector and average magnetization are defined as $\mathbf{n} = (\mathbf{M}_1 - \mathbf{M}_2)/2M_s$ and $\mathbf{m} = (\mathbf{M}_1 + \mathbf{M}_2)/2M_s$, respectively, where $\mathbf{n}.\mathbf{m} = 0$ and $|\mathbf{n}|^2 + |\mathbf{m}|^2 = 1$. $\mathbf{M}_i$ ($i = 1,2$) is the sublattice magnetization with saturation value of $M_s = |\mathbf{M}_i|$. We consider the polarization direction of the spin current, $\hat{\mathbf{p}}$, to be parallel to $\mathbf{n}$ where the SOT has the highest efficiency [35]. There is no externally applied magnetic field. The total magnetic free energy of the AFM is $F = \int f dV$, where the energy density, f, is given by [24, 25, 102, 174]

$$f = \frac{M_s}{\gamma} \quad \left\{ \frac{1}{2}\omega_E\left(\mathbf{m}^2 - \mathbf{n}^2\right) - \frac{1}{2}\omega_A\left(m_x^2 + n_x^2\right) - \frac{1}{2}\omega_A\lambda_{ex}^2\left[(\nabla\mathbf{m})^2 - (\nabla\mathbf{n})^2\right] \right\}. \tag{6.1}$$

The dynamics of $\mathbf{m}$ and $\mathbf{n}$ is governed by the Landau-Lifshitz-Gilbert-Slonczewski (LLGS) equations with the spin-torque term as

$$\dot{\mathbf{m}} = \left[\boldsymbol{\omega}_m \times \mathbf{m} + \boldsymbol{\omega}_n \times \mathbf{n} \right] + \boldsymbol{\tau}_m^{\mathrm{D}} + \boldsymbol{\tau}_m^{\mathrm{SOT}}, \tag{6.2a}$$

$$\dot{\mathbf{n}} = \left[\boldsymbol{\omega}_m \times \mathbf{n} + \boldsymbol{\omega}_n \times \mathbf{m} \right] + \boldsymbol{\tau}_n^{\mathrm{D}} + \boldsymbol{\tau}_n^{\mathrm{SOT}}, \tag{6.2b}$$

where $\boldsymbol{\omega}_m = -\frac{\gamma}{M_s}\frac{\delta F}{\delta \mathbf{m}}$ and $\boldsymbol{\omega}_n = -\frac{\gamma}{M_s}\frac{\delta F}{\delta \mathbf{n}}$ are the effective fields in frequency units [24, 25, 102, 174]. The damping torques are given by $\boldsymbol{\tau}_m^{\mathrm{D}} = \alpha\left(\mathbf{m}\times\dot{\mathbf{m}} + \mathbf{n}\times\dot{\mathbf{n}}\right)$ and $\boldsymbol{\tau}_n^{\mathrm{D}} = \alpha\left(\mathbf{m}\times\dot{\mathbf{n}} + \mathbf{n}\times\dot{\mathbf{m}}\right)$ where $\alpha = \alpha_0 + \alpha_{\mathrm{SP}}$ is the effective damping consisting of the Gilbert damping, α_0, and the enhanced damping due to spin pumping [24, 25], $\alpha_{\mathrm{SP}} = \frac{\gamma\hbar g_r}{4\pi M_s d_{AF}}$. Here, $\hbar$ and g_r are the reduced Planck constant and interface spin mixing conductance, respectively. The spin-torque terms are given as $\boldsymbol{\tau}_m^{\mathrm{SOT}} = \omega_s\left[\,\mathbf{m}\times\left(\mathbf{m}\times\hat{\mathbf{p}}\right) + \mathbf{n}\times\left(\mathbf{n}\times\hat{\mathbf{p}}\right)\,\right]H(R-r)$ and $\boldsymbol{\tau}_n^{\mathrm{SOT}} = \omega_s\left[\,\mathbf{m}\times\left(\mathbf{n}\times\hat{\mathbf{p}}\right) + \mathbf{n}\times\left(\mathbf{m}\times\hat{\mathbf{p}}\right)\,\right]H(R-r)$ where $\omega_s = \frac{2\hbar\gamma\theta_{SH}J_c\eta}{eM_s d_{AF}}$ with $\eta = \frac{\lambda_N G_r \tanh(d_N/2\lambda_N)}{\sigma_N + 2\lambda_N G_r \coth(d_N/\lambda_N)}$ is the SOT

strength in frequency units, $H(R-r)$ is the Heaviside step function and r is the radial distance from the center of the NC. θ_{SH}, λ_N, σ_N, d_N and J_c are spin-Hall angle, spin diffusion length, electrical conductivity, thickness and applied electric current of the HM, respectively, and $G_r = e^2 g_r/2\pi\hbar$ where $-e$ is the electron charge. We consider the ansatz $\mathbf{n} = n_0\hat{\mathbf{x}} + \mathbf{n}_\perp(x,y)\, e^{i\omega t}$ with $|\mathbf{n}_\perp(x,y)| \ll 1$ to derive the wave equation for small amplitude SWs excited by SOT. In the exchange limit ($\omega_A/\omega_E \ll 1$) which is the case for most antiferromagnets and the absence of an external field, $\mathbf{m} \simeq (\omega_A/\omega_E)\mathbf{n}_\perp \ll \mathbf{n}_\perp$ and $|n_0| \simeq 1$. By keeping the linear terms in $\mathbf{m}$ and $\mathbf{n}_\perp$ and eliminating $\mathbf{m}$ between the Eqs. 6.2a and 6.2b [175], we obtain two coupled equations for two components of $\mathbf{n}_\perp$ as

$$\left(\frac{\mp\omega^2}{2\omega_E+\omega_A}\right) n_{z(y)} = \mp\omega_A n_{z(y)} \mp i\alpha\omega n_{z(y)} + \omega_s n_{y(z)} \pm \omega_A \lambda_{ex}^2 \nabla^2 n_{z(y)}. \tag{6.3}$$

By defining the complex SW amplitude as $u = n_y + i n_z$, and the normalized distance $\tilde{r} = r/R$ and by adding the dispersive dissipation term , $i\alpha\omega_A\lambda_{ex}^2\nabla^2 u$, which describes the increase of the relaxation rate with the wave vector k of the excited SW [176, 177], we obtain the SW equation as [175]

$$\frac{1}{\tilde{r}}\frac{\partial}{\partial\tilde{r}}\left(\tilde{r}\frac{\partial u}{\partial\tilde{r}}\right) + Au + iBu + \alpha Bu - i\alpha Cu = 0, \tag{6.4a}$$

$$A = \left(\frac{R^2}{\omega_A\lambda_{ex}^2}\right)\left(\frac{\omega^2}{2\omega_E+\omega_A} - \omega_A\right), \tag{6.4b}$$

$$B = \left(\frac{R^2}{\omega_A\lambda_{ex}^2}\right)\omega_s H(1-\tilde{r}), \tag{6.4c}$$

$$C = \left(\frac{R^2}{\omega_A\lambda_{ex}^2}\right)\left[\omega + \frac{\omega^2}{2\omega_E+\omega_A} - \omega_A\right]. \tag{6.4d}$$

One can summarize Eqs. 6.4a-6.4d as $\frac{1}{\tilde{r}}\frac{\partial}{\partial\tilde{r}}\left(\tilde{r}\frac{\partial u}{\partial\tilde{r}}\right) + k_i^2 u = 0$, which is the Bessel equation with complex wave vector $k_1 = \sqrt{A + iB + \alpha(B - iC)}$ for $0 \le \tilde{r} \le 1$ and $k_2 = \sqrt{A - i\alpha C}$ for $\tilde{r} > 1$. Following Slonczewski [58, 162, 178], we take a piecewise Bessel solution of the form

$$u(\tilde{r}) = \begin{cases} J_0(k_1\tilde{r}); & 0 \le r \le 1, \\ cH_0^{(1)}(k_2\tilde{r}); & r > 1, \text{ with } c = \dfrac{J_0(k_1\tilde{r})}{H_0^{(1)}(k_2\tilde{r})}, \end{cases} \tag{6.5}$$

where $J_0(x)$ and $H_0^{(1)}(x)$ are the Bessel and Hankel functions of the first kind, respectively. The continuity of the derivative of u at the NC boundary $\tilde{r} = 1$, leads to a complex transcendental equation whose real and imaginary parts determine two real eigenvalues ω and ω_s at the threshold [58, 175, 178]. By solving this equation we have derived the frequency of the excited mode and required current density at the threshold as

$$\omega_{\rm th} = \frac{\alpha A_{12}\,(2\omega_E+\omega_A)}{2\,(1-\alpha A_{12})} + \sqrt{\left[\frac{\alpha A_{12}\,(2\omega_E+\omega_A)}{2\,(1-\alpha A_{12})}\right]^2 + (2\omega_E+\omega_A)\left[\omega_A+\left(\frac{A_0+\alpha A_{11}}{1-\alpha A_{12}}\right)\left(\frac{\omega_A\lambda_{ex}^2}{R^2}\right)\right]}, \quad (6.6)$$

$$J_{c,\rm th} = \left(\frac{eM_s d_{AF}}{2\gamma\hbar\theta_{SH}\eta}\right)\left\{\left(\frac{\alpha B_{12}}{1-\alpha A_{12}}\right)\omega_{\rm th}+\left(\frac{\omega_A\lambda_{ex}^2}{R^2}\right)\left[B_0+\alpha B_{11}+\alpha B_{12}\left(\frac{A_0+\alpha A_{11}}{1-\alpha A_{12}}\right)\right]\right\}, \quad (6.7)$$

respectively, where $A_0 = 1.428$, $A_{11} = -3.087$, $A_{12} = 0.815$, $B_0 = 1.863$, $B_{11} = -1.581$ and $B_{12} = 1.004$.

Micromagnetic simulations

We use the Object Oriented MicroMagnetic Framework (OOMMF) [98] which solves the LLGS equation based on the finite difference method to validate the analytical expressions derived from the continuum model (Eqs. 6.6 and 6.7). These simulations are performed on a cuboid-like mesa with dimensions of 2 μm×2 μm×1 nm, divided into 2000×2000×1 cells. A circular NC with a radius of R is defined at the center of the device for spin current driven excitations (Fig. 6.1(a)). In order to compare the simulations with our theoretical results, we performed the simulations for different NC radii of $R = 10$, 25, 75 and 125 nm. In all the simulations, we used $M_s = 350$ kA/m, $K_x = 20$ kJ/m^3, $\alpha = 0.001$ as the sublattice saturation magnetization, magnetic anisotropy and Gilbert damping, respectively. In order to achieve antiferromagnetic order, we used $A_{ex} = -10$ pJ/m as the exchange stiffness in OOMMF simulations. This corresponds to a two-sublattice G-type antiferromagnet with homogeneous (nonhomogeneous) exchange constant of $A_h = -4A_{ex}/a^2$ ($A_{nh} = -A_{ex}$) with the magnetic lattice constant $a = 1$ nm (See Supplemental Material [175]). These parameters correspond to $\mu_0 H_E = 228.57$ T and $\mu_0 H_A = 0.114$ T which are in the range of material parameters for the existing AFMs. For HM material parameters we considered $d_{HM} = 10$ nm, $\theta_{SH} = 0.15$, $\lambda_{HM} = 7$ nm and $\sigma_N = 2.083\times10^6\ \Omega^{-1}\mathrm{m}^{-1}$. Considering $g_r = 6.9\times10^{18}$ m^{-2} [24] results in $\eta = 0.18$ for the interface. Absorbing boundaries were used to prevent back-reflection and interference effects [179]. The time dependent Néel order vector of the AFM layer under the d.c. current was sampled every 0.1 ps for a total number of 1000 samplings for each simulation.

Results and discussion

By taking the fast-Fourier-transform (FFT) of **n** we obtain the power spectral density (PSD) of the magnetization dynamics. Varying the current density and extracting the peak position of the PSD, we obtained the frequency versus current density curve of the SHNOs plotted in Fig.

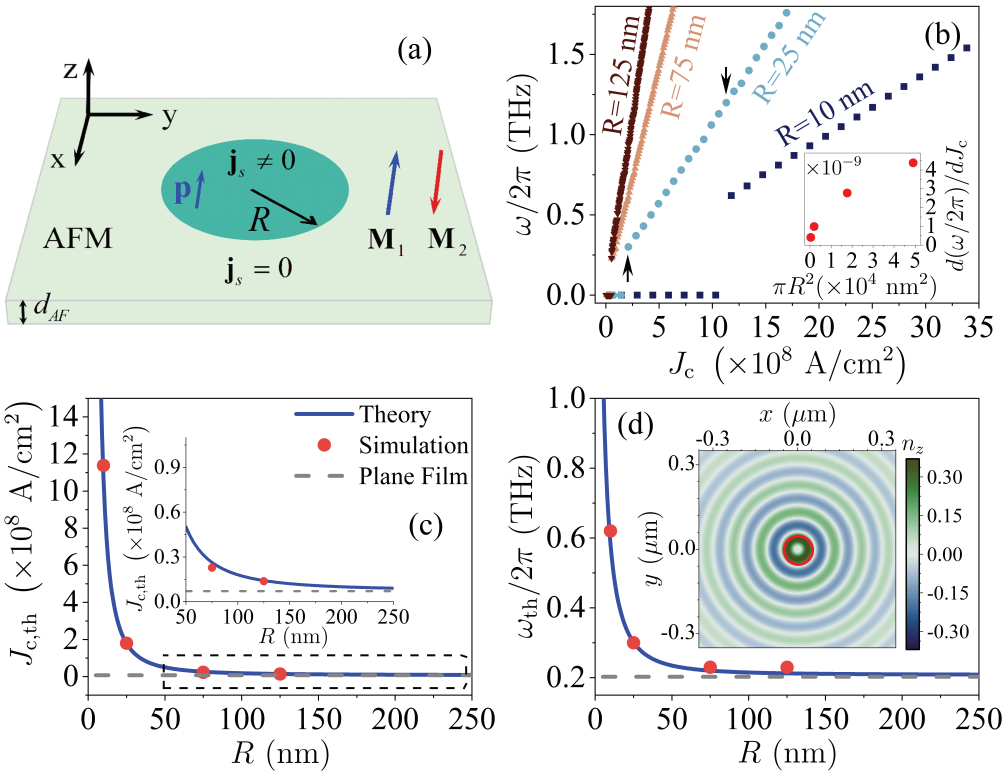

Figure 6.1: (a) Schematics of the studied system. The spin current with polarization **p** originates from the SHE of the electric current constrained in a circular NC of radius R in the adjacent HM layer. The spin polarization of the spin current is assumed to be along the Néel order vector. (b) Excitation frequency versus applied current density for the simulated SHNOs with different NC radii R. The black upward (downward) arrow indicates the mode for $R = 25$ nm at threshold $J_{c,\mathrm{th}} = 2.12 \times 10^8$ A/cm^2 with $f_{\mathrm{th}} = 0.3$ THz ($J_{c,\mathrm{h}} = 11.3 \times 10^8$ A/cm^2 with $f_{\mathrm{h}} = 1.2$ THz) which is selected to calculate output electric fields due to spin pumping in Fig. 6.4. The slope β as a function of R^2 is shown in the inset. Threshold current density (c) and frequency (d) obtained from simulations (filled red circles) and Eqs. 6.7 and 6.6 (blue line), respectively. Gray dashed lines indicate the plane film limit. Inset in (d) shows a snapshot of current induced SW at threshold for SHNO with $R = 50$ nm (marked with red circle) and simulation parameters given in the text.

6.1(b). The frequency variation for large currents is attributed to the excessive SOT beyond threshold according to $\omega = \omega_{\mathrm{th}} + \beta(J_c - J_{\mathrm{th}})$. The inset in Fig. 6.1(b) shows the SW frequency shift coefficient $\beta = d\omega/dJ_c$ as a function of the NC area. β as determined from micromagnetic simulations increases with R and seems to asymptotically approach the macrospin limit. The observed tunability of β goes beyond macrospin studies where β is a constant and can be used to engineer NC performance.

Now we focus on the dynamics at the threshold. At the threshold, the PSD peak jumps from zero to the threshold frequency. Here, the dynamics of the SHNO is in the linear regime. The threshold current density and corresponding frequency decrease with the NC radius are plotted in Fig. 6.1(c) and (d), respectively. The values $J_{c,\mathrm{th}}$ obtained from micromagnetic

simulations (red symbols) are plotted with an offset of $\Delta J = -0.4 \times 10^8$ A/cm^2. We attribute this systematic error to the Taylor expansion of the complex transcendental equation that we employed to solve the eigenvalue problem [175]. The fixed offset does not affect the main conclusion of the comparison, i.e., the significant dependency of $J_{c,\mathrm{th}}$ on R making a geometrical optimization of an NC device necessary. The inset in Fig. 6.1(c) shows a zoom in of the region indicated by dashed rectangle. By considering the constant offset, the remaining discrepancies amount to only -1% and 6% which can be due to the coarse sweeping of the applied current in the simulations.

For large $R \gg \lambda_{ex}$ the threshold current density $J_{c,\mathrm{th}}$ (frequency ω_{th}) asymptotically approaches the AFMR limit in a thin film, $J_{c,\mathrm{th}} = \left(\frac{eM_s d_{AF}}{2\gamma\hbar\theta_{SH}\eta}\right)\alpha\omega_0$ ($\omega_0 = \sqrt{(2\omega_E + \omega_A)\omega_A}$), indicated by the gray dashed line in Fig. 6.1(c) (6.1(d)). The inset in Fig. 6.1(d) shows a snapshot of the spin-current-generated spin wave simulated for $R = 50$ nm. For small R (below almost $\lambda_{ex} = 22.3$ nm), the exchange term dominates and the threshold current density and frequency are large. One can understand the increase in threshold current density with decreasing R by considering the energy flow away from the NC by outgoing SWs. The wave vector, k, of the excited spin wave at the threshold is comparable to $2\pi/R$. Therefore, by decreasing R one increases k and the group velocity of the excited wave (following the dispersion in Eq. 6.6) and hence, the propagating energy away from the NC. To sustain this energy flow, a higher threshold current is necessary.

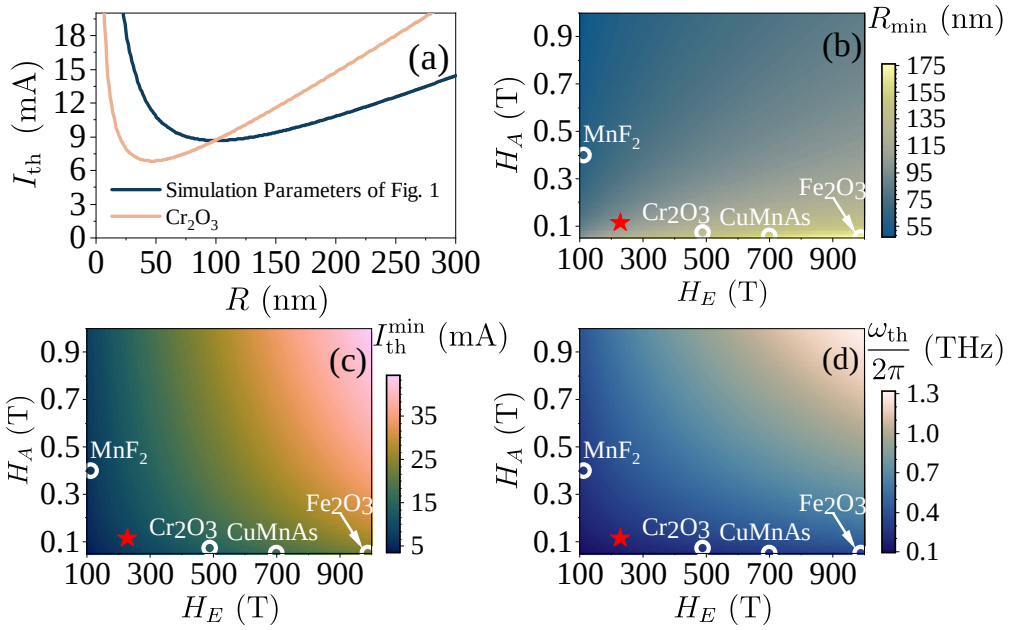

Figure 6.2: (a) Threshold current, I_{th}, as a function of R for the parameters used in Fig. 6.1 (blue line). The orange line considers Cr_2O_3 material parameters with the same HM and interface parameters as Fig. 6.1. NC radius (b), threshold current (c) and frequency (d) at the minimum point of $I_{\mathrm{th}}(R)$ as a function of exchange and anisotropy fields. For all graphs we considered $d_{AF} = 20$ nm as well as the corresponding α_{SP}. Red asterisks indicate the material parameters used in Fig. 6.1. White circles highlight further AFMs.

For practical applications the power consumption of the SHNO is of crucial importance. Approximating the current passing part of the NC in HM as a resistance with the length $L = 2R$ and cross-sectional area $S = 2Rd_N$ in the $xz-$plane one obtains its resistance as $\sim (L/\sigma_N S) = 1/\sigma_N d_N$ which is independent of R. By multiplying Eq. 6.7 by S we obtain the threshold current as

$$I_{\rm th}(R) = \alpha \mathcal{A} \omega_{\rm th} R + (\mathcal{B}\lambda_{ex}^2/R). \tag{6.8}$$

The first term in this equation represents the current needed to overcome the damping which grows linearly with R. The second term reflects the propagation energy which scales with R^{-1}. The combination of these two terms leads to a minimum threshold current, $I_{\rm th}^{\rm min}$, with respect to R. In Fig. 6.2(a) we depict $I_{\rm th}$ as a function of R for the parameters used in Fig. 6.1 (blue line). For comparison, we display $I_{\rm th}(R)$ for the uniaxial antiferromagnet Cr_2O_3 (orange line) with material parameters of $M_s = 45.5$ kA/m, $H_E = 490$ T, $H_A = 0.035$ T and $a = 1$ nm [47, 180]. Since $\omega_{\rm th}$ is a slowly varying function of R for $R \gtrsim 2\lambda_{ex}$ (Fig. 6.1(d)) away from the exchange dominated regime, we neglect its dependency on R, for large R and obtain $R_{\rm min} \simeq \sqrt{\frac{\mathcal{B}\lambda_{ex}^2}{\alpha \mathcal{A} \omega_{\rm th}^{\rm min}}}$ where $R_{\rm min}$ and $\omega_{\rm th}^{\rm min}$ are the NC radius and threshold frequency at the threshold current minimum, respectively. This expression slightly underestimates $R_{\rm min}$. In Fig. 6.2(b), (c) and (d) we depict $R_{\rm min}$, $I_{\rm th}^{\rm min}$ and $\omega_{\rm th}^{\rm min}$, respectively, as a function of H_E and H_A (for a set of parameters that hold the exchange limit) which are numerically obtained by minimizing $I_{\rm th}(R)$. Figure 6.2 (b) shows that $R_{\rm min}$ increases (decreases) by increasing H_E (H_A). However, $I_{\rm th}^{\rm min}$ (Fig. 6.2 (c)) and $\omega_{\rm th}^{\rm min}$ (Fig. 6.2 (d)) increase by increasing both H_E and H_A. The parameters used for simulations is indicated with the red aster. White circles indicate some of the most interesting materials for AFM spintronics [14, 26, 27, 47, 120, 121, 124, 136, 180–184] which all of them fall in the exchange limit and our theory holds.

Due to the large exchange field in AFMs, the effect of damping on $I_{\rm th}(R)$ is enhanced (Eq. 6.7 and 6.8). Therefore, we evaluate the effect of AFM thickness which drastically influences $\alpha_{\rm SP}$. The intrinsic Gilbert damping, α_0, is in the order of $10^{-6} - 10^{-4}$ for insulating AFMs [14, 121, 124, 136, 183] which is negligibly small compared to $\alpha_{\rm SP}$ for thin films. Figure 6.3(a) shows $\alpha_{\rm SP}$ for the AFM simulated in Fig. 6.1 and Cr_2O_3. Since M_s for Cr_2O_3 is small, $\alpha_{\rm SP}$ depends prominently on d_{AF}. Despite the large $\alpha_{\rm SP}$ for Cr_2O_3, its $I_{\rm th}^{\rm min}$ (orange curve) is considerably smaller compared to the AFM with large M_s (blue curve) as is shown in Fig. 6.3(b). Though $\alpha_{\rm SP}$ decreases by increasing d_{AF}, $I_{\rm th}^{\rm min}$ increases since SOT is an interface effect and scales with d_{AF}^{-1}. $R_{\rm min}$ and $\omega_{\rm th}^{\rm min}$ as a function of d_{AF} are shown in Fig. 6.3(c) and (d), respectively. $R_{\rm min}$ increases as a function of d_{AF} (Fig. 6.3(c)) since $R_{\rm min} \propto \sqrt{\alpha_{\rm SP}^{-1}} \propto \sqrt{d_{AF}}$ and $\mathcal{A}$ and $\mathcal{B}$ are slowly varying functions of α. Despite having larger H_E and smaller H_A, Cr_2O_3 has smaller $R_{\rm min}$ due to larger $\alpha_{\rm SP}$ and $\omega_{\rm th}^{\rm min}$. Though the AFMR frequency of Cr_2O_3 (164 GHz) is lower than the AFMR of Fig. 6.1 (202.5 GHz), the threshold frequency at $I_{\rm th}^{\rm min}$ is higher for Cr_2O_3 (Fig. 6.3(d)). The higher frequency is a consequence of low M_s which results in a significant change of $\alpha_{\rm SP}$ with d_{AF}.

In the following we make use of the predicted spin dynamics and evaluate electrical signals that arise due to spin pumping into an adjacent HM layer. The dynamic part of the Néel vector, $\mathbf{n}(r,t)$, gives rise to spin pumping which scales with $\mathbf{j}_s = (\mathbf{n} \times \dot{\mathbf{n}}) \times \hat{\mathbf{z}}$ [24, 28, 29]. By adding

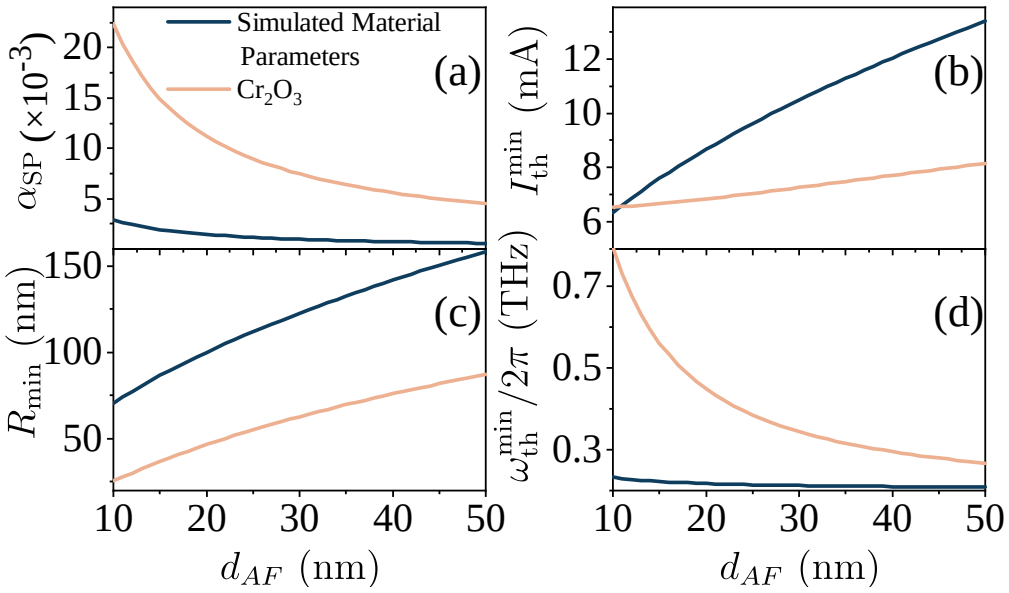

Figure 6.3: Spin pumping induced damping, α_{SP} (a) threshold current I_{th}^{min} (b), NC size R_{min} (c) and threshold frequency, ω_{th}^{min} (d) at the threshold current minimum as a function of AFM layer thickness, d_{AF}.

a HM layer either above or below the AFM, an ac electrical field is generated according to $\mathbf{E} = \mathcal{E}\mathbf{j}_s = \mathcal{E}(\mathbf{n}\times\dot{\mathbf{n}})\times\hat{\mathbf{z}}$ with $\mathcal{E} = \hbar\eta\theta_{SH}/ed_N$ [28]. Taking the complex SW amplitude, u, we obtain the ac signal [175]

$$E_{ac}(r,t) \quad = \quad \mathcal{E}n_x\dot{n}_z = \mathcal{E}\omega\sqrt{1-|u(r)|^2}\,\mathrm{Re}\left\{u(r)e^{i\omega t}\right\}. \tag{6.9}$$

We numerically calculated $\mathbf{j}_s = (\mathbf{n}\times\dot{\mathbf{n}})\times\hat{\mathbf{z}}$ for each cell at each moment in time from micromagnetic simulations. We took the FFT of this quantity, multiplied by $\mathcal{E} = 0.7\times10^{-7}$ V.s/cm and color-coded the absolute values as shown for two different currents J_c applied to an NC with $R = 25$ nm in Fig. 6.4(a) and (b). Thereby, we evaluate the spin pumping at $f_{th} = 0.3$ THz and $f_h = 1.2$ THz, respectively. We display its spatially inhomogeneous characteristics in units of V/cm. The panels of Fig. 6.4(a) and (b) hence show ac electric fields in the typical HM assumed above. They allow for a straightforward comparison with the earlier reports on spin pumping from biaxial AFMs. For the f_{th} mode, the maximum spin pumping signal is obtained in the NC, while for the f_h mode, E_{ac} vanishes under the NC. This result is explained by Fig. 6.4(c) illustrating the spin-precessional motion at f_{th} (blue) and f_h (red) in the center of the NC. For f_{th}, the SOT excites a conically precessing Néel vector (See Supplemental video 1 [175]) with a well-defined elliptical polarization and a cone angle smaller than $\pi/2$. At large J_c (SOT), the cone angle reaches $\pi/2$ and the Néel vector precesses entirely in the yz-plane (See Supplemental video 2 [175]). In this case, the spin-precessional amplitude $|u(r)|$ is maximum ($|u(r)| = 1$). In Fig. 6.4(d) we depict the quantity $j_{s,ac} = |u(r)|\sqrt{1-|u(r)|^2}$ as a function of $|u(r)|$. The striking feature of $j_{s,ac}$ is the maximum ac spin pumping at $|u|_{max} = \sqrt{2}/2$. Consistent with the macrospin approximation applied in Ref. [29], we observe zero spin pumping

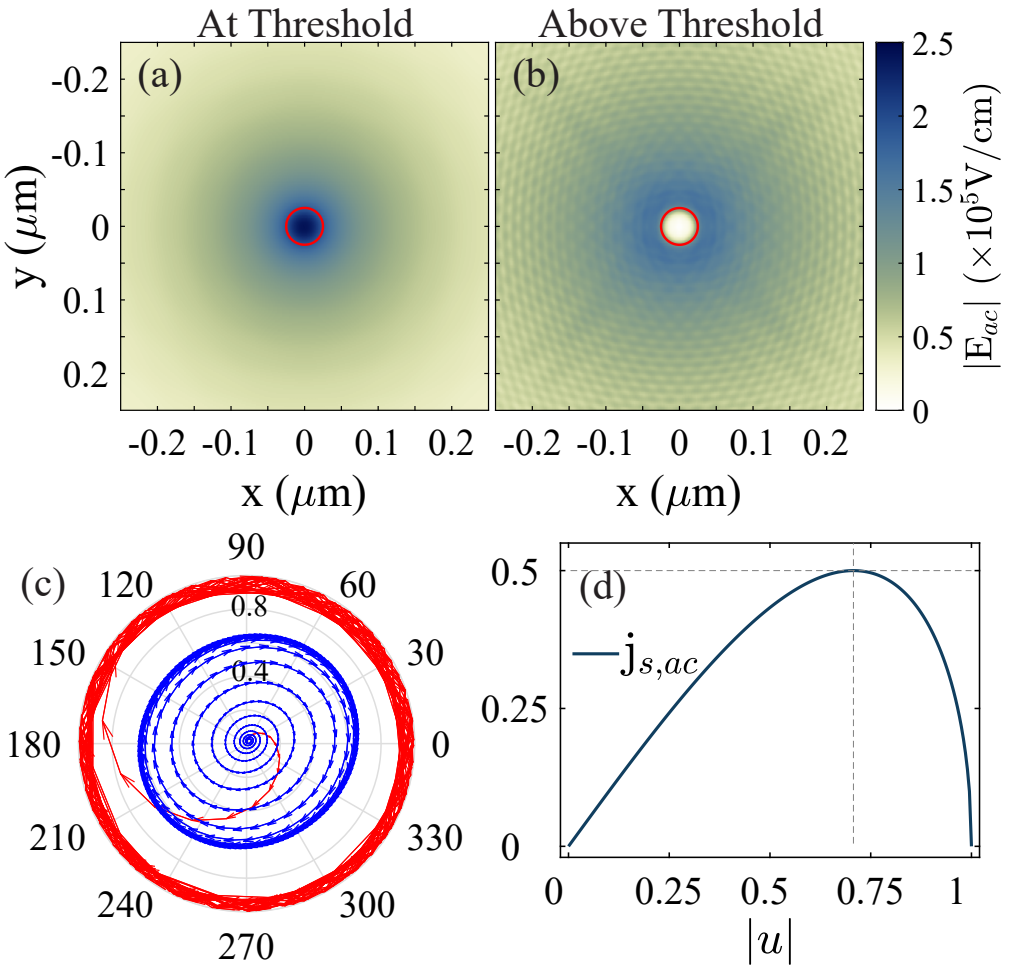

Figure 6.4: Spin pumping induced ac output electric field for modes (a) f_{th} at threshold and (b) f_{h} above threshold. Red circule marks the NC. (c) Time dependent dynamic Néel vector for f_{th} (blue) and f_{h} (red). The arrows indicate the direction of time. (d) The dimensionless parameter $j_{s,ac} = |u|\sqrt{1-|u|^2}$ as a function of the spin wave amplitude $|u|$.

inside the NC when a large J_c gives rise to $|u(r)| = 1$. But, the zero-spin pumping is no longer true for the discovered Slonzweski waves propagating into the AFM. Outside the NC a region is found where due to damping the amplitude $|u|_{\max} = \sqrt{2}/2$ is realized and maximum ac spin pumping occurs remotely from the NC. The predicted excitation of propagating THz-ASSWs makes uniaxial AFMs a promising material for SHNOs as they exhibit a lower threshold current and enable 3 orders of magnitude larger values $|E_{ac}|$ than the earlier considered biaxial AFMs [28, 29]. In Eq. 6.9, we find $|E_{ac}|$ to be proportional to the operational frequency ω, whereas for biaxial AFMs one finds $|E_{ac}| \propto \frac{\omega_e \omega_E}{4\sqrt{\alpha^2\omega_E^2+\omega^2}}$. The latter value is orders of magnitude smaller due to small biaxial anisotropy ω_e.

Conclusion

We have derived and solved the spin wave equation for a realistic SHNO considering AFMs with uni-axial anisotropy. We find propagating THz Slonzewski waves which allow one to generate large ac electrical fields via spin pumping into an adjacent heavy metal film. At the same time, synchronization between neighboring SHNOs via propagating SWs might arise. The predicted waves hence open unprecedented pathways for dc current driven THz signal generation by means of magnons in thin-film AFMs.

Acknowledgement

We thank SNSF for financial support via grant 177550.

7 Summary and Outlook

In this thesis we have addressed AFMs for their potential role in AFM magnonics, both in the GHz and THz frequency regime. In this chapter I provide a short summary of the main results and an outlook on possible future studies and challenges.

In Sec. 4.1 we studied the GHz branch of magnons in the canted antiferromagnet hematite at room temperature. Employing broadband microwave spectroscopy in flip-chip configuration, we extracted exchange, DMI and anisotropy field in hematite. From these measurements we determined a damping coefficient of 1.1×10^{-5}. By means of wave vector resolved inelastic Brillouin light scattering we measured the magnon dispersion relation of the low frequency branch for wave vectors k which are relevant for timely experiments in magnonics. We observed magnon group velocities of up to 23 km/s for a large regime of wave vectors up to $k \approx 24$ rad/μm and obtained the exchange stiffness length to be relatively short and only about 1 Å. We estimated a very large SW decay length of 1.1 cm in a small magnetic field of 30 mT similar to the best YIG. These observations put hematite in a rivalry position to be the next "fruit fly" of magnonics instead of YIG. As hematite is an antiferromagnet, it is expected that the effect of dipolar interaction will be absent that deteriorates the SW group velocities in YIG thin films. Thus order of magnitude larger SW group velocities than in YIG thin films are expected in hematite thin films. Such high group velocities not only eliminate the need for extra magnetic elements e.g. magnetic grating couplers, but also promise high speed and energy efficient magnonic devices.

In chapter 5 we investigated SWs in thin films of hematite. We developed a recipe for the growth of high quality thin films by successive sputtering on sapphire substrate at room temperature and successive rapid thermal annealing of ultra-thin (5 nm) layers of hematite. We assessed the quality of thin films by means of $\theta - 2\theta$, ϕ-scan and reciprocal space mapping XRD, which indicated that a high level of epitaxy was established. The grown films were highly strained without twin domains. We studied SWs in these thin films by means of BLS spectroscopy at room temperature. To the best of our knowledge, we report here the first BLS spectroscopy measurements done on antiferromagnetic thin films. Taking advantage of the scanning function and high resolution of micro-focus BLS (300 nm), we detected a pronounced spatial variation of the SW frequency in our thin films. Furthermore, we observed

multiple SW modes whose frequencies did not strictly follow the field dependent behavior measured in the bulk sample reported in Sec. 4.1. They often showed jumps in the low field regime (12-40 mT). We attribute the large spatial variation, multiple modes and jumps in the SW frequencies to the strain gradients in the film due to substrate clamping and the magnetoelastic effects which are very strong in hematite. Our results showcase a crucial unanticipated challenge for AFM magnonics, which is to obtain strain-free thin films. Such magnetoelastically homogeneous thin films are essential to harvest a long decay length and high group velocity of GHz SWs in hematite.

In chapter 6 we present a theoretical and micromagnetic simulation study of a uniaxial AFM based SHNO consisting of a nano-constriction region. By solving the derived SW equation we evidence radially propagating THz Slonczewski SWs. We show that these SWs possess a minimum threshold current with respect to the NC radius accessible by the state-of-the-art nanotechnology. We demonstrate that when used in the form of NC-based SHNOs, uniaxial AFMs generate ac electrical fields via spin pumping that are three orders of magnitude larger than suggested by biaxial AFMs. Our work provides a fundamental understanding of spin dynamics in AFM-SHNOs and enables optimization of practical devices in terms of materials choice, device geometry, and frequency tunability. Propagating SWs not only enable remote generation of THz signals but also offer an efficient means for synchronizing SHNOs. We hope that our results spark investigations of such synchronization schemes between AFM-SHNOs. We expect that when excited in uniaxial AFMs with the right sign of second order anisotropy, these AFM Slonczewski SWs would be modulationally unstable and convert to dynamical droplet solitons as predicted in Ref. [185]. Surprisingly, second order anisotropy in hematite fulfills the criteria for formation of such dynamical solitons. Therefore, one might be able to excite the soliton mode in thin films of hematite in which the Morin transition is restored and uniaxial phase is accessible.

Appendix Part

A Supplementary Information: Terahertz Slonczewski propagating spin waves and large output voltage in antiferromagnetic spin-Hall nano-oscillators

M. Hamdi, and D. Grundler
arXiv 2206.07844 (2022)
doi: arXiv 2206.07844

My contribution to this paper included the derivation of analytical equations, micromagnetic simulations and data analysis. I wrote the draft of the manuscript. Supplementary of the draft have been reformatted, the content of Sec. A.1 and A.2 was not modified.

A.1 Slonczewski Spin wave

In this section we present a detailed derivation of the spin wave equation and the corresponding solution of it for our system. We start with the magnetic free energy density of a uniaxial antiferromagnet without the parity breaking term [24, 25, 102, 174] as

$$f = \frac{M_s}{\gamma}\left\{\frac{1}{2}\omega_E\left(\mathbf{m}^2-\mathbf{n}^2\right)-\frac{1}{2}\omega_A\left[(\mathbf{m}.\hat{\mathbf{u}})^2+(\mathbf{n}.\hat{\mathbf{u}})^2\right]-\frac{1}{2}\omega_A\lambda_{ex}^2\left[(\nabla\mathbf{m})^2-(\nabla\mathbf{n})^2\right]\right\}. \tag{A.1}$$

We will show in Sec. A.2 the correspondence between this continuum model and the micromagnetic simulations. The equations of motion for **m** and **n** are given by

$$\dot{\mathbf{m}} = \left[\boldsymbol{\omega}_m \times \mathbf{m} + \boldsymbol{\omega}_n \times \mathbf{n} \right] + \boldsymbol{\tau}_m^{\mathrm{D}} + \boldsymbol{\tau}_m^{\mathrm{SOT}}, \tag{A.2}$$

$$\dot{\mathbf{n}} = \left[\boldsymbol{\omega}_m \times \mathbf{n} + \boldsymbol{\omega}_n \times \mathbf{m} \right] + \boldsymbol{\tau}_n^{\mathrm{D}} + \boldsymbol{\tau}_n^{\mathrm{SOT}}. \tag{A.3}$$

All the parameters in Eqs. A.1, A.2 and A.3 are described in the main text. The effective fields in frequency unit are given by the functional derivative of total free energy, $F = \int f dV$ as

$$\boldsymbol{\omega}_m = -\frac{\gamma}{M_s}\frac{\delta F}{\delta \mathbf{m}} = -\frac{\gamma}{M_s}\left[\frac{\partial f}{\partial \mathbf{m}} - \nabla.\frac{\partial f}{\partial \nabla \mathbf{m}}\right] = -\left[\omega_E \mathbf{m} - \omega_A \left(\mathbf{m}.\hat{\mathbf{u}}\right)\hat{\mathbf{u}} + \omega_A \lambda_{ex}^2 \nabla^2 \mathbf{m}\right], \tag{A.4}$$

$$\boldsymbol{\omega}_n = -\frac{\gamma}{M_s}\frac{\delta F}{\delta \mathbf{n}} = -\frac{\gamma}{M_s}\left[\frac{\partial f}{\partial \mathbf{n}} - \nabla.\frac{\partial f}{\partial \nabla \mathbf{n}}\right] = -\left[-\omega_E \mathbf{n} - \omega_A \left(\mathbf{n}.\hat{\mathbf{u}}\right)\hat{\mathbf{u}} - \omega_A \lambda_{ex}^2 \nabla^2 \mathbf{n}\right]. \tag{A.5}$$

We consider the linear excitation of the form $\mathbf{n} = n_0\hat{\mathbf{x}} + \mathbf{n}_\perp\left(x,y\right)e^{i\omega t}$ with $|\mathbf{n}_\perp\left(x,y\right)| \ll 1$ to derive the wave equation for small amplitude spin waves excited by spin-orbit torque. In the exchange limit ($\omega_A/\omega_E \ll 1$) which is the case for most of the antiferromagnets and in the absence of an external field, $\mathbf{m} \simeq (\omega_A/\omega_E)\mathbf{n}_\perp \ll \mathbf{n}_\perp$ and $|n_0| \simeq 1$. By keeping only the linear terms in $\mathbf{n}_\perp$, we consider the damping terms as

$$\boldsymbol{\tau}_m^{\mathrm{D}} = \alpha(\mathbf{m} \times \dot{\mathbf{m}} + \mathbf{n} \times \dot{\mathbf{n}}) \simeq \alpha \mathbf{n} \times \dot{\mathbf{n}}, \tag{A.6}$$

$$\boldsymbol{\tau}_n^{\mathrm{D}} = \alpha(\mathbf{m} \times \dot{\mathbf{n}} + \mathbf{n} \times \dot{\mathbf{m}}) \simeq 0, \tag{A.7}$$

and the spin-orbit torque terms as

$$\boldsymbol{\tau}_m^{\mathrm{SOT}} = \omega_s\left[\mathbf{m} \times \left(\mathbf{m} \times \hat{\mathbf{p}}\right) + \mathbf{n} \times \left(\mathbf{n} \times \hat{\mathbf{p}}\right)\right] H(R-r) \simeq \omega_s\left[\mathbf{n} \times \left(\mathbf{n} \times \hat{\mathbf{p}}\right)\right] H(R-r), \tag{A.8}$$

$$\boldsymbol{\tau}_n^{\mathrm{SOT}} = \omega_s\left[\mathbf{m} \times \left(\mathbf{n} \times \hat{\mathbf{p}}\right) + \mathbf{n} \times \left(\mathbf{m} \times \hat{\mathbf{p}}\right)\right] H(R-r) \simeq 0. \tag{A.9}$$

Applying these considerations and plugging in Eqs. A.4 and A.5 to Eq. A.3 results in

$$\begin{aligned}\dot{\mathbf{n}} &= (\boldsymbol{\omega}_m \times \mathbf{n} + \boldsymbol{\omega}_n \times \mathbf{m}) \\ &= \left(-\omega_E \mathbf{m} + \omega_A m_x \mathbf{x} - \omega_A \lambda_{ex}^2 \nabla^2 \mathbf{m}\right) \times \mathbf{n} + \left(\omega_E \mathbf{n} + \omega_A n_x \mathbf{x} + \omega_A \lambda_{ex}^2 \nabla^2 \mathbf{n}\right) \times \mathbf{m} \\ &= (2\omega_E + \omega_A)\, \mathbf{n}_0 \times \mathbf{m}. \end{aligned} \tag{A.10}$$

We take the time derivative of Eq. A.10 considering $\mathbf{n} = n_0 \hat{\mathbf{x}} + \mathbf{n}_\perp (x, y)\, e^{i\omega t}$ which results in $\ddot{\mathbf{n}} = -\omega^2 \mathbf{n}_\perp = (2\omega_E + \omega_A)\, \mathbf{n}_0 \times \dot{\mathbf{m}}$. by taking the cross product between this equation and $\mathbf{n}$ and rearrangement of the terms we obtain

$$\dot{\mathbf{m}} = \begin{bmatrix} \dot{m}_y \\ \dot{m}_z \end{bmatrix} = \left(\frac{\omega^2}{2\omega_E + \omega_A}\right) \begin{bmatrix} -n_z \\ n_y \end{bmatrix} = \left(\frac{\omega^2}{2_E + \omega_A}\right) \mathbf{n}_0 \times \mathbf{n}_\perp. \tag{A.11}$$

Plugging Eqs. A.4, A.5, A.6 and A.8 into Eq. A.2 considering $\mathbf{n} \times \left(\mathbf{n} \times \hat{\mathbf{p}}\right) = \mathbf{n}_\perp$ we derive

$$\begin{aligned}\dot{\mathbf{m}} &= \omega_A \mathbf{n}_0 \times \mathbf{n}_\perp + \omega_A \lambda_{ex}^2 \nabla^2 \mathbf{n}_\perp \times \mathbf{n}_0 + i\alpha\omega \mathbf{n}_0 \times \mathbf{n}_\perp + \omega_s H(R-r)\, \mathbf{n}_\perp \\ &= \begin{bmatrix} -\omega_A n_z - i\alpha\omega n_z + \omega_s H(R-r)\, n_y + \omega_A \lambda_{ex}^2 \nabla^2 n_z \\ \\ \omega_A n_y + i\alpha\omega n_y + \omega_s H(R-r)\, n_z - \omega_A \lambda_{ex}^2 \nabla^2 n_y \end{bmatrix}. \end{aligned} \tag{A.12}$$

By equating Eqs. A.11 and A.12 we obtain the following coupled equations for components of $\mathbf{n}_\perp$ as

$$\left(\frac{-\omega^2}{2\omega_E + \omega_A}\right) n_z = -\omega_A n_z - i\alpha\omega n_z + \omega_s H(R-r)\, n_y + \omega_A \lambda_{ex}^2 \nabla^2 n_z, \tag{A.13}$$

$$\left(\frac{\omega^2}{2\omega_E + \omega_A}\right) n_y = \omega_A n_y + i\alpha\omega n_y + \omega_s H(R-r)\, n_z - \omega_A \lambda_{ex}^2 \nabla^2 n_y. \tag{A.14}$$

We introduce complex spin wave amplitude as $u = n_y + i n_z$ and its complex conjugate as $u^* = n_y - i n_z$ which results in

$$\begin{cases} n_y = \dfrac{u + u^*}{2} \\ n_z = \dfrac{u - u^*}{2i} \end{cases}. \tag{A.15}$$

Plugging Eq. A.15 into Eqs. A.13 and A.14 we obtain the wave equation for u and u^* as

$$\left(\frac{\omega^2}{2\omega_E+\omega_A}\right)u = \omega_A u + i\alpha\omega u - i\omega_s H(R-r)\,u - \omega_A\lambda_{ex}^2\nabla^2 u, \tag{A.16}$$

$$\left(\frac{\omega^2}{2\omega_E+\omega_A}\right)u^* = \omega_A u^* - i\alpha\omega u^* + i\omega_s H(R-r)\,u^* - \omega_A\lambda_{ex}^2\nabla^2 u^*. \tag{A.17}$$

Equation A.17 is the complex conjugate of Eq. A.16. Therefore, solving only one of these wave equations is sufficient to describe dynamics of the system. By adding the dispersive dissipation term [176, 177], $i\alpha\omega_A\lambda_{ex}^2\nabla^2 u$ to Eq. A.16 we obtain

$$(1+i\alpha)\,\omega_A\lambda_{ex}^2\nabla^2 u + \left(\frac{\omega^2}{2\omega_E+\omega_A}-\omega_A\right)u - i\alpha\omega u + i\omega_s H(R-r)\,u = 0. \tag{A.18}$$

Dividing Eq. A.18 by $1+i\alpha$ and using the Taylor expansion of $(1+i\alpha)^{-1} = 1-i\alpha$ we obtain

$$\omega_A\lambda_{ex}^2\nabla^2 u + (1-i\alpha)\left(\frac{\omega^2}{2\omega_E+\omega_A}-\omega_A\right)u - (1-i\alpha)\,i\alpha\omega u + (1-i\alpha)\,i\omega_s H(r-R)\,u = 0. \tag{A.19}$$

Retaining the linear terms in α, changing r to dimensionless variable $\tilde{r} = r/R$ and multiplying by $\left(\frac{R^2}{\omega_A\lambda_{ex}^2}\right)$ we rewrite Eq. A.19 as

$$\begin{aligned}\frac{1}{\tilde{r}}\frac{\partial}{\partial\tilde{r}}\left(\tilde{r}\frac{\partial u}{\partial\tilde{r}}\right) + \left(\frac{R^2}{\omega_A\lambda_{ex}^2}\right)\Bigg\{\left(\frac{\omega^2}{2\omega_E+\omega_A}-\omega_A\right) &+ i\omega_s H(\tilde{r}-1) + \alpha\omega_s H(\tilde{r}-1) \\ &- i\alpha\left[\omega + \frac{\omega^2}{2\omega_E+\omega_A} - \omega_A\right]\Bigg\}u = 0.\end{aligned} \tag{A.20}$$

Here, we consider the Laplace operator in polar coordinate as $\nabla^2 u = \frac{1}{r}\frac{\partial}{\partial r}\left(r\frac{\partial u}{\partial r}\right)$. Symmetry of the problem indicates that $u(\mathbf{r}) = u(r)$ is a radial function and independent of the polar angle. We summarize Eq. A.20 for convenience as following

$$\frac{1}{\tilde{r}}\frac{\partial}{\partial\tilde{r}}\left(\tilde{r}\frac{\partial u}{\partial\tilde{r}}\right) + Au + iBH(\tilde{r}-1)\,u + \alpha BH(\tilde{r}-1)\,u - i\alpha Cu = 0, \tag{A.21}$$

with coefficients A, B and C defined as

$$A = \left(\frac{R^2}{\omega_A \lambda_{ex}^2}\right)\left(\frac{\omega^2}{2\omega_E + \omega_A} - \omega_A\right), \tag{A.22}$$

$$B = \left(\frac{R^2}{\omega_A \lambda_{ex}^2}\right)\omega_s, \tag{A.23}$$

$$C = \left(\frac{R^2}{\omega_A \lambda_{ex}^2}\right)\left[\omega + \frac{\omega^2}{2\omega_E + \omega_A} - \omega_A\right]. \tag{A.24}$$

Equation A.21 can be written as

$$\frac{1}{\tilde{r}}\frac{\partial}{\partial \tilde{r}}\left(\tilde{r}\frac{\partial u}{\partial \tilde{r}}\right) + k_i^2 u = 0, \tag{A.25}$$

which is the Bessel equation with the complex wavenumber, k_i ($i = 1, 2$). Here, $k_1 = \sqrt{A + iB + \alpha(B - iC)}$ ($k_2 = \sqrt{A - i\alpha C}$) for $0 < \tilde{r} < 1$ ($\tilde{r} > 1$), i.e. inside (outside) the nano-constriction. Following Slonczewski [58, 178], we take a piecewise Bessel solution of the form

$$u(\tilde{r}) = \begin{cases} J_0(k_1\tilde{r}); & 0 \le r \le 1, \\ cH_0^{(1)}(k_2\tilde{r}); & r > 1, \text{ with } c = \dfrac{J_0(k_1\tilde{r})}{H_0^{(1)}(k_2\tilde{r})}, \end{cases} \tag{A.26}$$

where $J_0(x)$ and $H_0^{(1)}(x)$ are the Bessel and Hankel functions of the first kind, respectively. Requiring continuity of the derivative of u at the NC boundary $\tilde{r} = 1$, leads to the following complex transcendental equation whose real and imaginary parts determine two real eigenvalues ω and ω_s at the threshold [58, 178]

$$k_1 H_0^{(2)}(k_2) J_1(k_1) = k_2 H_1^{(2)}(k_2) J_0(k_1). \tag{A.27}$$

We solve this equation by expanding the wavenumbers in the small parameter α as

$$\begin{aligned} k_1 &= k_{10} + \alpha k_{11} \equiv \sqrt{A_0 + iB_0} + \alpha \frac{A_1 + B_0 + i(B_1 - C)}{2\sqrt{A_0 + iB_0}}, \\ k_2 &= k_{20} + \alpha k_{21} \equiv \sqrt{A_0} + \alpha \frac{A_1 - iC}{2\sqrt{A_0}}, \end{aligned} \tag{A.28}$$

where

$$A = A_0 + \alpha A_1 = A_0 + \alpha \left(A_{11} + A_{12} C\right), \tag{A.29}$$

$$B = B_0 + \alpha B_1 = B_0 + \alpha \left(B_{11} + B_{12} C\right). \tag{A.30}$$

We plug Eq. A.28 into Eq. A.27 and match the terms of the order of $O(1)$ and $O(\alpha)$ separately which results in

$$O(1): \qquad k_{10} H_0^{(2)}\left(k_{20}\right) J_1\left(k_{10}\right) = k_{20} H_1^{(2)}\left(k_{20}\right) J_0\left(k_{10}\right), \tag{A.31}$$

$$\begin{aligned} O(\alpha): \qquad k_{11} \quad & \left[k_{10} J_0\left(k_{10}\right) H_0^{(2)}\left(k_{20}\right) + k_{20} J_1\left(k_{10}\right) H_1^{(2)}\left(k_{20}\right)\right] \\ -k_{21} \quad & \left[k_{20} J_0\left(k_{10}\right) H_0^{(2)}\left(k_{20}\right) + k_{10} J_1\left(k_{10}\right) H_1^{(2)}\left(k_{20}\right)\right] = 0. \end{aligned} \tag{A.32}$$

Numerical solution to Eq. A.31 gives $A_0 = 1.428$ and $B_0 = 1.863$. Using these values and we solve Eq. A.32 which is a linear equation for A_1 and B_1 and obtain $A_{11} = -3.087$, $A_{12} = 0.815$, $B_{11} = -1.581$ and $B_{12} = 1.004$. From Eqs. A.22 and A.29 we get

$$\begin{aligned} A = A_0 + \alpha \left(A_{11} + A_{12} C\right) = A_0 + \alpha \left\{A_{11} + A_{12}\left(\frac{R^2}{\omega_A \lambda_{ex}^2}\right)\left[\omega + \frac{\omega^2}{2\omega_E + \omega_A} - \omega_A\right]\right\} \\ = \left(\frac{R^2}{\omega_A \lambda_{ex}^2}\right)\left(\frac{\omega^2}{2\omega_E + \omega_A} - \omega_A\right). \end{aligned} \tag{A.33}$$

Multiplying by $\left(\frac{\omega_A \lambda_{ex}^2}{R^2}\right)$ and rearranging the terms we obtain

$$\begin{aligned} \left(\frac{\omega^2}{2\omega_E + \omega_A} - \omega_A\right) \quad - \quad & \left(\frac{\omega_A \lambda_{ex}^2}{R^2}\right)\left(A_0 + \alpha A_{11}\right) \\ - \quad & \left(\frac{\omega_A \lambda_{ex}^2}{R^2}\right) \alpha A_{12}\left(\frac{R^2}{\omega_A \lambda_{ex}^2}\right)\left[\omega + \frac{\omega^2}{2\omega_E + \omega_A} - \omega_A\right] = 0. \end{aligned} \tag{A.34}$$

Rearranging the terms, we obtain the following equation the eigenvalue ω

$$\omega^2 - \left[\frac{\alpha A_{12}(2\omega_E+\omega_A)}{1-\alpha A_{12}}\right]\omega - (2\omega_E+\omega_A)\left[\omega_A + \left(\frac{A_0+\alpha A_{11}}{1-\alpha A_{21}}\right)\left(\frac{\omega_A\lambda_{ex}^2}{R^2}\right)\right] = 0. \tag{A.35}$$

Solution to this equation gives the threshold frequency as

$$\begin{aligned}\omega_{\text{th}} &= \frac{\alpha A_{12}(2\omega_E+\omega_A)}{2(1-\alpha A_{12})} \\ &+\sqrt{\left[\frac{\alpha A_{12}(2\omega_E+\omega_A)}{2(1-\alpha A_{12})}\right]^2 + (2\omega_E+\omega_A)\left[\omega_A + \left(\frac{A_0+\alpha A_{11}}{1-\alpha A_{12}}\right)\left(\frac{\omega_A\lambda_{ex}^2}{R^2}\right)\right]}.\end{aligned} \tag{A.36}$$

Equating Eqs. A.23 and A.30 we obtain

$$\omega_s = \left(\frac{\omega_A\lambda_{ex}^2}{R^2}\right)[B_0 + \alpha(B_{11}+B_{12}C)], \tag{A.37}$$

and considering $\omega_s = \dfrac{2\hbar\gamma\theta_{SH}J_c}{eM_s d_{AF}}\eta$ we obtain the threshold current density as a function of the coefficient C as

$$J_c = \left(\frac{eM_s d_{AF}}{2\gamma\hbar\theta_{SH}\eta}\right)\left(\frac{\omega_A\lambda_{ex}^2}{R^2}\right)[B_0 + \alpha(B_{11}+B_{12}C)]. \tag{A.38}$$

We rewrite Eqs. A.24 and A.34 as

$$\left(\frac{\omega^2}{2\omega_E+\omega_A} - \omega_A\right) = \left(\frac{\omega_A\lambda_{ex}^2}{R^2}\right)C - \omega, \tag{A.39}$$

$$\left(\frac{\omega^2}{2\omega_E+\omega_A} - \omega_A\right) - \left(\frac{\omega_A\lambda_{ex}^2}{R^2}\right)(A_0+\alpha A_{11}) - \left(\frac{\omega_A\lambda_{ex}^2}{R^2}\right)\alpha A_{12}C = 0, \tag{A.40}$$

respectively. By replacing the first term in Eq. A.40 with Eq. A.39 we obtain C as

$$C = \left(\frac{R^2}{\omega_A\lambda_{\text{ln}}^2}\right)\left(\frac{\omega}{1-\alpha A_{21}}\right) + \frac{A_0+\alpha A_{11}}{1-\alpha A_{12}}. \tag{A.41}$$

Plugging Eq. A.41 into Eq. A.38 we obtain the threshold current density as

$$J_{c,\mathrm{th}} = \left(\frac{eM_s d_{AF}}{2\gamma\hbar\theta_{SH}\eta}\right)\left\{\left(\frac{\omega_A\lambda_{ex}^2}{R^2}\right)\left[B_0 + \alpha B_{11} + \alpha B_{21}\left(\frac{A_0+\alpha A_{11}}{1-\alpha A_{12}}\right)\right] + \left(\frac{\alpha B_{12}}{1-\alpha A_{12}}\right)\omega_{\mathrm{th}}\right\}. \quad \text{(A.42)}$$

A.2 Continuum model from micromagnetic formalism in OOMMF

In this section we employ a similar method to Ref. [186] to derive a continuum model free energy from discrete micromagnetic energy terms used in OOMMF [98]. In this micromagnetic code the standard 6-neighbor exchange energy density (**Oxs_Exchange6Ngbr**) for cell k is given by

$$E_{k,ex} = \sum_{l\in N_l} A_{kl}\frac{\mathbf{S}_k.(\mathbf{S}_k-\mathbf{S}_l)}{\Delta_{kl}^2}, \quad \text{(A.43)}$$

where N_l is the set consisting of the 6 cells nearest to cell k in 3D, A_{kl} is the exchange coefficient between cells k and l and Δ_{kl} is the discretization step size between cell k and cell l. **S** is the unit vector of magnetization in the cell. The exchange energy density of a pair of neighboring cells is given by

$$E_{ex}^{\mathrm{pair}}(k,l) = \frac{A_{kl}}{\Delta_{kl}^2}\mathbf{S}_k.(\mathbf{S}_k-\mathbf{S}_l) + \frac{A_{lk}}{\Delta_{lk}^2}\mathbf{S}_l.(\mathbf{S}_l-\mathbf{S}_k). \quad \text{(A.44)}$$

Considering $A_{kl} = A_{lk} = A_{ex}$ and $\Delta_{kl} = \Delta_{lk} = a$, the total exchange energy of this pair of neighboring cells is given by

$$\begin{aligned} VE_{ex}^{\mathrm{pair}}(k,l) &= \frac{A_{ex}V}{a^2}\times[\mathbf{S}_k.(\mathbf{S}_k-\mathbf{S}_l)+\mathbf{S}_l.(\mathbf{S}_l-\mathbf{S}_k)] \\ &= \frac{A_{ex}V}{a^2}\times\left[S_k^2-\mathbf{S}_k.\mathbf{S}_l+S_l^2-\mathbf{S}_l.\mathbf{S}_k\right] \\ &= \frac{2A_{ex}V}{a^2}\times(1-\mathbf{S}_k.\mathbf{S}_l), \end{aligned} \quad \text{(A.45)}$$

where $V = a^3$ is the volume of each cell. The first term in Eq. A.45 is a constant energy shift and does not contribute to the dynamics of the system. The total exchange free energy term of the whole system important for spin dynamics is given by

$$F_{ex} = \left(-\frac{2A_{ex}V}{a^2}\right) \sum_{\langle k,l \rangle} \mathbf{S}_k.\mathbf{S}_l = J \sum_{\langle k,l \rangle} \mathbf{S}_k.\mathbf{S}_l. \tag{A.46}$$

This exchange energy describes a G-type cubic antiferromagnet with $J = \left(-\frac{2A_{ex}V}{a^2}\right)$. We define average magnetization and the Néel order vector as

$$\mathbf{m} = \frac{\mathbf{S}_k + \mathbf{S}_1}{2}, \tag{A.47}$$

$$\mathbf{n} = \frac{\mathbf{S}_k - \mathbf{S}_l}{2}, \tag{A.48}$$

respectively. Using $\mathbf{S}_k = \mathbf{m} + \mathbf{n}$ and $\mathbf{S}_l = \mathbf{m} - \mathbf{n}$, Eq. A.46 can be written as the system free energy under the continuum approximation. We consider a quasi-two-dimensional system since we have only one cell along the thickness of the simulated antiferromagnetic layer. To keep the distance between sublattice pairs equal along both coordinate axes, we define **m** and **n** in a rotated coordinate system $x'Oy'$ which we call "continuum coordinate system". $x'Oy'$ is rotated by $\theta = 45$ degree counterclockwise with respect to xOy coordinate system which we call the "discrete coordinate system", as shown in Fig. A.1.

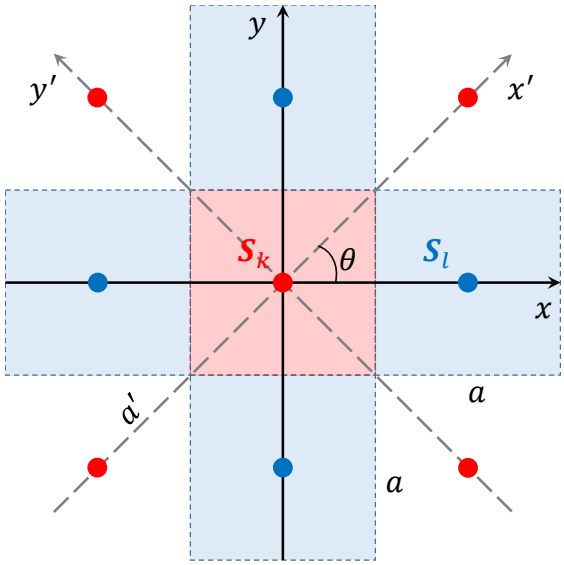

Figure A.1: Schematics of the studied system. The neighboring cells in the discrete micromagnetic model are illustrated by transparent red and blue squares with the side length a (cell size) and diameter a'. The neighboring spins corresponding to these cells are shown by solid circles. Since the system represents a G-type antiferromagnet, the red and blue color of the neighboring cells indicates that they belong to two opposing sublattices of the antiferromagnet. The xOy and $x'Oy'$ are the discrete and continuum coordinate systems.

Plugging $\mathbf{S}_k = \mathbf{m} + \mathbf{n}$ into Eq. A.46 we obtain

$$F_{ex} = J\sum \quad \{(\mathbf{m}_{i,j} - \mathbf{n}_{i,j}).[(\mathbf{m}_{i,j} + \mathbf{n}_{i,j}) + (\mathbf{m}_{i+1,j} + \mathbf{n}_{i+1,j}) + (\mathbf{m}_{i,j+1} + \mathbf{n}_{i,j+1}) + (\mathbf{m}_{i+1,j+1} + \mathbf{n}_{i+1,j+1})]\}, \tag{A.49}$$

$$F_{ex} = J\sum \left[F_{i,j}^{(0)} + F_{i,j}^{(1)} + F_{i,j}^{(2)} + F_{i,j}^{(3)} + F_{i,j}^{(4)}\right], \tag{A.50}$$

where subscripts i and j indicate the sublattice pairs in the continuum coordinate system and

$$F_{i,j}^{(0)} = \mathbf{m}_{ij}^2 - \mathbf{n}_{i,j}^2, \tag{A.51}$$
$$F_{i,j}^{(1)} = \mathbf{m}_{i,j}.(\mathbf{m}_{i+1,j} + \mathbf{m}_{i,j+1} + \mathbf{m}_{i+1,j+1}), \tag{A.52}$$
$$F_{i,j}^{(2)} = -\mathbf{n}_{i,j}.(\mathbf{n}_{i+1,j} + \mathbf{n}_{i,j+1} + \mathbf{n}_{i+1,j+1}), \tag{A.53}$$
$$F_{i,j}^{(3)} = \mathbf{m}_{i,j}.(\mathbf{n}_{i+1,j} + \mathbf{n}_{i,j+1} + \mathbf{n}_{i+1,j+1}), \tag{A.54}$$
$$F_{i,j}^{(4)} = -\mathbf{n}_{i,j}.(\mathbf{m}_{i+1,j} + \mathbf{m}_{i,j+1} + \mathbf{m}_{i+1,j+1}). \tag{A.55}$$

To obtain the continuum model we replace differences with derivatives as given below

$$\mathbf{m}_{i+1,j} - \mathbf{m}_{i,j} = a'\partial_{x'}\mathbf{m}, \tag{A.56}$$
$$\mathbf{m}_{i,j+1} - \mathbf{m}_{i,j} = a'\partial_{y'}\mathbf{m}, \tag{A.57}$$
$$\mathbf{m}_{i+1,j+1} - \mathbf{m}_{i,j} = a'\partial_{x'}\mathbf{m} + a'\partial_{y'}\mathbf{m}, \tag{A.58}$$
$$\mathbf{n}_{i+1,j} - \mathbf{n}_{i,j} = a'\partial_{x'}\mathbf{n}, \tag{A.59}$$
$$\mathbf{n}_{i,j+1} - \mathbf{n}_{i,j} = a'\partial_{y'}\mathbf{n}, \tag{A.60}$$
$$\mathbf{n}_{i+1,j+1} - \mathbf{n}_{i,j} = a'\partial_{x'}\mathbf{n} + a'\partial_{y'}\mathbf{n}, \tag{A.61}$$

where $a' = a\sqrt{2}$ is the distance of sublattice pairs in $x'Oy'$ coordinate along both x' and y'. Using the vectorial identity $\mathbf{v}_1.\mathbf{v}_2 = \frac{1}{2}\left[\mathbf{v}_1^2 + \mathbf{v}_2^2 - (\mathbf{v}_1 - \mathbf{v}_2)^2\right]$ we have e.g.

$$\mathbf{n}_{i,j}.\mathbf{n}_{i+1,j} = \frac{1}{2}\left[2\mathbf{n}^2 - \left(a'\partial_{x'}\mathbf{n}\right)^2\right],$$
$$\mathbf{n}_{i,j}.\mathbf{n}_{i,j+1} = \frac{1}{2}\left[2\mathbf{n}^2 - \left(a'\partial_{y'}\mathbf{n}\right)^2\right],$$
$$\mathbf{n}_{i,j}.\mathbf{n}_{i+1,j+1} = \frac{1}{2}\left[2\mathbf{n}^2 - \left(a'\partial_{x'}\mathbf{n} + a'\partial_{y'}\mathbf{n}\right)\right].$$

With the same argument for all the terms in Eqs. A.52-A.55 we obtain

$$F_{i,j}^{(0)} = \mathbf{m}^2 - \mathbf{n}^2, \tag{A.62}$$
$$F_{i,j}^{(1)} = +\left[3\mathbf{m}^2 - \frac{1}{2}\left[\left(a'\partial_{x'}\mathbf{m}\right)^2 + \left(a'\partial_{y'}\mathbf{m}\right)^2 + \left(a'\partial_{x'}\mathbf{m} + a'\partial_{y'}\mathbf{m}\right)^2\right]\right], \tag{A.63}$$
$$F_{i,j}^{(2)} = -\left[3\mathbf{n}^2 - \frac{1}{2}\left[\left(a'\partial_{x'}\mathbf{n}\right)^2 + \left(a'\partial_{y'}\mathbf{n}\right)^2 + \left(a'\partial_{x'}\mathbf{m} + a'\partial_{y'}\mathbf{m}\right)^2\right]\right], \tag{A.64}$$
$$F_{i,j}^{(3)} = +\left[3\mathbf{m}.\mathbf{n} + 2\mathbf{m}.\left(a'\partial_{x'}\mathbf{n} + a'\partial_{y'}\mathbf{n}\right)\right], \tag{A.65}$$
$$F_{i,j}^{(4)} = -\left[3\mathbf{m}.\mathbf{n} + 2\mathbf{n}.\left(a'\partial_{x'}\mathbf{m} + a'\partial_{y'}\mathbf{m}\right)\right]. \tag{A.66}$$

Substituting these equations into Eq. A.50 and replacing discrete sum with $\sum \rightarrow \frac{1}{V'}\int dV'$ (with $V' = aa'^2$) we obtain the exchange free energy of the system in $x'Oy'$ coordinate system as

$$\begin{aligned} F_{ex} = \left(\frac{-2AV}{a^2}\right)\frac{1}{V'}\int dV'\Big\{ \quad & 4\left[\left(\mathbf{m}^2 - \mathbf{n}^2\right)\right] - \left[\left(a'\partial_{x'}\mathbf{m}\right)^2 + \left(a'\partial_{y'}\mathbf{m}\right)^2 + a'\partial_{x'}\mathbf{m}.a'\partial_{y'}\mathbf{m}\right] \\ & + \left[\left(a'\partial_{x'}\mathbf{n}\right)^2 + \left(a'\partial_{y'}\mathbf{n}\right)^2 + a'\partial_{x'}\mathbf{n}.a'\partial_{y'}\mathbf{n}\right] + \left[3\mathbf{m}.\mathbf{n} + 2\mathbf{m}.\left(a'\partial_{x'}\mathbf{n} + a'\partial_{y'}\mathbf{n}\right)\right] \\ & - \left[3\mathbf{m}.\mathbf{n} + 2\mathbf{n}.\left(a'\partial_{x'}\mathbf{m} + a'\partial_{y'}\mathbf{m}\right)\right]\Big\}. \end{aligned} \tag{A.67}$$

Since $\mathbf{m}.\mathbf{n} = 0$ we have

$$\begin{cases} \partial_{x'}\left(\mathbf{m}.\mathbf{n}\right) = \mathbf{m}.\partial_{x'}\mathbf{n} + \mathbf{n}.\partial_{x'}\mathbf{m} = 0, \\ \partial_{y'}\left(\mathbf{m}.\mathbf{n}\right) = \mathbf{m}.\partial_{y'}\mathbf{n} + \mathbf{n}.\partial_{y'}\mathbf{m} = 0, \end{cases} \tag{A.68}$$

which results in $-\mathbf{n}.\left(a'\partial_{x'}\mathbf{m} + a'\partial_{y'}\mathbf{m}\right) = \mathbf{m}.\left(a'\partial_{x'}\mathbf{n} + a'\partial_{y'}\mathbf{n}\right)$ and we obtain

$$F_{ex} = \int dV' \Big\{ \quad A_h \left(\mathbf{m}^2 - \mathbf{n}^2\right) - A'_{nh} \Big[\left((\partial_{x'}\mathbf{m})^2 + \left(\partial_{y'}\mathbf{m}\right)^2 + \partial_{x'}\mathbf{m}.\partial_{y'}\mathbf{m} \right) - \left((\partial_{x'}\mathbf{n})^2 + \left(\partial_{y'}\mathbf{n}\right)^2 + \partial_{x'}\mathbf{n}.\partial_{y'}\mathbf{n} \right) \Big] + L\mathbf{m}.\left(\partial_{x'}\mathbf{n} + \partial_{y'}\mathbf{n}\right) \Big\}. \tag{A.69}$$

with

$$A_h = 4\left(\frac{-2A_{ex}}{a^2}\right)\left(\frac{V}{V'}\right) = 4\left(\frac{-2A_{ex}}{a^2}\right)\left(\frac{a^3}{2a^3}\right) = \frac{-4A_{ex}}{a^2}, \tag{A.70}$$

$$A'_{nh} = a'^2\left(\frac{-2A_{ex}}{a^2}\right)\left(\frac{V}{V'}\right) = \left(2a^2\right)\left(\frac{-2A_{ex}}{a^2}\right)\left(\frac{a^3}{2a^3}\right) = -2A_{ex}, \tag{A.71}$$

$$L = 4a'\left(\frac{-2A_{ex}}{a^2}\right)\left(\frac{V}{V'}\right) = 4a\sqrt{2}\left(\frac{-2A_{ex}}{a^2}\right)\left(\frac{a^3}{2a^3}\right) = -\frac{4\sqrt{2}A_{ex}}{a} = \frac{-8A_{ex}}{a\sqrt{2}}, \tag{A.72}$$

where A_h, A'_{nh} and L are homogeneous, nonhomogeneous and parity breaking exchange constants. Since the micromagnetic simulations are describing the system in xOy, one needs to transform Eq. A.69 to this coordinate system. Under the rotation transformation shown in Fig. A.1 the homogeneous exchange term remains invariant. The rotation transformation is given by

$$\begin{cases} x = x'\cos\theta - y'\sin\theta, \\ y = x'\sin\theta + y'\cos\theta. \end{cases} \tag{A.73}$$

Under this transformation the derivative operators transform as

$$\begin{cases} \partial_{x'} = \dfrac{\partial x}{\partial x'}\partial_x + \dfrac{\partial y}{\partial x'}\partial_y = \cos\theta\partial_x + \sin\theta\partial_y, \\ \partial_{y'} = \dfrac{\partial x}{\partial y'}\partial_x + \dfrac{\partial y}{\partial y'}\partial_y = -\sin\theta\partial_x + \cos\theta\partial_y. \end{cases} \tag{A.74}$$

Therefore, we have

$$\begin{cases} (\partial_{x'}\mathbf{m})^2 + \left(\partial_{y'}\mathbf{m}\right)^2 = (\partial_x\mathbf{m})^2 + \left(\partial_y\mathbf{m}\right)^2 = (\nabla\mathbf{m})^2, \\ \partial_{x'}\mathbf{m}.\partial_{y'}\mathbf{m} = \partial_x\mathbf{m}.\partial_y\mathbf{m}\left(\cos^2\theta - \sin^2\theta\right) - \sin\theta\cos\theta\left[(\partial_x\mathbf{m})^2 + \left(\partial_y\mathbf{m}\right)^2\right] = -\dfrac{1}{2}(\nabla\mathbf{m})^2. \end{cases} \tag{A.75}$$

Similar equations stand for **n** as well. Applying these change of variables to Eq. A.69 we obtain the total exchange free energy without the parity breaking term in xOy coordinate as

$$F_{ex} = \int dV \left\{A_h\left(\mathbf{m}^2 - \mathbf{n}^2\right) - A_{nh}\left[(\nabla\mathbf{m})^2 - (\nabla\mathbf{n})^2\right]\right\}, \tag{A.76}$$

where $A_{nh} = A'_{nh}/2 = -A_{ex}$.

We consider the total uniaxial anisotropy energy (**Oxs_UniaxialAnisotropy** in OOMMF) for the sublattice pair discussed above as

$$VE_{an}(k,l) = -KV\left[(\mathbf{S}_k.\hat{\mathbf{u}})^2 + (\mathbf{S}_l.\hat{\mathbf{u}})^2\right], \tag{A.77}$$

where K is the anisotropy constant and $\hat{\mathbf{u}}$ is the unit vector along the anisotropy axis. We obtain the total anisotropy free energy of the antiferromagnet in $x'Oy'$ coordinate system as

$$\begin{aligned} F_{an} &= -KV\sum\left[(\mathbf{S_k}.\hat{\mathbf{u}})^2 + (\mathbf{S}_l.\hat{\mathbf{u}})^2\right] = -KV\sum\left\{\left[(\mathbf{m}+\mathbf{n}).\hat{\mathbf{u}}\right]^2 + \left[(\mathbf{m}-\mathbf{n}).\hat{\mathbf{u}}\right]^2\right\} && \text{(A.78)} \\ &= \frac{-2KV}{V'}\int dV'\left[(\mathbf{m}.\hat{\mathbf{u}})^2 + (\mathbf{n}.\hat{\mathbf{u}})^2\right] = -K_u\int dV'\left[(\mathbf{m}.\hat{\mathbf{u}})^2 + (\mathbf{n}.\hat{\mathbf{u}})^2\right], && \text{(A.79)} \end{aligned}$$

with $K_u = \dfrac{2KV}{V'} = 2K\dfrac{a^3}{2a^3} = K$. Since the rotation transformation from $x'Oy'$ to xOy does not affect F_{an}, we obtain the free energy density of the antiferromagnet as

$$f = A_h\left(\mathbf{m}^2 - \mathbf{n}^2\right) - A_{nh}\left[(\nabla\mathbf{m})^2 - (\nabla\mathbf{n})^2\right] - K_u\left[(\mathbf{m}.\hat{\mathbf{u}})^2 + (\mathbf{n}.\hat{\mathbf{u}})^2\right]. \tag{A.80}$$

One can rewrite the free energy density of the form

$$f = \left(\frac{M_s}{\gamma}\right)\left(\frac{\gamma}{M_s}f\right) = \frac{M_s}{\gamma}\Big\{ \quad \frac{1}{2}\left(\gamma\frac{2A_h}{M_s}\right)\left(\mathbf{m}^2-\mathbf{n}^2\right) - \frac{1}{2}\left(\gamma\frac{2A_{nh}}{M_s}\right)\left[(\nabla\mathbf{m})^2-(\nabla\mathbf{n})^2\right] - \frac{1}{2}\left(\gamma\frac{2K}{M_s}\right)\left[(\mathbf{m}.\hat{\mathbf{u}})^2+(\mathbf{n}.\hat{\mathbf{u}})^2\right]\Big\}. \tag{A.81}$$

By introducing the exchange and anisotropy fields in frequency units as following

$$\omega_E = \gamma H_E = \gamma\left(\frac{2A_h}{M_s}\right) = \gamma\left(\frac{-8A_{ex}}{a^2M_s}\right), \tag{A.82}$$

$$\omega_A = \gamma H_A = \gamma\left(\frac{2K_u}{M_S}\right), \tag{A.83}$$

$$\omega_A\lambda_{ex}^2 = \gamma\left(\frac{2A_{nh}}{M_s}\right) = \gamma\left(\frac{2\left(\frac{a^2}{4}A_h\right)}{M_s}\right) = \frac{a^2}{4}\left(\gamma\frac{2A_h}{M_s}\right) = \frac{a^2}{4}\omega_E, \tag{A.84}$$

$$\lambda_{ex}^2 = \frac{a^2}{4}\frac{\omega_E}{\omega_A}, \tag{A.85}$$

we obtain the free energy density as

$$f = \frac{M_s}{\gamma}\left\{\frac{1}{2}\omega_E\left(\mathbf{m}^2-\mathbf{n}^2\right) - \frac{1}{2}\omega_A\left[(\mathbf{m}.\hat{\mathbf{u}})^2+(\mathbf{n}.\hat{\mathbf{u}})^2\right] - \frac{1}{2}\omega_A\lambda_{ex}^2\left[(\nabla\mathbf{m})^2-(\nabla\mathbf{n})^2\right]\right\}. \tag{A.86}$$

The free energy density of the form A.80 and A.86 obtained from the micromagetic energy terms of OOMMF with a negative exchange parameter represents the free energy density of a two sublattice antiferromagnet. Relation between the homogeneous and nonhomogeneous exchange constants of the antiferromagnet and the exchange coefficient introduced in OOMMF (A_{ex}) is given by $A_h = \dfrac{-4A_{ex}}{a^2}$ and $A_{nh} = -A_{ex}$.

Bibliography

[1] Momma, K. & Izumi, F. VESTA 3 for three-dimensional visualization of crystal, volumetric and morphology data. *J. Appl. Crystallogr.* **44**, 1272–1276 (2011). DOI: 10.1107/S0021889811038970.

[2] Sulymenko, O. R., Prokopenko, O. V., Tiberkevich, V. S., Slavin, A. N., Ivanov, B. A. & Khymyn, R. S. Terahertz-Frequency Spin Hall Auto-oscillator Based on a Canted Antiferromagnet. *Phys. Rev. Appl.* **8**, 064007 (2017). DOI: 10.1103/PhysRevApplied.8.064007.

[3] Ashton, K. *et al.* That 'Internet of Things' Thing. *RFID Journal* **22**, 97–114 (2009).

[4] "Global IoT market will grow to 24.1 billion devices in 2030, generating $1.5 trillion annual revenue". https://transformainsights.com/news/iot-market-24-billion-usd15-trillion-revenue-2030 (2020). Accessed: 2020-11-24.

[5] Ummethala, S., Harter, T., Koehnle, K. *et al.* THz-to-optical conversion in wireless communications using an ultra-broadband plasmonic modulator. *Nat. Photonics* **13**, 519–524 (2019). DOI: 10.1038/s41566-019-0475-6.

[6] Bronckers, S., Roc'h, A. & Smolders, B. Wireless Receiver Architectures Towards 5G: Where Are We? *IEEE Circuits Syst. Mag.* **17**, 6–16 (2017). DOI: 10.1109/MCAS.2017.2713306.

[7] Sirtori, C. Bridge for the terahertz gap. *Nature* **417**, 132–133 (2002). DOI: 10.1038/417132b.

[8] Osborne, I. S. Filling the THz Gap. *Science (80-.).* **320**, 1262b–1262b (2008). DOI: 10.1126/science.320.5881.1262b.

[9] Kruglyak, V. V., Demokritov, S. O. & Grundler, D. Magnonics. *J. Phys. D: Appl. Phys.* **43**, 264001 (2010). DOI: 10.1088/0022-3727/43/26/264001.

[10] Tkachenko, V. S., Kuchko, A. N., Dvornik, M. & Kruglyak, V. V. Propagation and scattering of spin waves in curved magnonic waveguides. *Appl. Phys. Lett.* **101**, 152402 (2012). DOI: 10.1063/1.4757994.

[11] Vogt, K., Schultheiss, H., Jain, S., Pearson, J. E., Hoffmann, A., Bader, S. D. & Hillebrands, B. Spin waves turning a corner. *Appl. Phys. Lett.* **101**, 042410 (2012). DOI: 10.1063/1.4738887.

[12] Barman, A., Gubbiotti, G., Ladak, S. *et al.* The 2021 Magnonics Roadmap. *J. Phys. Condens. Matter* **33**, 413001 (2021). DOI: 10.1088/1361-648X/ABEC1A.

[13] .

[14] Hamdi, M., Posva, F. & Grundler, D. Spin wave dispersion of ultra-low damping hematite (α-Fe2O3) at GHz frequencies (2022). DOI: 10.48550/arxiv.2212.11887.

[15] Hamdi, M. & Grundler, D. Terahertz Slonczewski propagating spin waves and large output voltage in antiferromagnetic spin-Hall nano-oscillators (2022). DOI: 10.48550/arxiv.2206.07844.

[16] Sparks, M., Loudon, R. & Kittel, C. Ferromagnetic Relaxation. I. Theory of the Relaxation of the Uniform Precession and the Degenerate Spectrum in Insulators at Low Temperatures. *Phys. Rev.* **122**, 791 (1961). DOI: 10.1103/PhysRev.122.791.

[17] Nanni, E. A., Huang, W. R., Hong, K.-H., Ravi, K., Fallahi, A., Moriena, G., Dwayne Miller, R. J. & Kärtner, F. X. Terahertz-driven linear electron acceleration. *Nat. Commun.* **6**, 8486 (2015). DOI: 10.1038/ncomms9486.

[18] Kartikeyan, M. V., Borie, E. & Thumm, M. K. A. *Gyrotrons: High-Power Microwave and Millimeter Wave Technology.* Advanced Texts in Physics Springer, New York, New York (2004). DOI: 10.1007/978-3-662-07637-8.

[19] Hübers, H. W. Towards THz integrated photonics. *Nat. Photonics* **4**, 503–504 (2010). DOI: 10.1038/nphoton.2010.169.

[20] Consolino, L., Jung, S., Campa, A. *et al.* Spectral purity and tunability of terahertz quantum cascade laser sources based on intracavity difference-frequency generation. *Sci. Adv.* **3** (2017). DOI: 10.1126/sciadv.1603317.

[21] Ozyuzer, L., Koshelev, A. E., Kurter, C. *et al.* Emission of Coherent THz Radiation from Superconductors. *Science (80-.).* **318**, 1291–1293 (2007). DOI: 10.1126/science.1149802.

[22] Gorshunov, B., Volkov, A., Spektor, I., Prokhorov, A., Mukhin, A., Dressel, M., Uchida, S. & Loidl, A. Terahertz BWO-Spectrosopy. *Int. J. Infrared Millimeter Waves* **26**, 1217–1240 (2005). DOI: 10.1007/s10762-005-7600-y.

[23] Tonouchi, M. Cutting-edge terahertz technology. *Nat. Photonics* **1**, 97–105 (2007). DOI: 10.1038/nphoton.2007.3.

[24] Cheng, R., Xiao, J., Niu, Q. & Brataas, A. Spin Pumping and Spin-Transfer Torques in Antiferromagnets. *Phys. Rev. Lett.* **113**, 057601 (2014). DOI: 10.1103/PhysRevLett.113.057601.

[25] Johansen, Ø. & Brataas, A. Spin pumping and inverse spin Hall voltages from dynamical antiferromagnets. *Phys. Rev. B* **95**, 220408 (2017). DOI: 10.1103/PhysRevB.95.220408.

[26] Li, J., Wilson, C. B., Cheng, R. *et al.* Spin current from sub-terahertz-generated antiferromagnetic magnons. *Nature* **578**, 70–74 (2020). DOI: 10.1038/s41586-020-1950-4.

[27] Vaidya, P., Morley, S. A., Van Tol, J., Liu, Y., Cheng, R., Brataas, A., Lederman, D. & Del Barco, E. Subterahertz spin pumping from an insulating antiferromagnet. *Science (80-.).* **368**, 160–165 (2020). DOI: 10.1126/science.aaz4247.

[28] Cheng, R., Xiao, D. & Brataas, A. Terahertz Antiferromagnetic Spin Hall Nano-Oscillator. *Phys. Rev. Lett.* **116**, 207603 (2016). DOI: 10.1103/PhysRevLett.116.207603.

[29] Khymyn, R., Lisenkov, I., Tiberkevich, V., Ivanov, B. A. & Slavin, A. Antiferromagnetic THz-frequency Josephson-like Oscillator Driven by Spin Current. *Sci. Rep.* **7**, 43705 (2017). DOI: 10.1038/srep43705.

[30] Chęciński, J., Frankowski, M. & Stobiecki, T. Antiferromagnetic nano-oscillator in external magnetic fields. *Phys. Rev. B* **96**, 174438 (2017). DOI: 10.1103/PhysRevB.96.174438.

[31] Khymyn, R., Tiberkevich, V. & Slavin, A. Antiferromagnetic spin current rectifier. *AIP Adv.* **7**, 055931 (2017). DOI: 10.1063/1.4977974.

[32] Johansen, Ø., Skarsvåg, H. & Brataas, A. Spin-transfer antiferromagnetic resonance. *Phys. Rev. B* **97**, 054423 (2018). DOI: 10.1103/PhysRevB.97.054423.

[33] Gomonay, O., Jungwirth, T. & Sinova, J. Narrow-band tunable terahertz detector in antiferromagnets via staggered-field and antidamping torques. *Phys. Rev. B* **98**, 104430 (2018). DOI: 10.1103/PhysRevB.98.104430.

[34] Puliafito, V., Khymyn, R., Carpentieri, M., Azzerboni, B., Tiberkevich, V., Slavin, A. & Finocchio, G. Micromagnetic modeling of terahertz oscillations in an antiferromagnetic material driven by the spin Hall effect. *Phys. Rev. B* **99**, 024405 (2019). DOI: 10.1103/PhysRevB.99.024405.

[35] Lee, D.-K., Park, B.-G. & Lee, K.-J. Antiferromagnetic Oscillators Driven by Spin Currents with Arbitrary Spin Polarization Directions. *Phys. Rev. Appl.* **11**, 054048 (2019). DOI: 10.1103/PhysRevApplied.11.054048.

[36] Lisenkov, I., Khymyn, R., Åkerman, J., Sun, N. X. & Ivanov, B. A. Subterahertz ferrimagnetic spin-transfer torque oscillator. *Phys. Rev. B* **100**, 100409 (2019). DOI: 10.1103/PhysRevB.100.100409.

[37] Troncoso, R. E., Rode, K., Stamenov, P., Coey, J. M. D. & Brataas, A. Antiferromagnetic single-layer spin-orbit torque oscillators. *Phys. Rev. B* **99**, 054433 (2019). DOI: 10.1103/PhysRevB.99.054433.

[38] Safin, A., Puliafito, V., Carpentieri, M., Finocchio, G., Nikitov, S., Stremoukhov, P., Kirilyuk, A., Tyberkevych, V. & Slavin, A. Electrically tunable detector of THz-frequency signals based on an antiferromagnet. *Appl. Phys. Lett.* **117**, 222411 (2020). DOI: 10.1063/5.0031053.

[39] Parthasarathy, A., Cogulu, E., Kent, A. D. & Rakheja, S. Precessional spin-torque dynamics in biaxial antiferromagnets. *Phys. Rev. B* **103**, 024450 (2021). DOI: 10.1103/PhysRevB.103.024450.

[40] Shtanko, O. & Prokopenko, O. Terahertz-Frequency Signal Source Based on an Array of Antiferromagnetic Spin Hall Oscillators. *2020 IEEE 10th Int. Conf. Nanomater. Appl. Prop.* 01NMM04–1–01NMM04–4 (2020). DOI: 10.1109/NAP51477.2020.9309712.

[41] Sulymenko, O., Prokopenko, O., Lisenkov, I., Åkerman, J., Tyberkevych, V., Slavin, A. N. & Khymyn, R. Ultra-fast logic devices using artificial "neurons" based on antiferromagnetic pulse generators. *J. Appl. Phys.* **124**, 152115 (2018). DOI: 10.1063/1.5042348.

[42] Khymyn, R., Lisenkov, I., Voorheis, J., Sulymenko, O., Prokopenko, O., Tiberkevich, V., Akerman, J. & Slavin, A. Ultra-fast artificial neuron: generation of picosecond-duration spikes in a current-driven antiferromagnetic auto-oscillator. *Sci. Rep.* **8**, 15727 (2018). DOI: 10.1038/s41598-018-33697-0.

[43] Daniels, M. W., Cheng, R., Yu, W., Xiao, J. & Xiao, D. Nonabelian magnonics in antiferromagnets. *Phys. Rev. B* **98**, 134450 (2018). DOI: 10.1103/PhysRevB.98.134450.

[44] Sulymenko, O. R. & Prokopenko, O. V. Terahertz-Frequency Spin Hall Oscillators for Logic Operations. *Proc. Int. Conf. Adv. Optoelectron. Lasers, CAOL* **2019-Septe**, 533–536 (2019). DOI: 10.1109/CAOL46282.2019.9019409.

[45] Sulymenko, O. R. & Prokopenko, O. V. Logic Circuits Based on Neuron-Like Antiferromagnetic Spin Hall Oscillators. *2019 IEEE 39th Int. Conf. Electron. Nanotechnology, ELNANO 2019 - Proc.* 132–137 (2019). DOI: 10.1109/ELNANO.2019.8783266.

[46] Grollier, J., Querlioz, D., Camsari, K. Y., Everschor-Sitte, K., Fukami, S. & Stiles, M. D. Neuromorphic spintronics (2020), URL https://doi.org/10.1038/s41928-019-0360-9.

[47] Artman, J. O., Murphy, J. C. & Foner, S. Magnetic Anisotropy in Antiferromagnetic Corundum-Type Sesquioxides. *Phys. Rev.* **138**, A912 (1965). DOI: 10.1103/PhysRev.138.A912.

[48] Morrish, A. H. *Canted Antiferromagnetism: Hematite* World Scientific (1995). DOI: 10.1142/2518.

[49] Gurevich, A. & Melkov, G. *Magnetization Oscillations and Waves.* Taylor & Francis (1996). ISBN: 9780849394607.

[50] Gross, R. & Marx, A. *Festkörperphysik.* De Gruyter Oldenbourg (2014). DOI: 10.1524/9783110358704.

[51] Anderson, P. W. Antiferromagnetism. Theory of Superexchange Interaction. *Phys. Rev.* **79**, 350 (1950). DOI: 10.1103/PhysRev.79.350.

[52] Dzyaloshinsky, I. A thermodynamic theory of "weak" ferromagnetism of antiferromagnetics. *J. Phys. Chem. Solids* **4**, 241–255 (1958). DOI: 10.1016/0022-3697(58)90076-3.

[53] Moriya, T. Anisotropic Superexchange Interaction and Weak Ferromagnetism. *Phys. Rev.* **120**, 91–98 (1960). DOI: 10.1103/PhysRev.120.91.

[54] D'yakonov, M. & Perel', V. Possibility of Orienting Electron Spins with Current. *JETP Lett.* **13**, 657 (1971).

[55] Hirsch, J. E. Spin Hall Effect. *Phys. Rev. Lett.* **83**, 1834–1837 (1999). DOI: 10.1103/PhysRevLett.83.1834.

[56] Zhang, S. Spin Hall Effect in the Presence of Spin Diffusion. *Phys. Rev. Lett.* **85**, 393 (2000). DOI: 10.1103/PhysRevLett.85.393.

[57] Slonczewski, J. Current-driven excitation of magnetic multilayers. *J. Magn. Magn. Mater.* **159**, L1–L7 (1996). DOI: 10.1016/0304-8853(96)00062-5.

[58] Slonczewski, J. C. Excitation of spin waves by an electric current. *J. Magn. Magn. Mater.* **195**, L261–L268 (1999). DOI: 10.1016/S0304-8853(99)00043-8.

[59] Berger, L. Emission of spin waves by a magnetic multilayer traversed by a current. *Phys. Rev. B* **54**, 9353–9358 (1996). DOI: 10.1103/PhysRevB.54.9353.

[60] Berger, L. Effect of interfaces on Gilbert damping and ferromagnetic resonance linewidth in magnetic multilayers. *J. Appl. Phys.* **90**, 4632 (2001). DOI: 10.1063/1.1405824.

[61] Stiles, M. D. & Zangwill, A. Anatomy of spin-transfer torque. *Phys. Rev. B* **66**, 014407 (2002). DOI: 10.1103/PhysRevB.66.014407.

[62] Ralph, D. & Stiles, M. Spin transfer torques. *J. Magn. Magn. Mater.* **320**, 1190–1216 (2008). DOI: 10.1016/j.jmmm.2007.12.019.

[63] Haney, P. M. & Stiles, M. D. Current-induced torques in the presence of spin-orbit coupling. *Phys. Rev. Lett.* **105**, 126602 (2010). DOI: 10.1103/PHYSREVLETT.105.126602/FIGURES/3/MEDIUM.

[64] Haney, P. M., Lee, H. W., Lee, K. J., Manchon, A. & Stiles, M. D. Current induced torques and interfacial spin-orbit coupling: Semiclassical modeling. *Phys. Rev. B* **87**, 174411 (2013). DOI: 10.1103/PHYSREVB.87.174411/FIGURES/6/MEDIUM.

[65] Amin, V. P. & Stiles, M. D. Spin transport at interfaces with spin-orbit coupling: Phenomenology. *Phys. Rev. B* **94**, 104420 (2016). DOI: 10.1103/PHYSREVB.94.104420/FIGURES/4/MEDIUM.

[66] Amin, V. P. & Stiles, M. D. Spin transport at interfaces with spin-orbit coupling: Formalism. *Phys. Rev. B* **94**, 104419 (2016). DOI: 10.1103/PHYSREVB.94.104419/FIGURES/4/MEDIUM.

[67] Silsbee, R. H., Janossy, A. & Monod, P. Coupling between ferromagnetic and conduction-spin-resonance modes at a ferromagnetic—normal-metal interface. *Phys. Rev. B* **19**, 4382 (1979). DOI: 10.1103/PhysRevB.19.4382.

[68] Tserkovnyak, Y., Brataas, A. & Bauer, G. E. Enhanced Gilbert Damping in Thin Ferromagnetic Films. *Phys. Rev. Lett.* **88**, 117601 (2002). DOI: 10.1103/PhysRevLett.88.117601.

[69] Takahashi, S. Physical Principles of Spin Pumping. In *Handb. Spintron.*, 1445–1480 (Springer Netherlands, Dordrecht, 2016). URL http://link.springer.com/10.1007/978-94-007-6892-5_51.

[70] Fujii, T., Takano, M., Kakano, R., Isozumi, Y. & Bando, Y. Spin-flip anomalies in epitaxial α-Fe2O3 films by Mössbauer spectroscopy. *J. Magn. Magn. Mater.* **135**, 231–236 (1994). DOI: 10.1016/0304-8853(94)90351-4.

[71] Leighton, C., Hoffmann, A., Fitzsimmons, M. R., Nogués, J. & Schuller, I. K. Deposition of epitaxial α-Fe2O3 layers for exchange bias studies by reactive dc magnetron sputtering. *Philos. Mag. B* **81**, 1927–1934 (2001). DOI: 10.1080/13642810110061501.

[72] Lee, I. J., Kim, J.-Y., Yu, C., Chang, C.-H., Joo, M.-K., Lee, Y. P., Hur, T.-B. & Kim, H.-K. Morphological and structural characterization of epitaxial α-Fe2O3 (0001) deposited on Al2O3 (0001) by dc sputter deposition. *J. Vac. Sci. Technol. A Vacuum, Surfaces, Film.* **23**, 1450–1455 (2005). DOI: 10.1116/1.2013321.

[73] Park, S., Jang, H., Kim, J.-Y., Park, B.-G., Koo, T.-Y. & Park, J.-H. Strain control of Morin temperature in epitaxial α-Fe2O3 (0001) film. *EPL (Europhysics Lett.* **103**, 27007 (2013). DOI: 10.1209/0295-5075/103/27007.

[74] Shimomura, N., Pati, S. P., Sato, Y., Nozaki, T., Shibata, T., Mibu, K. & Sahashi, M. Morin transition temperature in (0001)-oriented α-Fe 2 O 3 thin film and effect of Ir doping. *J. Appl. Phys.* **117**, 17C736 (2015). DOI: 10.1063/1.4916304.

[75] Pati, S. P., Al-Mahdawi, M., Ye, S., Nozaki, T. & Sahashi, M. Control of spin-reorientation transition in (0001) oriented α-Fe2O3 thin film by external magnetic field and temperature. *Phys. status solidi* **11**, 1700101 (2017). DOI: 10.1002/pssr.201700101.

[76] Cheng, Y., Yu, S., Ahmed, A. S., Zhu, M., Rao, Y., Ghazisaeidi, M., Hwang, J. & Yang, F. Anisotropic magnetoresistance and nontrivial spin Hall magnetoresistance in Pt/α-Fe2O3 bilayers. *Phys. Rev. B* **100**, 220408 (2019). DOI: 10.1103/PhysRevB.100.220408.

[77] Cheng, Y., Yu, S., Zhu, M., Hwang, J. & Yang, F. Electrical Switching of Tristate Antiferromagnetic Néel Order in α-Fe2O3 Epitaxial Films. *Phys. Rev. Lett.* **124**, 027202 (2020). DOI: 10.1103/PhysRevLett.124.027202.

[78] Cogulu, E., Statuto, N. N., Cheng, Y., Yang, F., Chopdekar, R. V., Ohldag, H. & Kent, A. D. Direct imaging of electrical switching of antiferromagnetic Néel order in α-Fe2O3 epitaxial films. *Phys. Rev. B* **103**, L100405 (2021). DOI: 10.1103/PhysRevB.103.L100405.

[79] Wittmann, A., Gomonay, O., Litzius, K. *et al.* Role of substrate clamping on anisotropy and domain structure in the canted antiferromagnet α-Fe2O3. *Phys. Rev. B* **106**, 224419 (2022). DOI: 10.1103/PhysRevB.106.224419.

[80] Ross, A., Lebrun, R., Ulloa, C., Grave, D. A., Kay, A., Baldrati, L., Kronast, F., Valencia, S., Rothschild, A. & Kläui, M. Structural sensitivity of the spin Hall magnetoresistance in antiferromagnetic thin films. *Phys. Rev. B* **102**, 094415 (2020). DOI: 10.1103/PhysRevB.102.094415.

[81] Jani, H., Lin, J.-C., Chen, J. *et al.* Antiferromagnetic half-skyrmions and bimerons at room temperature. *Nature* **590**, 74–79 (2021). DOI: 10.1038/s41586-021-03219-6.

[82] Jani, H., Linghu, J., Hooda, S. *et al.* Reversible hydrogen control of antiferromagnetic anisotropy in α-Fe2O3. *Nat. Commun.* **12**, 1668 (2021). DOI: 10.1038/s41467-021-21807-y.

[83] Kan, D., Moriyama, T., Aso, R., Horai, S. & Shimakawa, Y. Triaxial magnetic anisotropy and Morin transition in α-Fe2O3 epitaxial films characterized by spin Hall magnetoresistance. *Appl. Phys. Lett.* **120**, 112403 (2022). DOI: 10.1063/5.0087643.

[84] Zhang, P., Finley, J., Safi, T. & Liu, L. Quantitative Study on Current-Induced Effect in an Antiferromagnet Insulator/Pt Bilayer Film. *Phys. Rev. Lett.* **123**, 247206 (2019). DOI: 10.1103/PhysRevLett.123.247206.

[85] Wadell, B. *Transmission Line Design Handbook* Artech House (1991).

[86] SurfaceNet GmbH. SurfaceNet GmbH, URL https://surfacenet.de/crystal_products.html?crystal=17.

[87] Egan, W. F. E. *Practical RF Design.* John Wiley and Sons (2003). DOI: 10.1002/0471654094.

[88] Baumgärtl, K. *Magnonic crystals with reconfigurable magnetic defects for spin-based microwave electronics.* Ph.D. thesis (2021). URL https://infoscience.epfl.ch/record/283774.

[89] Brillouin, L. Diffusion de la lumière et des rayons X par un corps transparent homogène. *Annales de Physique* **9**, 88–122 (1922). DOI: 10.1051/anphys/192209170088.

[90] Mandelstam, L. *Zh. Radio-Fiziko-Khimicheskogo Obshchestva* **58**, 381 (1926).

[91] Cottam, M. *Light scattering in magnetic solids.* Wiley, New York (1986). ISBN: 9780471817017.

[92] Sandercock, J. Light Scattering in Solids, Edited by M. Balkanski (1971). Paris: Flammarion Press.

[93] Lindsay, S. M., Anderson, M. W. & Sandercock, J. R. Construction and alignment of a high performance multipass vernier tandem Fabry–Perot interferometer. *Rev. Sci. Instrum.* **52**, 1478–1486 (1981). DOI: 10.1063/1.1136479.

[94] Hillebrands, B. Progress in multipass tandem Fabry–Perot interferometry: I. A fully automated, easy to use, self-aligning spectrometer with increased stability and flexibility. *Rev. Sci. Instrum.* **70**, 1589–1598 (1999). DOI: 10.1063/1.1149637.

[95] Querry, M. R. Optical Constants. Tech. Rep., Missouri University (1984). URL https://apps.dtic.mil/sti/citations/ADA158623.

[96] Sebastian, T., Schultheiss, K., Obry, B., Hillebrands, B. & Schultheiss, H. Micro-focused Brillouin light scattering: imaging spin waves at the nanoscale. *Front. Phys.* **3**, 35 (2015). DOI: 10.3389/fphy.2015.00035.

[97] Che & Ping. *Helimagnons and Skyrmion Dynamics in Cu2OSeO3 and Fe/Gd Multilayers Explored by Brillouin Light Scattering and X-ray Microscopy.* Ph.D. thesis, EPFL (2021). URL https://infoscience.epfl.ch/record/287943.

[98] Donahue, M. J. & Porter, D. G. OOMMF user's guide, version 1.0 (1999). DOI: 10.6028/NIST.IR.6376.

[99] Liu, C., Luo, Y., Hong, D. *et al.* Electric field control of magnon spin currents in an antiferromagnetic insulator. *Sci. Adv.* **7** (2021). DOI: 10.1126/sciadv.abg1669.

[100] Luo, Y., Liu, C., Saglam, H. *et al.* Distinguishing antiferromagnetic spin sublattices via the spin Seebeck effect. *Phys. Rev. B* **103**, L020401 (2021). DOI: 10.1103/PhysRevB.103.L020401.

[101] Lepadatu, S. Boris computational spintronics—High performance multi-mesh magnetic and spin transport modeling software. *J. Appl. Phys.* **128**, 243902 (2020). DOI: 10.1063/5.0024382.

[102] Wang, X. G., Nie, Y. Z., Chotorlishvili, L., Xia, Q. L., Berakdar, J. & Guo, G. H. Electron-magnon spin conversion and magnonic spin pumping in an antiferromagnet/heavy metal heterostructure. *Phys. Rev. B* **103**, 064404 (2021). DOI: 10.1103/PHYSREVB.103.064404/FIGURES/8/MEDIUM.

[103] Jeong, S.-Y., Lee, J.-B., Na, H. & Seong, T.-Y. Epitaxial growth of Cr2O3 thin film on Al2O3 (0001) substrate by radio frequency magnetron sputtering combined with rapid-thermal annealing. *Thin Solid Films* **518**, 4813–4816 (2010). DOI: 10.1016/J.TSF.2010.01.046.

[104] Wickman, B., Bastos Fanta, A., Burrows, A., Hellman, A., Wagner, J. B. & Iandolo, B. Iron Oxide Films Prepared by Rapid Thermal Processing for Solar Energy Conversion. *Sci. Rep.* **7**, 40500 (2017). DOI: 10.1038/srep40500.

[105] Baumgaertl, K. & Grundler, D. Reversal of nanomagnets by propagating magnons in ferrimagnetic yttrium iron garnet enabling nonvolatile magnon memory (2022). DOI: 10.48550/arxiv.2208.10923.

[106] Mieszczak, S., Busel, O., Gruszecki, P., Kuchko, A. N., Kłos, J. W. & Krawczyk, M. Anomalous Refraction of Spin Waves as a Way to Guide Signals in Curved Magnonic Multimode Waveguides. *Phys. Rev. Appl.* **13**, 054038 (2020). DOI: 10.1103/PHYSREVAPPLIED.13.054038/FIGURES/9/MEDIUM.

[107] Doughty, D. C. & White, E. A. D. Imperfections in yttrium iron garnet crystals. *Acta Crystallogr.* **13**, 761–762 (1960). DOI: 10.1107/S0365110X60001837.

[108] Serga, A. A., Chumak, A. V. & Hillebrands, B. YIG magnonics. *J. Phys. D: Appl. Phys.* **43**, 264002 (2010). DOI: 10.1088/0022-3727/43/26/264002.

[109] Maendl, S., Stasinopoulos, I. & Grundler, D. Spin waves with large decay length and few 100 nm wavelengths in thin yttrium iron garnet grown at the wafer scale. *Appl. Phys. Lett.* **111**, 012403 (2017). DOI: 10.1063/1.4991520.

[110] Yu, H., d' Allivy Kelly, O., Cros, V., Bernard, R., Bortolotti, P., Anane, A., Brandl, F., Heimbach, F. & Grundler, D. Approaching soft X-ray wavelengths in nanomagnet-based microwave technology. *Nat. Commun.* **7**, 11255 (2016). DOI: 10.1038/ncomms11255.

[111] Baumgaertl, K., Gräfe, J., Che, P., Mucchietto, A., Förster, J., Träger, N., Bechtel, M., Weigand, M., Schütz, G. & Grundler, D. Nanoimaging of Ultrashort Magnon Emission by Ferromagnetic Grating Couplers at GHz Frequencies. *Nano Lett.* **20**, 7281–7286 (2020). DOI: 10.1021/ACS.NANOLETT.0C02645/ASSET/IMAGES/MEDIUM/NL0C02645_M002.GIF.

[112] Che, P., Baumgaertl, K., Kúkol'ová, A., Dubs, C. & Grundler, D. Efficient wavelength conversion of exchange magnons below 100 nm by magnetic coplanar waveguides. *Nat. Commun.* **11** (2020). DOI: 10.1038/s41467-020-15265-1.

[113] Chumak, A. V., Serga, A. A. & Hillebrands, B. Magnonic crystals for data processing. *J. Phys. D. Appl. Phys.* **50**, 244001 (2017). DOI: 10.1088/1361-6463/aa6a65.

[114] Turov, E. On the Theory of Weak Ferromagnetism. *J. Exp. Theor. Phys.* **9**, 890 (1959).

[115] Keffer, F. *Spin Waves* Springer (1966). DOI: 10.1007/978-3-642-46035-7_1.

[116] Samuelsen, E. J. & Shirane, G. Inelastic neutron scattering investigation of spin waves and magnetic interactions in α-Fe2O3. *Phys. status solidi* **42**, 241–256 (1970). DOI: 10.1002/pssb.19700420125.

[117] Hortensius, J. R., Afanasiev, D., Matthiesen, M., Leenders, R., Citro, R., Kimel, A. V., Mikhaylovskiy, R. V., Ivanov, B. A. & Caviglia, A. D. Coherent spin-wave transport in an antiferromagnet. *Nat. Phys.* **17**, 1001–1006 (2021). DOI: 10.1038/s41567-021-01290-4.

[118] Hamdi, M., Posva, F. & Grundler, D. Ultra-fast spin waves with few mm-long decay length in canted antiferromagnet Hematite (α-Fe2O3). In *67th Annu. Conf. Magn. Magn. Mater. (MMM 2022)*, GOE–12 (2022).

[119] Wang, H., Yuan, R., Zhou, Y. *et al.* Long-distance propagation of high-velocity antiferromagnetic spin waves (2022).

[120] Lebrun, R., Ross, A., Bender, S. A., Qaiumzadeh, A., Baldrati, L., Cramer, J., Brataas, A., Duine, R. A. & Kläui, M. Tunable long-distance spin transport in a crystalline antiferromagnetic iron oxide. *Nature* **561**, 222–225 (2018). DOI: 10.1038/s41586-018-0490-7.

[121] Lebrun, R., Ross, A., Gomonay, O., Baltz, V., Ebels, U., Barra, A. L., Qaiumzadeh, A., Brataas, A., Sinova, J. & Kläui, M. Long-distance spin-transport across the Morin phase transition up to room temperature in ultra-low damping single crystals of the antiferromagnet α-Fe2O3. *Nat. Commun.* **11**, 1–7 (2020). DOI: 10.1038/s41467-020-20155-7.

[122] Wang, H., Xiao, Y., Guo, M., Lee-Wong, E., Yan, G. Q., Cheng, R. & Du, C. R. Spin Pumping of an Easy-Plane Antiferromagnet Enhanced by Dzyaloshinskii–Moriya Interaction. *Phys. Rev. Lett.* **127**, 117202 (2021). DOI: 10.1103/PhysRevLett.127.117202.

[123] Pincus, P. Theory of Magnetic Resonance in α-Fe2O3. *Phys. Rev. Lett.* **5**, 13–15 (1960). DOI: 10.1103/PhysRevLett.5.13.

[124] Searle, C. W. & Wang, S. T. Magnetic-Resonance Properties of Pure and Titanium-Doped Hematite. *J. Appl. Phys.* **39**, 1025–1026 (1968). DOI: 10.1063/1.1656155.

[125] Shone, M. The technology of YIG film growth. *Circuits, Syst. Signal Process.* **4**, 89–103 (1985). DOI: 10.1007/BF01600074.

[126] Watanabe, S., Bhat, V. S., Baumgaertl, K., Hamdi, M. & Grundler, D. Direct observation of multiband transport in magnonic Penrose quasicrystals via broadband and phase-resolved spectroscopy. *Sci. Adv.* **7**, eabg3771 (2021). DOI: 10.1126/sciadv.abg3771.

[127] Moskowitz, B. M., Jackson, M. & Chandler, V. Geophysical Properties of the Near-Surface Earth: Magnetic Properties. In Schubert, G. (ed.) *Treatise Geophys. Resour. Near-Surface Earth*, vol. 11, chap. 11.05, 139–174 (Elsevier, 2015), 2 edn.

[128] Iandolo, B., Wickman, B., Zorić, I. & Hellman, A. The rise of hematite: origin and strategies to reduce the high onset potential for the oxygen evolution reaction. *J. Mater. Chem. A* **3**, 16896–16912 (2015). DOI: 10.1039/C5TA03362D.

[129] Hill, A. H., Jiao, F., Bruce, P. G., Harrison, A., Kockelmann, W. & Ritter, C. Neutron diffraction study of mesoporous and bulk hematite, α-Fe 2O3. *Chem. Mater.* **20**, 4891–4899 (2008). DOI: 10.1021/CM800009S/ASSET/IMAGES/CM-2008-00009S_M002.GIF.

[130] Eaton, J., Morrish, A. & Searle, C. Magnetic domains in hematite and evidence for a new wall structure. *Phys. Lett. A* **26**, 520–521 (1968). DOI: 10.1016/0375-9601(68)90522-7.

[131] Eaton, J. A. & Morrish, A. H. Magnetic Domains in Hematite At and Above the Morin Transition. *J. Appl. Phys.* **40**, 3180–3185 (1969). DOI: 10.1063/1.1658162.

[132] Eaton, J. A. & Morrish, A. H. Magnetic Domain Structure of Hematite. *Can. J. Phys.* **49**, 2768–2777 (1971). DOI: 10.1139/p71-335.

[133] Özdemir, Ö. & Dunlop, D. J. Magnetic memory and coupling between spin-canted and defect magnetism in hematite. *J. Geophys. Res. Solid Earth* **111**, B12S03 (2006). DOI: 10.1029/2006JB004555.

[134] Özdemir, Ö. & Dunlop, D. J. Hysteresis and coercivity of hematite. *J. Geophys. Res. Solid Earth* **119**, 2582–2594 (2014). DOI: 10.1002/2013JB010739.

[135] Bialek, M., Zhang, J., Yu, H. & Ansermet, J. P. Antiferromagnetic resonance in α-Fe2O3 up to its Néel temperature. *Appl. Phys. Lett.* **121**, 032401 (2022). DOI: 10.1063/5.0094868.

[136] Fink, H. J. Resonance Line Shapes of Weak Ferromagnets of the α-Fe2O3 and NiF2 Type. *Phys. Rev.* **133**, A1322 (1964). DOI: 10.1103/PhysRev.133.A1322.

[137] Sebastian, T., Schultheiss, K., Obry, B., Hillebrands, B. & Schultheiss, H. Micro-focused Brillouin light scattering: imaging spin waves at the nanoscale. *Front. Phys.* **3**, 35 (2015). DOI: 10.3389/fphy.2015.00035.

[138] Novotny, L. & Hecht, B. *Principles of Nano-Optics* Cambridge University Press (2012). DOI: 10.1017/CBO9780511794193.

[139] Levy, U., Davidson, N. & Silberberg, Y. Mathematics of vectorial Gaussian beams. *Adv. Opt. Photonics* **11**, 828–891 (2019). DOI: 10.1364/AOP.11.000828.

[140] Kalarickal, S. S., Krivosik, P., Wu, M., Patton, C. E., Schneider, M. L., Kabos, P., Silva, T. J. & Nibarger, J. P. Ferromagnetic resonance linewidth in metallic thin films: Comparison of measurement methods. *J. Appl. Phys.* **99**, 093909 (2006). DOI: 10.1063/1.2197087.

[141] Bilzer, C., Devolder, T., Crozat, P., Chappert, C., Cardoso, S. & Freitas, P. P. Vector network analyzer ferromagnetic resonance of thin films on coplanar waveguides: Comparison of different evaluation methods. *J. Appl. Phys.* **101**, 074505 (2007). DOI: 10.1063/1.2716995.

[142] Yu, H., Kelly, O. d., Cros, V., Bernard, R., Bortolotti, P., Anane, A., Brandl, F., Huber, R., Stasinopoulos, I. & Grundler, D. Magnetic thin-film insulator with ultra-low spin wave damping for coherent nanomagnonics. *Sci. Rep.* **4**, 1–5 (2014). DOI: 10.1038/srep06848.

[143] Levitin, R. Z., Pakhomov, A. S. & Shchurov, V. A. Magnetoelastic Properties of Hematite. *J. Exp. Theor. Phys.* **29**, 669 (1969).

[144] Maksimenkov, P. P. & Ozhogin, V. I. Antiferromagnetic resonance investigation of the magnetoelastic interaction in hematite. *J. Exp. Theor. Phys.* **38**, 324 (1974).

[145] Crameri, F. Scientific colour maps. *Zenodo* DOI: 10.5281/ZENODO.5501399.

[146] Crameri, F., Shephard, G. E. & Heron, P. J. The misuse of colour in science communication. *Nat. Commun.* **11**, 1–10 (2020). DOI: 10.1038/s41467-020-19160-7.

[147] Chou, S. G., Stutzman, P. E., Wang, S., Garboczi, E. J., Egelhoff, W. F. & Plusquellic, D. F. High-resolution terahertz optical absorption study of the antiferromagnetic resonance transition in hematite (α-Fe_2O_3). *J. Phys. Chem. C* **116**, 16161–16166 (2012). DOI: 10.1021/jp3036567.

[148] Aleksandrov, K., Bezmaternykh, L., Kozlov, G., Lebedev, S., Mukhin, A. & Prokhorov, A. Anomalies of high-frequency magnetic permeability of hematite at the Morin phase transition. *J. Exp. Theor. Phys.* **65**, 591 (1987).

[149] Turov, E. A. & Shavrov, V. G. Broken symmetry and magnetoacoustic effects in ferroand antiferromagnetics. *Sov. Phys. Uspekhi* **26**, 593–611 (1983). DOI: 10.1070/PU1983v026n07ABEH004449.

[150] Nagatsuma, T., Ducournau, G. & Renaud, C. C. Advances in terahertz communications accelerated by photonics. *Nat. Photonics* **10**, 371–379 (2016). DOI: 10.1038/nphoton.2016.65.

[151] Ma, Z. T., Geng, Z. X., Fan, Z. Y., Liu, J. & Chen, H. D. Modulators for Terahertz Communication: The Current State of the Art. *Research* **2019**, 1–22 (2019). DOI: 10.34133/2019/6482975.

[152] Jungwirth, T., Marti, X., Wadley, P. & Wunderlich, J. Antiferromagnetic spintronics. *Nat. Nanotechnol.* **11**, 231–241 (2016). DOI: 10.1038/nnano.2016.18.

[153] Baltz, V., Manchon, A., Tsoi, M., Moriyama, T., Ono, T. & Tserkovnyak, Y. Antiferromagnetic spintronics. *Rev. Mod. Phys.* **90**, 015005 (2018). DOI: 10.1103/RevModPhys.90.015005.

[154] Jungwirth, T., Sinova, J., Manchon, A., Marti, X., Wunderlich, J. & Felser, C. The multiple directions of antiferromagnetic spintronics. *Nat. Phys. 2018 143* **14**, 200–203 (2018). DOI: 10.1038/s41567-018-0063-6.

[155] Duine, R. A., Lee, K. J., Parkin, S. S. & Stiles, M. D. Synthetic antiferromagnetic spintronics. *Nat. Phys. 2018 143* **14**, 217–219 (2018). DOI: 10.1038/s41567-018-0050-y.

[156] Gomonay, O., Baltz, V., Brataas, A. & Tserkovnyak, Y. Antiferromagnetic spin textures and dynamics. *Nat. Phys. 2018 143* **14**, 213–216 (2018). DOI: 10.1038/s41567-018-0049-4.

[157] Železný, J., Wadley, P., Olejník, K., Hoffmann, A. & Ohno, H. Spin transport and spin torque in antiferromagnetic devices. *Nat. Phys. 2018 143* **14**, 220–228 (2018). DOI: 10.1038/s41567-018-0062-7.

[158] Němec, P., Fiebig, M., Kampfrath, T. & Kimel, A. V. Antiferromagnetic opto-spintronics. *Nat. Phys. 2018 143* **14**, 229–241 (2018). DOI: 10.1038/s41567-018-0051-x.

[159] Šmejkal, L., Mokrousov, Y., Yan, B. & MacDonald, A. H. Topological antiferromagnetic spintronics. *Nat. Phys. 2018 143* **14**, 242–251 (2018). DOI: 10.1038/s41567-018-0064-5.

[160] Chen, T., Dumas, R. K., Eklund, A., Muduli, P. K., Houshang, A., Awad, A. A., Dürrenfeld, P., Malm, B. G., Rusu, A. & Akerman, J. Spin-Torque and Spin-Hall Nano-Oscillators. *Proc. IEEE* **104**, 1919–1945 (2016). DOI: 10.1109/JPROC.2016.2554518.

[161] Demidov, V., Urazhdin, S., de Loubens, G., Klein, O., Cros, V., Anane, A. & Demokritov, S. Magnetization oscillations and waves driven by pure spin currents. *Phys. Rep.* **673**, 1–31 (2017). DOI: 10.1016/J.PHYSREP.2017.01.001.

[162] Hoefer, M. A., Ablowitz, M. J., Ilan, B., Pufall, M. R. & Silva, T. J. Theory of Magnetodynamics Induced by Spin Torque in Perpendicularly Magnetized Thin Films. *Phys. Rev. Lett.* **95**, 267206 (2005). DOI: 10.1103/PhysRevLett.95.267206.

[163] Mohseni, S. M., Yazdi, H. F., Hamdi, M., Brächer, T. & Mohseni, S. M. Current induced multi-mode propagating spin waves in a spin transfer torque nano-contact with strong perpendicular magnetic anisotropy. *J. Magn. Magn. Mater.* **450**, 40–45 (2018). DOI: 10.1016/J.JMMM.2017.09.032.

[164] Kendziorczyk, T., Demokritov, S. O. & Kuhn, T. Spin-wave-mediated mutual synchronization of spin-torque nano-oscillators: A micromagnetic study of multistable phase locking. *Phys. Rev. B* **90**, 054414 (2014). DOI: 10.1103/PhysRevB.90.054414.

[165] Houshang, A., Iacocca, E., Dürrenfeld, P., Sani, S. R., Åkerman, J. & Dumas, R. K. Spin-wave-beam driven synchronization of nanocontact spin-torque oscillators. *Nat. Nanotechnol.* **11**, 280–286 (2016). DOI: 10.1038/nnano.2015.280.

[166] Kendziorczyk, T. & Kuhn, T. Mutual synchronization of nanoconstriction-based spin Hall nano-oscillators through evanescent and propagating spin waves. *Phys. Rev. B* **93**, 134413 (2016). DOI: 10.1103/PhysRevB.93.134413.

[167] Awad, A. A., Dürrenfeld, P., Houshang, A., Dvornik, M., Iacocca, E., Dumas, R. K. & Åkerman, J. Long-range mutual synchronization of spin Hall nano-oscillators. *Nat. Phys.* **13**, 292–299 (2017). DOI: 10.1038/nphys3927.

[168] Zahedinejad, M., Awad, A. A., Muralidhar, S., Khymyn, R., Fulara, H., Mazraati, H., Dvornik, M. & Åkerman, J. Two-dimensional mutually synchronized spin Hall nano-oscillator arrays for neuromorphic computing. *Nat. Nanotechnol.* **15**, 47–52 (2020). DOI: 10.1038/s41565-019-0593-9.

[169] Zahedinejad, M., Fulara, H., Khymyn, R., Houshang, A., Dvornik, M., Fukami, S., Kanai, S., Ohno, H. & Åkerman, J. Memristive control of mutual spin Hall nano-oscillator synchronization for neuromorphic computing. *Nat. Mater.* **21**, 81–87 (2022). DOI: 10.1038/s41563-021-01153-6.

[170] Hoefer, M. A., Silva, T. J. & Keller, M. W. Theory for a dissipative droplet soliton excited by a spin torque nanocontact. *Phys. Rev. B - Condens. Matter Mater. Phys.* **82**, 054432 (2010). DOI: 10.1103/PHYSREVB.82.054432/FIGURES/12/MEDIUM.

[171] Mohseni, S. M., Sani, S. R., Persson, J. *et al.* Spin torque-generated magnetic droplet solitons. *Science (80-.).* **339**, 1295–1298 (2013). DOI: 10.1126/SCIENCE.1230155/SUPPL_FILE/MOHESNI-SOM.PDF.

[172] Mohseni, M., Hamdi, M., Yazdi, H. F., Banuazizi, S. A. H., Chung, S., Sani, S. R., Åkerman, J. & Mohseni, M. Magnetic droplet soliton nucleation in oblique fields. *Phys. Rev. B* **97**, 184402 (2018). DOI: 10.1103/PhysRevB.97.184402.

[173] Galkina, E. G. & Ivanov, B. A. Dynamic solitons in antiferromagnets (Review Article). *Low Temp. Phys.* **44**, 618 (2018). DOI: 10.1063/1.5041427.

[174] Hals, K. M., Tserkovnyak, Y. & Brataas, A. Phenomenology of current-induced dynamics in antiferromagnets. *Phys. Rev. Lett.* **106**, 107206 (2011). DOI: 10.1103/PHYSREVLETT.106.107206/FIGURES/1/MEDIUM.

[175] See Supplemental Material.

[176] Slavin, A. N. & Kabos, P. Approximate theory of microwave generation in a current-driven magnetic nanocontact magnetized in an arbitrary direction. *IEEE Trans. Magn.* **41**, 1264–1273 (2005). DOI: 10.1109/TMAG.2005.845915.

[177] Slavin, A. & Tiberkevich, V. Excitation of Spin Waves by Spin-Polarized Current in Magnetic Nano-Structures. *IEEE Trans. Magn.* **44**, 1916–1927 (2008). DOI: 10.1109/TMAG.2008.924537.

[178] Chung, S., Eklund, A., Iacocca, E., Mohseni, S. M., Sani, S. R., Bookman, L., Hoefer, M. A., Dumas, R. K. & Åkerman, J. Magnetic droplet nucleation boundary in orthogonal spin-torque nano-oscillators. *Nat. Commun.* **7**, 1–8 (2016). DOI: 10.1038/ncomms11209.

[179] Venkat, G., Fangohr, H. & Prabhakar, A. Absorbing boundary layers for spin wave micromagnetics. *J. Magn. Magn. Mater.* **450**, 34–39 (2018). DOI: 10.1016/J.JMMM.2017.06.057.

[180] Foner, S. High-Field Antiferromagnetic Resonance in Cr2O3. *Phys. Rev.* **130**, 183 (1963). DOI: 10.1103/PhysRev.130.183.

[181] Saidl, V., Němec, P., Wadley, P. *et al.* Optical determination of the Néel vector in a CuMnAs thin-film antiferromagnet. *Nat. Photonics* **11**, 91–96 (2017). DOI: 10.1038/nphoton.2016.255.

[182] Wang, M., Andrews, C., Reimers, S. *et al.* Spin flop and crystalline anisotropic magnetoresistance in CuMnAs. *Phys. Rev. B* **101**, 094429 (2020). DOI: 10.1103/PhysRevB.101.094429.

[183] Moriyama, T., Hayashi, K., Yamada, K., Shima, M., Ohya, Y. & Ono, T. Intrinsic and extrinsic antiferromagnetic damping in NiO. *Phys. Rev. Mater.* **3**, 051402 (2019). DOI: 10.1103/PhysRevMaterials.3.051402.

[184] Zhou, Y., Liao, L., Guo, T. *et al.* Orthogonal interlayer coupling in an all-antiferromagnetic junction. *Nat. Commun.* **13**, 3723 (2022). DOI: 10.1038/s41467-022-31531-w.

[185] Galkina, E. G. & Ivanov, B. A. Dynamic solitons in antiferromagnets (Review Article). *Low Temp. Phys.* **44**, 618–633 (2018). DOI: 10.1063/1.5041427.

[186] Li, X., Shen, L., Bai, Y. *et al.* Bimeron clusters in chiral antiferromagnets. *npj Comput. Mater.* **6**, 1–9 (2020). DOI: 10.1038/s41524-020-00435-y.

Mohammad Hamdi

Curriculum Vitae

LMGN IMX STI
École polytechnique fédérale de Lausanne (EPFL)
1015 Lausanne, Switzerland
(+98) 936-757-9959
(+41) 21-693-4291
mohammad.hamdi@epfl.ch
LMGN, Google Scholar, LinkedIn

Personal Information

Gender, *Male*.

Nationality, *Iranian*.

Birth date, *March 12, 1990*.

Education

Jun 2018 – Feb 2023 **Ph.D. Student**, **École Polytechnique Fédérale de Lausanne (EPFL)**, *School of Engineering (STI), Institute of Materials (IMX), Laboratory of Nanoscale Magnetic Materials and Magnonics (LMGN)*.
Material Science and Engineering
Research: *Spintronics and Magnonics of Antiferromagnets*
Supervisor: Prof. Dirk Grundler

2013–2016 **M.Sc.**, **Shahid Beheshti University**, *Department of Physics*.
Solid State Physics
Thesis: *Effective Hamiltonian approach to the interfacial Dzyaloshinskii-Moriya interaction in ultrathin magnetic films*
Supervisor: Dr. Seyed Majid Mohseni
Adviser: Dr. Ali Sadeghi
Grade: 92.3/100
Rank: 1/16

2010–2013 **B.Sc.**, **University of Urmia**, *Department of basic Science*.
Physics
Grade: 76.95/100
Rank: 4/60

Teaching

Fall 2021 **Teaching Assistant**, *Electricity and Magnetism*, (*undergraduate*).
Institute of Materials, École Polytechnique Fédérale de Lausanne (EPFL)

Fall 2020 **Teaching Assistant**, *Electricity and Magnetism*, (*undergraduate*).
Institute of Materials, École Polytechnique Fédérale de Lausanne (EPFL)

Spring 2020 **Teaching Assistant**, *Introduction to magnetic materials in modern technologies*, (*graduate*).
Institute of Materials, École Polytechnique Fédérale de Lausanne (EPFL)

Fall 2019 **Teaching Assistant**, *Electricity and Magnetism*, (*undergraduate*).
Institute of Materials, École Polytechnique Fédérale de Lausanne (EPFL)

Spring 2016 **Teaching Assistant**, *Advanced Solid State Physics*, (*graduate*).
Department of Physics, Shahid Beheshti University

Spring 2016 **Teaching Assistant**, *Electrodynamics*, (*graduate*).
Department of Physics, Shahid Beheshti University

Fall 2015 **Teaching Assistant**, *Advanced Solid State Physics*, (*graduate*).
Department of Physics, Shahid Beheshti University

Fall 2015 **Teaching Assistant**, *Electrodynamics*, (*graduate*).
Department of Physics, Shahid Beheshti University

Spring 2015 **Teaching Assistant**, *Electrodynamics*, (*graduate*).
Department of Physics, Shahid Beheshti University

Fall 2014 **Teaching Assistant**, *Electrodynamics*, (*graduate*).
Department of Physics, Shahid Beheshti University

Fall 2014 **Teaching Assistant**, *Solid State Physics*, (*undergraduate*).
Department of Physics, Shahid Beheshti University

Scientific Experiences

Jun 2018 – Feb 2023 **Doctoral Assistant**, *Spintronics and Magnonics*.
LMGN - IMX - STI - EPFL
Supervisor: Prof. Dirk Grundler

Feb 2016 – Jun 2018 **Junior Researcher**, *NanoMagnetism and Spintronics*.
NanoPhysics and Spintronics Group, Department of Physics, Shahid Beheshti University
Supervisor: Dr. Seyed Majid Mohseni

Jan 2015 – Jan 2016 **Research Assistant**, *NanoMagnetism and Spintronics*.
NanoPhysics and Spintronics Group, Department of Physics, Shahid Beheshti University
Supervisor: Dr. Seyed Majid Mohseni

– **Journal Referee-Nature**, *Scientific Reports*.

– **Journal Referee-IOPscience**, *Journal of Physics: Condensed Matter*.

– **Journal Referee-IOPscience**, *Journal of Physics D: Applied Physics*.

Experimental/Nanofabrication Experience & Skills

Experimental Experience:
– Spatial-, Angle-, Time- and Phase- Resolved Brillouin Light Scattering Spectroscopy (Micro- and Macro-BLS)
– Cryogenic Brillouin Light Scattering Spectroscopy (Cryo-BLS)
– Cryogenics (Liquid Helium and Nitrogen Cryostat, Closed-Cycle Cryostat)
– Vector Network Analyzer Spin Wave Spectroscopy (VNA, Cryo-VNA)
– Microwave electronics and magnetic resonance spectroscopy
– Magneto-Transport measurements (AMR, GMR, AHE, PHE)
– X-Ray Diffraction (XRD)
– SQUID Magnetometry
– Scanning Electron Microscopy (SEM)

Nano-Fabrication Experience:
– Experience in an ISO6 Clean Room Environment (Center of MicroNanoTechnology-CMi-EPFL)
– Electron Beam Lithography (EBL)
– Ion Beam Etching (IBE)
– Ga and Xe-Plasma Focused Ion Beam Etching (FIB, PFIB)
– Epitaxial Reactive Magnetron Sputtering (Thin Films of Fe_2O_3, Cr_2O_3, NiO)
– Rapid Thermal Annealing/Oxidation (RTP)
– Furnace Thermal Annealing/Oxidation (FTP)

Computational Experience & Skills

Programming Languages:
– MATLAB
– Mathematica
– Python
– LabView
– LaTeX

Scientific Software Packages:
– MuMax3 (Micromagnetic spin Simulations)
– OOMMF (Micromagnetic spin Simulations)
– Boris (Multi-Physics Magnetisation Dynamics and Spin Transport Simulations)
– SpinW (Atomistic Linear Spin Wave Theory)
– UppASD (Atomistic Spin Dynamics)
– Spirit (Atomistic Spin Dynamics)

Publication

17 – **Spin wave dispersion of ultra-low damping hematite (α-Fe2O3) at GHz frequencies**.
M. Hamdi, F. Posva, D. Grundler
arXiv:2212.11887 (2022)

16 – **Terahertz Slonczewski propagating spin waves in antiferromagnetic spin-Hall nano-oscillators**.
M. Hamdi, D. Grundler
arXiv:2206.07844 (2022)

15 – **Magnetochiral properties of spin waves existing in nanotubes with axial and circumferential magnetization**.
M. C. Giordano*, **M. Hamdi***, A. Mucchietto, D. Grundler (*Equal Contribution, Accepted by Phys. Rev. Materials)
arXiv:2204.12995 (2022)

14 – **Long decay length of magnon-polarons in $BiFeO_3$/$La_{0.67}Sr_{0.33}MnO_3$ heterostructures**.
J. Zhang*, M. Chen*, J. Chen*, K. Yamamoto*, H. Wang*, **M. Hamdi***, Y. Sun, K. Wagner, W. He, Y. Zhang, J. Ma, P. Gao, X. Han, D. Yu, P. Maletinsky, J-P. Ansermet, S. Maekawa, D. Grundler, C-W. Nan, H. Yu (*Equal Contribution)
Nat. Commun **12**, 7258 (2021)

13 – **Magnetoelastic coupling enabled tunability of magnon spin current generation in two-dimensional antiferromagnets**.
N. Bazazzadeh*, **M. Hamdi***, S. Park, A. Khavasi, S. M. Mohseni, A. Sadeghi (*Equal Contribution)
Phys. Rev. B **104**, L180402 (2021)

12 – **Direct observation of multiband transport in magnonic Penrose quasicrystals via broadband and phase-resolved spectroscopy**.
S. Watanabe, V. S. Bhat, K. Baumgaertl, **M. Hamdi**, D. Grundler
Sci. Adv **7**, eabg3771 (2021)

11 – **van der Waals epitaxy of $Co_{10-x}Zn_{10-y}Mn_{x+y}$ thin films: chemical composition engineering and magnetic properties**.
A. Kukolova, S. E. Steinvall, R. Paul, J-B. Leran, P. Che, **M. Hamdi**, A. Mucchietto, D. Grundler, and A. Fontcuberta i Morral
J. Phys. Chem. C, **125**, 17, 9391 (2021)

10 – **Symmetry enhanced spin-Nernst effect in honeycomb antiferromagnetic transition metal trichalcogenide monolayers**.
N. Bazazzadeh*, **M. Hamdi***, F. Haddadi, A. Khavasi, A. Sadeghi, and S. M. Mohseni (*Equal Contribution)
Phys. Rev. B **103**, 014425 (2021)

9 – **Morphological magnetostatic coupling in spin valves due to anisotropic self-affine interface roughness**.
M. J. Kamali Ashtiani, M. Mokhtarzadeh, **M. Hamdi**, S. M. Mohseni
J. Appl. Phys **127**, 095301 (2020)

8 – **Electrical and optical properties of MoS_2, $MoO_{x=2,3}$ (MoSO)/RGO heterostructure**.
S. Erfanifam, L. Jamilpanah, P. Sangpour, **M. Hamdi**, F. Haddadi, M. Erfanifam, G. Chanda, T. Herrmannsdorfer, V. Sazgari, A. Sadeghi, S. M. Mohseni
arXiv:1808.03534 (2018)

7 – **Magnetic droplet soliton nucleation in oblique fields**.
S. Morteza Mohseni*, **M. Hamdi***, H. F. Yazdi, S. A. H. Banouazizi, S. R. Sani, S. Chung, J. Akerman, and S. M. Mohseni (*Equal Contribution)
Phys. Rev. B **97** 184402 (2018)

6 – **Current induced multi-mode propagating spin waves in a spin transfer torque nano-contact with strong perpendicular magnetic anisotropy**.
S. Morteza Mohseni, H. F. Yazdi, **M. Hamdi**, T. Bracher, and S. M. Mohseni
J. Magn. Magn. Mater **450**, 40-45 (2018)

5 – **Magnetic graphene/Ni-nano-crystal hybrid for small field magnetoresistive effect synthesized via electrochemical exfoliation/deposition technique**.
Z. Sheykhifard et al.
J. Mater. Sci. Mater. Electron (2017)

4 – **Spin orbit torque driven magnetoimpedance in Pt-layer/magnetic-ribbon heterostructures**.
M. R. Hajiali, S. Morteza Mohseni, L. Jamilpanah, **M. Hamdi**, S. E. Roozmeh, and S. M. Mohseni
Appl. Phys. Lett **111**, 192405 (2017)

3 – **Current-driven second-harmonic domain wall resonance in ferromagnetic metal /nonmagnetic metal bilayers: A field-free method for spin Hall angle measurements**.
M. R. Hajiali*, **M. Hamdi***, S. E. Roozmeh, and S. M. Mohseni (*Equal Contribution)
Phys. Rev. B **96**, 144406 (2017)

2 – **Temperature-induced coupled-decoupled transition in perpendicular pseudo spin valves**.
M. Hamdi, and S. M. Mohseni
J. Phys. D:Appl. Phys **50**, 115003 (2017)

1 – **Magnetostatically driven domain replication in Ni/Co based perpendicular pseudo-spin-valves**.
S. M. Mohseni, **M. Hamdi**, S. Chung, S. R. Sani, and Johan Akerman
J. Phys. D:Appl. Phys **49**, 415004 (2016)

Manuscript in Progres

2 – **Antiferromagnetic droplet soliton in a nano-contact spin-torque oscillator**.
R. S. Khymyn, R. V. Ovcharov, **M. Hamdi**, B. A. Ivanov, and J. Akerman

1 – **Effect of substrate clamping on spin waves in thin film canted antiferromagnet hematite (α-Fe2O3)**.
M. Hamdi, O. Gomonay, D. Grundler

Proceeding

Oct 2022 **Ultra-fast spin waves with few mm-long decay length in canted antiferromagnet Hematite (α-Fe2O3)**.
M. Hamdi (Oral Presentation), F. Posva and D. Grundler
67th Annual Conference on Magnetism and Magnetic Materials (MMM2022), Minneapolis, MN, US, 31 October - 5 November, 2022

Jul 2022 **Towards antiferromagnetic dynamic solitons: terahertz Slonczewskii spin waves in antiferromagnetic spin-Hall nano-oscillators**.
M. Hamdi (Oral Presentation), and D. Grundler
2022 Joint European Magnetic Symposia (JEMS2022), Warsaw, Poland, 24 - 29 July, 2022

Feb 2017 **Current-induced domain-wall motion in magnetic materials with in-plane magnetic anisotropy: The role of the spin Hall effect**.
M. R. Hajiali, **M. Hamdi**, S. E. Roozmeh, and S. M. Mohseni
13^{th} PSI Conference on Condensed Matter, Shahid Rajaee Teacher Training University, Tehran, Iran

Feb 2017 **Magnetic droplet soliton in spin valve with perpendicular magnetic anisotropy**.
H. F. Yazdi, S. Morteza Mohseni, **M. Hamdi**, and S. M. Mohseni
13^{th} PSI Conference on Condensed Matter, Shahid Rajaee Teacher Training University, Tehran, Iran

Feb 2017 **Magnetic coupling in spin valve nano layers with rough interfaces**.
M. J. Kamali, **M. Hamdi**, and S. M. Mohseni
13^{th} PSI Conference on Condensed Matter, Shahid Rajaee Teacher Training University, Tehran, Iran

Background

- **Antiferromagnetic Spintronics And Magnonics**.
- **Spin Wave and Magnonics**.
- **Skyrmionics**.
- **Spin-Orbitronics Effects (Rashba-Edelstein, Spin Hall, Dzyaloshinskii-Moriya)**.
- **Spin-Caloritronics Effects (Spin Seebeck Effect, Spin Nernst Effect)**.
- **Micromagnetic Theory**.
- **Density Functional Theory**.
- **Atomistic Spin Dynamics**.
- **Tight Binding**.
- **Boltzmann Transport**.

Attended Workshop

22–26 Aug, 2022 **NeuroSpin Summer School 2022: Spin Based Device Architectures for Neuromorphic Computing and Storage**.
Organizing Committee, EPFL, Laussane, Switzerland (Link to Website).

22–24 Aug, 2019 **Internal Nanoskyrmionics Workshop: Micromagnetic simulation on skyrmion hosting materials**.
Teaching Assistant, EPFL, Laussane, Switzerland (Link to Website).

8–10 Jul, 2019 **Summer School: Advanced Electronic Structure Methods in Condensed Matter Physics**.
EPFL, Laussane, Switzerland (Link to Website).

20–24 Aug, 2018 **Summer school: New Trends in Chiral magnetism**.
EPFL, Laussane, Switzerland (Link to Website).

23 Nov, 2017 2^{th} **PSI Autumn Meeting**.
Oral Presentation: A field-free method for spin Hall angle measurements
University of Tehran, Tehran, Iran

Jan, 2017 13^{th} **PSI Conference on Condensed Matter** .
Shahid Rajaei Teacher Training University, Tehran, Iran

5 March, 2016 **Workshop on Flatland: 2-D materials beyond Graphene**.
Institute for Research in Fundamental Sciences (IPM), Tehran, Iran

21–22 Jan, 2015 **Advanced School on Recent Progress in Condensed Matter Physics**.
Institute for Research in Fundamental Sciences (IPM), Tehran, Iran

4–6 Nov, 2015 **School on Spintronics and Nanomagnetism**.
Institute for Research in Fundamental Sciences (IPM), Tehran, Iran

Memberships

Jan 2014 – Jun 2018 **Physics Society of Iran (PSI)**.

Jan 2013 – Jun 2018 **Students' Scientific Association**.
Department of Physics, Shahis Beheshti University, Tehran, Iran

Sep 2020 – Sep 2021 **Iranian Students Association at EPFL (IRSA)**.
École Polytechnique Fédérale de Lausanne (EPFL), Lausanne, Switzerland

Languages

Azerbaijani	Native
Persian	Native
English	Full professional proficiency
Turkish	Native

References

Prof. Dirk Grundler, LMGN - IMX - STI - EPFL, dirk.grundler@epfl.ch

Prof. Majid Mohseni, Department of Physics, Shahid Beheshti University, m-mohseni@sbu.ac.ir

Prof. Ali Sadeghi, Department of Physics, Shahid Beheshti University, Ali_Sadeghi@sbu.ac.ir